



UNIVERSITY OF AMSTERDAM



MSc Physics and Astronomy
Track: Astronomy & Astrophysics

Master Thesis

Characterization of Gaia Astrometric Exoplanet Candidates

Spectroscopic Follow-Up Observations of Jupiter Desert Targets

by

David A.G. Bruijne
14608278 (UvA)

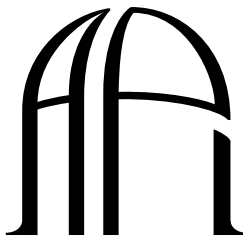
July 2, 2025

60 ECTS

September 2024 - July 2025

Supervisor:
Dr. Gudmundur K. Stefánsson

Second Examiner
Dr. Antonija Oklopčić



ANTON PANNEKOEK
INSTITUTE

Abstract

In this thesis, I present a detailed analysis of the astrometric exoplanet candidates identified by the Gaia mission (ASOIs). To confirm the planetary candidates and to rule a common false positive scenario (i.e. spectroscopic binaries), spectroscopic follow-up observations are crucial.

In this work, I analyze the usage of spectral energy distributions (SEDs) and color-magnitude diagrams to identify potential indicators of multiplicity. The results from the SED fitting software were compared to literature values to evaluate reliability of the software and identify potential indicators of multiplicity. This was done by performing regression analyses and correlation tests on 139 metrics. While most metrics showed no significant correlation, the TESS noise term (used in the SED fitting process) emerged as a weak indicator of multiplicity. This metric, however, was described to be questionable. In addition, we found that ASOIs that were confirmed to be spectroscopic binaries, tended to be over-luminous in the Gaia G band when compared to the Main-Sequence. However, for both results, the small sample size limited statistical power. The spectroscopic follow-up observations were conducted using multiple high-resolution spectrographs. As a part of this work, I analyzed the Gaia astrometric solution to derive the expected radial velocity (RV) curve, which has been used to time the follow-up observations and to aid the observation proposals for those spectrographs. Beyond the ASOIs, two brown dwarf candidates were identified and analyzed in detail. This work provides a framework for prioritizing future follow-up observations in preparation for Gaia's fourth data release.

Contents

1	Introduction	1
1.1	Exoplanet landscape	2
1.1.1	Detection and Demographics	3
1.1.2	Jupiter Desert	9
1.2	Gaia spacecraft	11
1.2.1	Instruments and Scanning Law	11
1.2.2	The Gaia Exoplanet Candidates	13
2	Methods	16
2.1	Color-Magnitude Diagrams as a Probe of Stellar Properties	16
2.1.1	SED fitting	16
2.2	Observations of ASOIs	22
2.2.1	RV Precision	23
2.2.2	Broadening Functions	24
2.2.3	Astrometry and RV Interplay	24
3	Results	30
3.0.1	Observation Proposal	30
3.0.2	SED Fitting using astroARIADNE	34
4	Discussion	45
4.1	SED Fitting	45
4.1.1	Ongoing Observations	52
5	Conclusion	59
5.1	Acknowledgments	60
A	Ariadne	66

List of Figures

List of Figures

1.8	A bar-graph of the different spectral types of all the stars within 10 parsecs. M-dwarfs are significantly more represent in the solar neighborhood than the other spectral types. This trend continues outside the solar neighborhood. The figure is adapted from Stefansson (2025) .	10
1.9	The astrometric precision of Gaia DR3, DR4, and DR5 (color-coded). The solid lines represent the uncertainty in the along-scan and the dashed lines in the across-scan. On the x-axis we see visual magnitude in the G-band and on the y-axis we see the uncertainty on the measurement in milliarcseconds (log-scale). The dots represent the ASOIs and are color coded based on their RUWE parameter. The uncertainties are generated by the PyGaia Python library (Brown 2024)	12
1.10	Hertzsprung-Russell diagram of the Gaia Catalog of Nearby Stars (GCNS), which contains all Gaia measured objects within 200 parsec (The Gaia Collaboration et al. 2021). The exoplanet candidate list is plotted on top of it. The x-axis represents the Gaia Bp-Rp color and y-axis represents the absolute magnitude in the G-band. The exoplanet candidates are split into two groups, 'Possible red dwarfs' and 'Other'. Stellar classification is done by analyzing the spectra of the star. Here it is done based on the Gaia color (Pecaut & Mamajek 2013). There are two clear clumps, the white dwarfs in the lower left corner and the main sequence. The color bar on the side represents the number of stars that can be found in a given area of the HRD. Note that, as expected from Figure 1.8, most stars in our neighborhood are red dwarfs.	15
2.1	The response function of the Gaia DR3 filters (denoted by color). With on the x-axis, the wavelength in micron and on the y-axis the response of the filter. This can be viewed as a percentage of light that passes through the filter. Note that outside the filter ranges, the response is zero. Also, note how within the filter range, the response function is not uniform. Figure is generated using the Speclite (Kirkby et al. 2024) software	18
2.2	Figure adapted from Yi (2024) . This figure shows the radial velocity (x-axis in km/s) plotted against mock broadening functions (y-axis) for a binary star system observed at three different orbital phases. The orange and blue curves represent the individual broadening functions of the two stellar components, while the gray curve represents the combined (measured) broadening function.	25
2.3	Figure adapted from Feng (2024) . A representation of some of the parameters used in the astrometric technique from a heliocentric point-of-view. On top, an enhanced mock system is shown. A similar system is shown in Figure 2.4.	27

2.4	Figure adapted from Lasunncy (2007) , showing multiple system-specific parameters used in the astrometric technique. The system represented is not the same as in Figure 2.3 but can be viewed as a zoomed in representation of the system parameters of that figure. Note that the Gaia solution are given using the Thiele-Ines framework, here we see the Campbell elements.	28
3.1	A comparison plot of the object masses calculated with Gaia's internal pipeline (Flame) and the <code>GORP</code> library. With on the x-axis the FLAME mass and on the y-axis the <code>gorp</code> mass. The objects shown are a random subset of stars within 100 parsec. The red line shows the 1:1 equality.	32
3.2	Same figure as Figure 1.7, now with the addition of the ASOI candidates represented with yellow stars. The histogram in panel b only shows the confirmed exoplanets. A) Scatter plot of confirmed exoplanets. On the x-axis the mass of the host star is shown in Solar masses and on the y-axis the log-scaled mass of the companion is shown in Jupiter masses. In panel b, on the side, a histogram is shown, which represents the companion mass distribution of the plotted exoplanets. C) Scatter-plot with the same x-axis as panel A, but now with the y-axis showing the mass ratio in log scale. The same coloring and marker-scheme is used as in Figure 1.7.	32
3.3	Sky position of all ASOIs using a Hammer-projection. On the horizontal axis the Right-Ascension, and the vertical axis the Declination. The circles indicate the ASOIs, note that not all ASOIs were selected for follow up. The triangles indicate 'Brown Dwarf Candidates' that were followed up and were part of the expanded ASOI list. In Section 4, we discuss these objects in further detail. The coloring-scheme of the objects is done based on the Gaia- <i>G</i> magnitude. In addition, the telescope ranges are highlighted using a underlying color-scheme, with gray indicating the Hobby-Eberly 10-meter telescope, red the ESO 3.6-meter telescope, and blue the WIYN 3.5-meter telescope European Southern Observatory (ESO) (2022, 2002); Stefansson (2019)	33
3.4	Scatterplot of the interpolated effective temperature of the ASOI-targets (shown in black). The red line represent the second degree polynomial used and the blue dotted background represents the data used for the fitting procedure. The code used for the fitting procedure was supplied by E. Koo, a member of the research team.	34

3.5 Two panel figure with on the left (panel a), the expected signal-to-noise ratio of the proposed targets as a function of the effective temperature, the color-bar indicates the orbital period of the companion as found by Gaia. The signal-to-noise ratio is represented in log-scale. In the right plot (panel b) we see a period-mass diagram of the proposed objects, with the color coding indicating the effective temperature. Two lines are annotated within this plot, which are the deuterium burning limit at 13 Jupiter masses and the hydrogen burning limit (sub-stellar/stellar boundary) at around 85 Jupiter masses. On both plots, the errors are shown in gray and the instruments are shown using the marker-scheme found in the legend. It is important to note that objects that are followed up with multiple instruments are shown twice in the plots.	35
3.6 Scatterplot of the fitted distance (Parsec) against the interstellar optical extinction. The data shown are gathered from the test run (the first run), with in gray, the error on the fitted optical extinction.	36
3.7 A six-panel Figure comprising of scatter plots, in which literature values queried from ExoFOP (NASA Exoplanet Science Institute (NExScI) 2022) are plotted against fitted values from the second run. In these six plots, the effective temperature (top-left), the distance (top-right), the radius (middle-left), the Isochrone interpolated stellar mass (middle-right), the metallicity (lower left) and stellar surface gravity (lower-right) are shown in their standard units (K , Parsec, R_{\odot} , M_{\odot} , z_{\odot} , cgs) and with both their literature error and fitted error (indicated by the gray horizontal and vertical bars). With blue indicating unknown systems and orange systems with confirmed multiplicity. The dotted red lines indicates the 1:1 line. The amount of data points shown is solely depended on if the data was available.	38
3.8 Corner plot of posterior parameter distributions (Second run) of Gaia-4b (left) and Gaia-5b (right) with the blue dots representing the literature values found by Stefánsson et al. (2025)	39

- 3.9 Four panel figure representing the best-fitting SED models for Gaia-4 (left-top), Gaia-5 (right-top). Gaia DR3 2845310284780420864 (bottom-left) and Gaia DR3 5085864568417061120 (bottom-right). Every SED is accompanied with a residual plot. The x-axis represents the wavelength (in micron) and is plotted against the energy flux density (in $\text{erg} \cdot \text{cm}^{-2} \cdot \text{s}^{-1}$) in log-scale. The SED model shown (black lines) are the most likely model found. The best-fitting parameters used as input for the models were the parameters found using BMA, not the best-fitting parameters for the model shown. The blue dots represent the fluxes used for the fitting procedure, the error-bars on the x-axis show the width of the filter. The error-bars on the y-axis show the error on the measurement. The purple triangles show the synthetic fluxes. The residual plot underneath each model is calculated using the distance between the blue data points and the purple triangles expressed in standard deviations (using the error on the flux measurement). Gaia-4 and Gaia-5 are prime examples of the usage of the `astroARIADNE` software. Gaia DR3 2845310284780420864 (bottom left) is an example of a query within a densely populated field and where the photometric retrieval was ineffective. Lastly, Gaia DR3 5085864568417061120 is an example of a confirmed spectroscopic binary. 40
- 3.10 Four panel figure with PDF's of the stellar radius (in R_{\odot}). The objects shown are Gaia-4 (top-left), Gaia (top-right), Gaia DR3 557717892980808960 (bottom-left) and Gaia DR3 2571855077162098944 (bottom-right). The color differentiates the PDF's per model (or mix of models). The PDF's are calculated with a kernel density estimation performed on the histograms that are plotted underneath the PDF's. The histograms each have ten bins. The legends for each PDF also contains the model likelihood, which is shortened to 'model prob:'. 41
- 3.11 CMD with the Gaia $Bp - Rp$ color on the x-axis and the Gaia absolute magnitude (M_G) on the y-axis. The blue line is generated by interpolating the stellar parameters Table (Pecaut & Mamajek 2013). The red line is calculated by subtracting $2.5 \log_{10}(2)$ from the blue line, effectively doubling the luminosity of the star. It outlines a rough estimate of the CMD position of two MS stars with equal luminosities ($\epsilon = 1$). The age of the system, as fitted by `astroARIADNE` is shown (in giga-years) by the coloring. Underneath the CMD, the residuals are shown (in absolute magnitude) and follows the same coloring scheme as the CMD. The markers indicate the current status of the object. 42

3.12 Scatterplot of each tested metric, with on the x-axis the Correlation coefficient (r) and on the y-scale the p-value in log-scale. The blue line represents a p value of 0.05 and the red line the Bonferroni correction performed. As we can see, no metric exceeds the Bonferroni correction but multiple metrics exceed the standard significance level of $p = 0.05$. A full description of the metrics tested and their corresponding p- and r- value can be found in Table A.3.	44
4.1 PDF of the surface gravity (cgs) as found by <code>astroARIADNE</code> for Gaia-3A. The models do not seem to agree on a solution.	47
4.2 Histograms of both the effective temperature (upper histogram in Kelvin) and the stellar mass (lower histogram in M_{\odot}). Both values are derived using <code>astroARIADNE</code> . Multiplicity is highlighted by the color-scheme, with Orange indicating single stars and blue confirmed binary systems. Gray highlights the ASOIs that are yet to be determined. The y-axis of both plots indicate the counts.	48
4.3 Two histograms of both the TESS noise metric (upper histogram) and the residual terms of the fitted MS (lower histogram in M_G). The y-axis of both plots indicate the counts. The same color-scheme is used as in Figure 4.2. The white dwarf target was removed in the analysis for the Main-Sequence residuals.	50
4.4 Two panel figure, with on top the RV measurements with a fitted curve of Gaia DR3 3937630969071148032. On the x-axis, we see the Barycentric Julian Date, and on the y-axis the RV in km/s . In the lower figure we see the residual terms. The Color-coding indicates the object, with blue representing the primary and red the secondary.	53
4.5 A plot of the semi-major axis a_0 color-coded as a function of both the primary mass M_1 and the flux-ratio ϵ using a period of 460 days and a mass ratio $q = 0.86$. The Blue line represents the semi major axis found by interpolating the Mamajek Table for the estimated masses to retrieve the flux-ratio. Then, using Equation 1.1 the semi-major axis is found . The red line indicates the Gaia DR3 value. The Black line, denoted with the label 'Theory' shows the flux-ratio as a function of the primary mass (using mass ratio $q = 0.86$).	54
4.6 Corner plot of the derived orbital parameters of Gaia DR3 3937630969071148032, which is a spectroscopic binary. The system has mass ratio $q = 0.86^{+0.046}_{-0.038}$, eccentricity $e = 0.366^{+0.070}_{-0.066}$, period $P = 460.0^{+5.6}_{-5.4}$ and the primary has a RV amplitude of $K = 6.65^{+0.28}_{-0.21} km s^{-1}$	55

- 4.7 The expected RV curve (upper figure) and broadening function (lower figure) for Gaia DR3 3724701024704375424. The expected RV curve is calculated using the Gaia astrometric solution under the assumption of a single star, a full description is given in Section 2 and Section 3. For this figure the x-axis represents the date of measurement and on the y-axis the expected RV measurement in m/s . The red line indicates the expected RV and the thin pink area surrounding it a $1-\sigma$ deviation from this model. The shaded areas indicate the observing windows in which the target can be viewed with the Hobby-Ebberly telescope. The Broadening function corresponds to a unspecified measurement, on the x-axis we see RV in km/s and on the y-axis the broadening function. The blue corresponds to the peak of the broadening function, which is taken as the measured RV. Note that the measured RV does not align with the expected RV. We ignored the movement of the system while calculating the expected RV curve (γ in Equation 2.26), which is unknowable before taking such measurements. Lastly, these figures were generated for internal use only, stylistic and scientific artifacts (such as shifted and flipped data) are still visible and should be ignored. 56
- 4.8 The expected RV curve (upper figure) and broadening function (lower figure) for Gaia DR3 4580216762992082048. This figure follows the same scheme as Figure 4.7. For reference I repeat these notes: The expected RV curve is calculated using the Gaia astrometric solution under the assumption of a single star, a full description is given in Section 2 and Section 3. For this figure the x-axis represents the date of measurement and on the y-axis the expected RV measurement in m/s . The red line indicates the expected RV and the thin pink area surrounding it a $1-\sigma$ deviation from this model. The shaded areas indicate the observing windows in which the target can be viewed with the Hobby-Ebberly telescope. The Broadening function corresponds to a unspecified measurement, on the x-axis we see RV in km/s and on the y-axis the broadening function. The blue corresponds to the peak of the broadening function, which is taken as the measured RV. Note that the measured RV does not align with the expected RV. We ignored the movement of the system while calculating the expected RV curve (γ in Equation 2.26), which is unknowable before taking such measurements. Lastly, these figures were generated for internal use only, stylistic and scientific artifacts (such as shifted and flipped data) are still visible and should be ignored 57

List of Tables

2.1	Overview of <code>astroARIADNE</code> input and output parameters. g_* and σ_{g_*} refer to the MIST estimate of the queried star; D_* and $D_{e,*}$ to the distance and uncertainty from Bailer-Jones et al. (2018); and av to the maximum optical extinction from the Schlegel, Finkbeiner & Davis (SFD) dust map (Schlafly & Finkbeiner 2011). RAVE refers to the fifth data release from the RAVE survey (Kunder et al. 2017). Isochrone interpolation uses the ISOCHrone Python package and MIST tracks (Morton 2015; Dotter 2016). Stellar mass is obtained both directly from $\log g_*$ and via isochrone interpolation. \mathcal{N} and \mathcal{U} represent a normal distribution and a uniform distribution respectively.	22
2.2	Overview of the instruments used for follow-up observations of the <i>Gaia</i> exoplanet candidates (Stefansson 2019; European Southern Observatory (ESO) 2022, 2002). Observatory names have been shortened: Kitt Peak ¹ , McDonald ² , and La Silla ³ refer to Kitt Peak National Observatory (Arizona, U.S.), McDonald Observatory (Texas, U.S.), and La Silla Observatory (Chile), respectively.	23
3.1	A comparison of IR-derived and regular fitted stellar parameters. They tend to agree, with an exception for the surface gravity and the temperature. The IR-derived values also tend to have larger uncertainties.	43
4.1	Table containing the literature values for Gaia-3A (Sozzetti, A. et al. 2023) and our fitted stellar parameters. They seem to be in agreement, with an exception for the stellar surface gravity.	46
4.2	Preliminary stellar and orbital parameters for Object 1 and Object 2 and their companions. The parameters are either adopted from Gaia, calculated using SED fitting or calculated using the Gaia astrometric solutions . The latter is done using a private software package. ¹ : See Table A.2 for a full description of the filters.	58
A.1	Stellar parameters derived from SED fitting. The values shown are from the second run, with exception to the Objects notated with a ' ¹ '. These indicate the results from the third run.	67

A.2	Photometric Filters, Labels, and Wavelength Ranges with Catalogue References. ¹ : Note that these filters are not used for the fitting procedure. these are only available for visualization (IR-excess). ² : These filters were included for the IR-only run.	68
A.3	Pearson correlation coefficient (r) and p -values for all tested metrics. Fitted values contain the prefix 'fit', the 1σ confidence interval is indicated with the suffixes 'upper' and 'lower'. Lastly, the literature values are found at the bottom, without special indication.	69

List of Abbreviations

ASOI Astrometric Object of Interest

BMA Bayesian Model Averaging

CMD Color-Magnitude Diagram

DR3 Data Release 3

DR4 Data Release 4

ESA European Space Agency

FLAME Final Luminosity Age Mass Estimator

FWHM Full-Width at Half Maximum

HARPS High Accuracy Radial velocity Planet Searcher

HPF Habitable Zone Planet Finder

MCMC Markov Chain Monte Carlo

MS Main-Sequence

NEID NN-EXPLORER Exoplanet Investigations with Doppler Spectroscopy

NIRPS Near Infra Red Planet Searcher

NSS Non-Single Star

PDF Probability Density Function

RUWE Renormalized Unit Weight Error

RV Radial Velocity

SED Spectral Energy Distribution

SNR Signal-to-Noise Ratio

YSO Young Stellar Object

Chapter 1

Introduction

Astrometry, which describes the kinematics of celestial bodies across the night sky, has been a fundamental part of astronomy for over 2000 years. The invention of the telescope brought a substantial increase in precision, allowing for the detection of Jupiter's moons ([Perryman 2012](#)). Astrometry has played a significant role in our understanding of the universe and our place in it. The Hipparcos satellite, which was launched in the late 1980s by the European Space Agency (ESA), brought the next step forward. Hipparcos superseded the increase in precision brought by the telescope.

The Gaia spacecraft is the spiritual successor of the Hipparcos mission and, in theme, revolutionized astrometry. It provided not only the best measurements so far but also data for a record 1.5 billion sources ([Vallenari et al. 2023](#); [European Space Agency \[ESA\] & The Gaia Collaboration 2023](#); [The Gaia Collaboration et al. 2016](#)). Gaia is expected to aid in the field of exoplanets by measuring the reflex motion caused by high mass exoplanets. In this thesis, I will use data collected by Gaia to characterize the exoplanet candidates that were published as a part of its third data release in order to gain insights into discerning between a true exoplanet companion and a common false positive scenario — a spectroscopic binary. I will do this using careful analysis of Color-Magnitude diagrams (CMDs) and Spectral Energy Distributions of these targets. In addition, I will use spectroscopic follow-up observations targeted at low-mass stars with the aim of finding high-mass exoplanet companions.

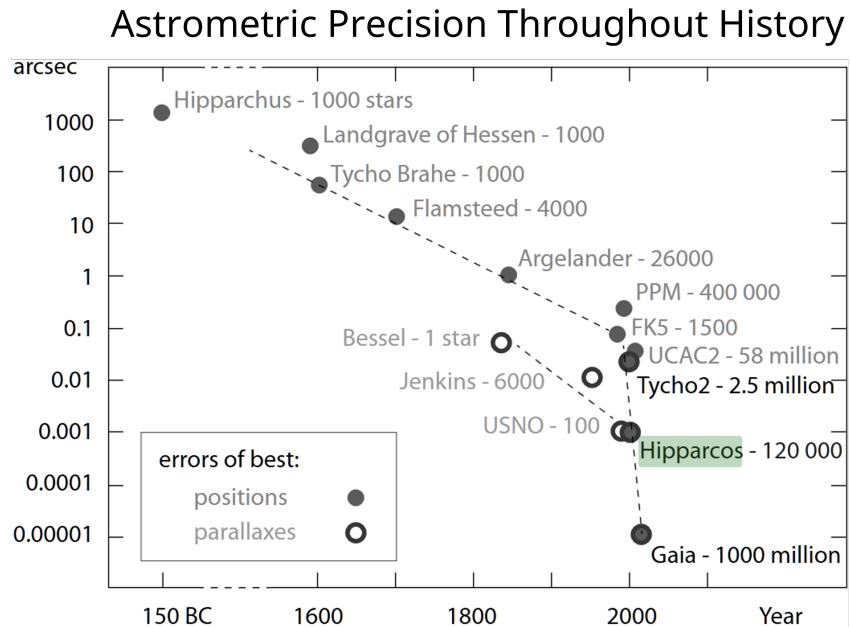


FIG. 1.1 – The advancement of astrometry throughout the ages (Perryman 2012)), with years on the x-axis and precision in arcseconds (log-scale) on the y-axis. Note that there is a gap between Hipparchus and recent history.

1.1 Exoplanet landscape

Exoplanets are objects that orbit a star other than our own. Its orbit must be cleared of any debris and the planet must be in hydrostatic equilibrium. They can be classified into multiple different categories, from gas-giants to smaller rocky planets. To name a few; Earth-like planets are the smallest of the bunch; they are made primarily of rock and can support a thin atmosphere. Neptunes have an intermediate mass. They are typically made out of rock and ice; they can have a thicker atmosphere. Jupiters are the most massive planets. They are composed mostly of a thick hydrogen/helium atmosphere with a dense core. The upper mass limit of planets is commonly set at $13 M_J$, which roughly corresponds to the mass at which deuterium fusion can be sustained inside the object. The true limit is somewhere between 11 and $16 M_J$, depending on the composition (Mollière & Mordasini 2012). Objects that exceed this mass but are not able to sustain hydrogen fusion in their core are called brown dwarfs. These objects range from the previously discussed upper mass limit to around $80 M_J \simeq 0.1 M_\odot$. Objects more massive than this are classified as stars.

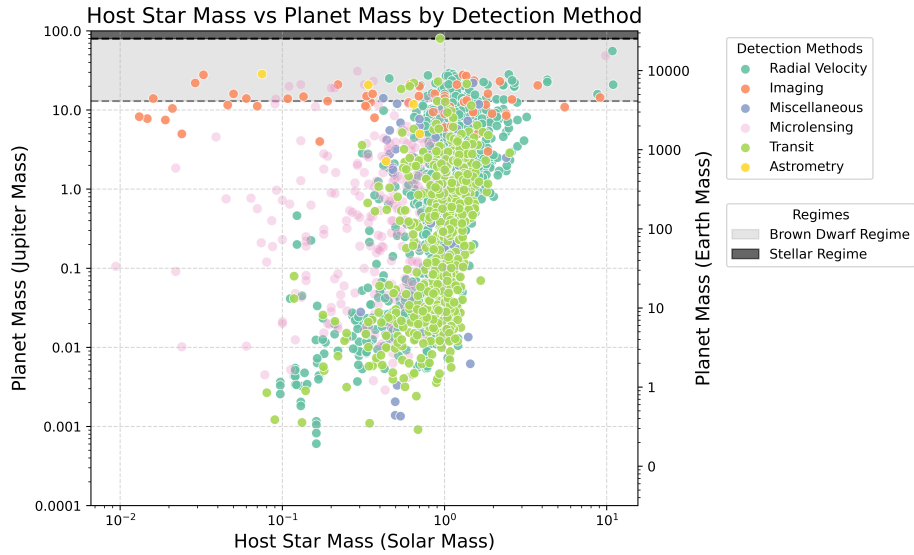


FIG. 1.2 – Scatter plot of all the confirmed exoplanets to date, with stellar mass (M_{\odot}) on the x-axis and planet mass (M_J) on the y-axis, both in log-space. The gray-colored area signifies the brown dwarf regime and the black area signifies the stellar regime. The dots are color-coded according to their initial detection method. ‘Imaging’ and ‘Microlensing’ are methods not discussed in this work. Lastly, ‘Miscellaneous’ refers to other exoplanet detection methods that have resulted in few confirmations to date. The data used is extracted from [Martin \(2019\)](#)

1.1.1 Detection and Demographics

As of 2025, over 5,800 exoplanets have been confirmed, most of them detected using the transit method, followed by the radial velocity (RV) method. The astrometric method has only been used successfully twice [Stefánsson et al. \(2025\)](#). Figure 1.2 shows a scatter plot of all confirmed exoplanets, comparing host star mass to planet mass.

These different detection methods are subject to different biases and they each have their strengths. The transit method is used in cases where the exoplanet blocks the line of sight to the host star, the exoplanet obscures part of the star during its orbit. Photometric data is used over a period of time to look for a temporary and predictable decrease in flux caused by the planet eclipsing the star from our point of view. This method, however, requires the planet to eclipse the star, which leads to observational biases. Close in planets with a larger radius are more likely to partially eclipse their star than far out smaller planets.

The radial velocity (RV) method uses high resolution spectra gathered over time to see if the star is moving in the radial direction. This is done by comparing absorption and emission lines in the star’s spectrum to a stationary reference spectrum. As the star moves toward or away from us, due to the gravitational influence of the planetary

companion, we see a blueshift/redshift of the expected spectral features. This allows us to calculate the velocity of the star in the radial direction. A major drawback is that the RV technique is not sensitive to the inclination of the orbit. This means that we can only calculate the minimum mass of the companion, usually referred to as $M \sin i$. This technique works best for massive planets in close-in orbits around small stars, as this maximizes the amplitude of the signal, but is also used for further out planets.

The astrometric technique uses photometric data to track the position of a star as it moves across the night sky, i.e. the movement in the right ascension (RA) and the declination (DEC). An object without a companion moves in a straight line (the proper motion). This movement from our point of view looks like a sinusoid, due to the movement of the Earth around the Sun (the parallax motion). In top graph of Figure 1.3 we see this motion drawn out over a period of four years. The orange line, represents a best-fit single-star model corresponding to the measurements, which corresponds to the sum of the proper motion of the star with the parallax of the earth (see the lower figure). If the object is gravitationally influenced by an unseen companion, a third motion is added, causing a discrepancy (the reflex motion). The effect on the movement of the star can be seen in the blue line in the upper figure. Note that they both show a periodicity corresponding to the movement of the Earth around the Sun, but the blue line is disturbed by an additional sinusoidal movement.

As outlined by [Marcussen & Albrecht \(2023\)](#), this movement is not necessarily caused by an exoplanet. The object is not optically resolved, and thus we can only measure the movement of the photocenter, not the barycenter (shown by the dotted line in Figure 1.3). This leads to a false positive scenario — a spectroscopic binary (see Figure 1.4). As the two stars orbit the center of mass, the photocenter orbits around the center of mass. The amplitude of the astrometric signal a_0 (the distance between the photocenter and center-of-mass) can be seen as the weighted average between the fluxes of the two stars (F_i) with weights a_i (the distances between the stars and the center-of-mass).

$$a_0 = \left| \frac{F_1 a_1 - F_2 a_2}{F_1 + F_2} \right| \quad (1.1)$$

Assuming the companion is indeed an exoplanet ($F_2 = 0$), $a_0 = a_1$ and the movement of the photocenter becomes identical to the movement of the star, as shown in the right panel of Figure 1.4. If we know the mass of the host star, which we can generally constrain by using spectral energy distribution modeling, we can recover all orbital parameters including the true mass of the companion. The assumption that the companion is indeed an exoplanet must be confirmed by some other method, to rule out the aforementioned false positive scenario. If the companion is not 'dark', this formula can be rewritten using Kepler's third law in terms of the mass ratio,

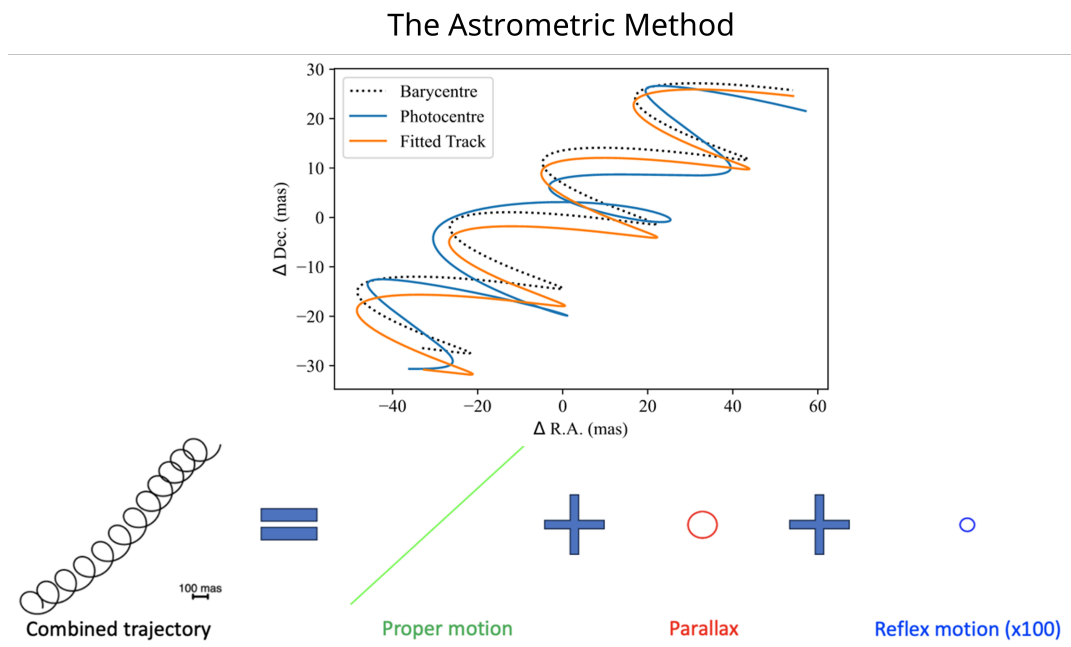


FIG. 1.3 – A two plot figure adapted from both Wallace et al. (2024) (top) and Feng (2024) (bottom). On top we see a simulated periodic astrometric measurement of a brown dwarf with a unspecified mass orbiting a main sequence star (also unspecified) over a period of four years. With blue representing the simulated movement of the object. Note that the x-axis and y-axis denote the change in right ascension and declination (in milliarcseconds). The dotted line represents the true movement of the center of mass. The fitted track represents the single-star fit made by Gaia spacecraft. The bottom figure illustrates the decomposition of the perceived motion in its constituents.

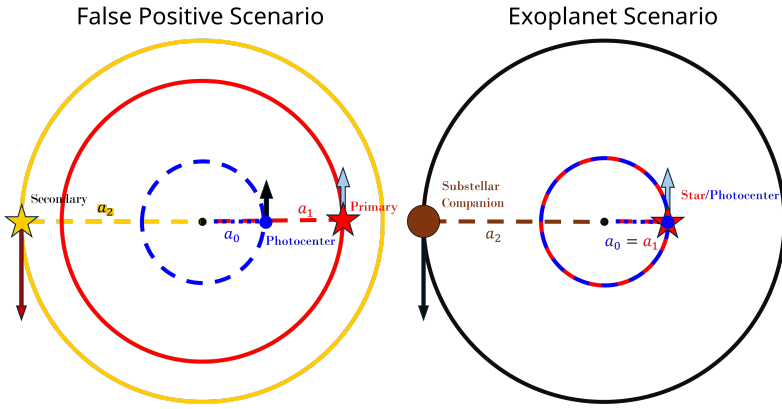


FIG. 1.4 – Illustration of the movement of the photo-center of two different systems. On the left we see a binary system (the false positive) and the right we see a single-star system with a substellar companion. The red and yellow circles are trajectories of the star(s), in brown and blue we see the same for the substellar companion and photocenter respectively. The arrows indicate the movement of the objects with the Doppler shift (with respect to a unshown observer at the top of the page) denoted by the color. Using the Doppler shift we can distinguish between the two cases. In Section 2 we go into further detail on how this is done.

$q \equiv a_1/a_2 = M_2/M_1$ and the flux ratio $\epsilon \equiv F_2/F_1$.

$$a_0^3 = \left| GM_1 \left(\frac{P}{2\pi} \right)^2 (1+q) \left(\frac{1}{1+q} - \frac{1}{1+\epsilon} \right)^3 \right| \quad (1.2)$$

The photocenter will orbit the center of mass at separation a_0 , which will produce the same small astrometric signal as in the dark companion case if $q \simeq \epsilon$ (middle panel of Figure 1.4). This false positive scenario can be ruled out with well-timed RV measurements. Because they are always in opposition, when both stars move in the radial direction we will see a simultaneous red- and blue-shift. This is why the false positive scenario is called a spectroscopic binary; they are easily identified using spectroscopy. It is important to note that in both cases, if $q = \epsilon$, the photocenter and the center of mass completely overlap, which means that there is no reflex motion to cause a discrepancy between the single-star and the star-companion scenarios. Such systems are astrometrically indistinguishable from single-star cases.

This technique works best for massive planets around low-mass stars in far out orbits, as this maximizes the displacement compared to the movement of a single star (shown in Figure 1.5). The recently discovered Gaia-4b and Gaia-5b, found by [Stefánsson et al. \(2025\)](#), are one of the first exoplanets detected with the astrometric technique, and are prime examples of unseen companions to low mass stars. Gaia-4b is a $11.8M_J$ (Jupiter mass) exoplanet orbiting a $0.64M_\odot$ (Solar mass) star. Likewise, Gaia-5b is $20.9M_J$ Brown dwarf orbiting a $0.34M_\odot$ star. These objects are among those that

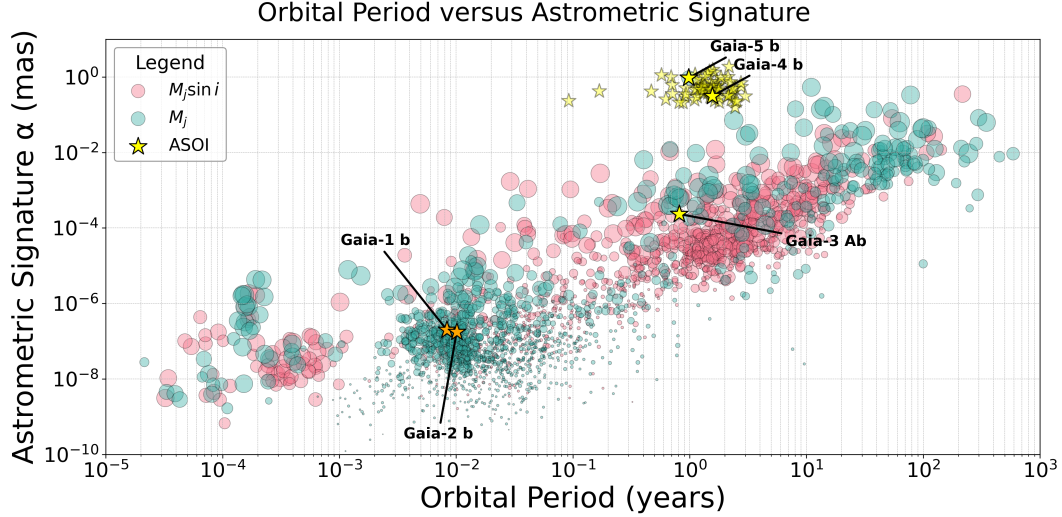


FIG. 1.5 – Scatter plot of known exoplanets and brown dwarf. The x-axis represents the orbital period in years and the y-axis represents the astrometric signature of the system (the amplitude of the orbit) in milliarcseconds. The minimum mass and absolute mass are color-coded and exoplanets found by the Gaia spacecraft are annotated (Orange). The Astrometric Objects of Interests (ASOIs) are highlighted in yellow. The same dataset is used as in Figure 1.2. With the addition of the Gaia exoplanet candidates. Note that Gaia-1b and Gaia-2b are transiting exoplanets ('Gaia TROIs', shown in orange) and Gaia-3 Ab's astrometric solution has been withdrawn.

will be studied in this thesis.

The observational biases mentioned before play an important role in exoplanet (population) research. In Figure 1.6 we see the distribution of exoplanets in a period-mass plot, with the method of discovery color-coded. The first thing to notice is that in the bottom right there are virtually no confirmed exoplanet companions. If they exist, they are very hard to detect using the three detection methods mentioned, as the signal would be very weak. Most planets with close-in orbits are found using the transit method. As the orbital period increases, the separation between the star and its companion increases as well, which will make it less likely that the companion eclipses the star. Another clump of exoplanets can be found near the top right. These are primarily discovered with the RV method. At this separation, only high-mass planets will produce a measurable signal. We do see the RV method being used at close-in orbits as well. Lastly, a notable gap is found at intermediate masses with ultrashort orbits — the Neptune Desert. Exoplanets in this gap lose their mass as the star blows away their atmosphere, leaving a smaller planet behind.

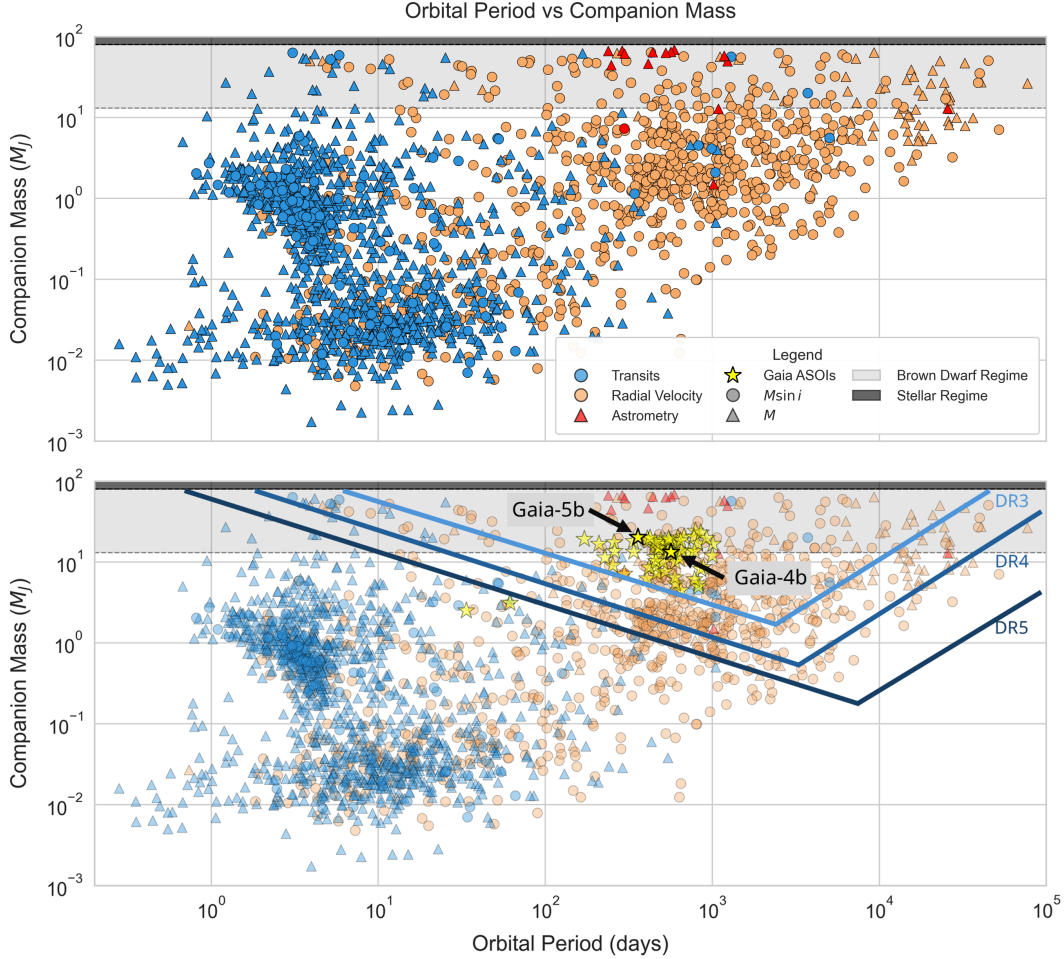


FIG. 1.6 – Two scatter plots of the confirmed sub-stellar companions, with on the x-axis the orbital period in days and on the y-axis the absolute mass of the planet in Jupiter masses. Both axes are in log scale. For clarity, only the object discovered using the Transit, RV and astrometry methods are shown, they are color-coded in blue, orange and red respectively. The Triangles indicate absolute masses and the circles lower mass limits. The Brown Dwarf Regime and Stellar Regime are highlighted using gray and black. Again for clarity, I have shown the population twice — Once without and once with the Gaia ASOIs and the Gaia detection limits. The Gaia ASOIs are denoted with yellow stars. Two of them are highlighted with a black outline, which are Gaia-5b (left object in the Brown Dwarf regime) and Gaia-4b (right object on the border of the Brown Dwarf regime). The masses of the ASOIs are calculated as described by Section 3. A rough estimation of the Gaia detection limits are highlighted using light blue, blue and dark blue, for Gaia DR3 - DR4 and DR5 and is adapted from Feng (2024). Objects enclosed in those regions could be detected by Gaia assuming the host star is sun-like and at a distance of 10 parsec. The same dataset is used as in Figure 1.2.

1.1.2 Jupiter Desert

The Jupiter desert refers to a lack of exoplanets found in a different parameter space, as described by [Stefánsson et al. \(2025\)](#). In Figure 1.7 we see the mass of the star plotted against the mass of the planet and the mass ratio, with both y-axes in log scale. In the histogram we see the distribution of the masses shown in the top scatter plot. There is a clear lack of supermassive planets ($M_p > 1M_j$) that orbit around low-mass stars ($M_\star < 0.3M_\odot$). This is not due to the lack of low-mass stars that we can observe. The solar neighborhood is littered with M-dwarfs. These are the smallest object still classified as star and range from around $0.6 M_\odot$ to around $0.1 M_\odot$. In Figure 1.8 we see a histogram of all the stars within 10 parsecs. They clearly stand out as the most abundant. This clearly shows that this lack of planets in the Jupiter desert is not due to the lack of targets. Quite the opposite, given that there is an overabundance of low-mass stars nearby, this area stands out as interesting. This gap is likely due to the formation processes of such objects, which are not favorable. It has been speculated to be a dividing line between planet formation and brown dwarf formation mechanisms [Stefánsson et al. \(2025\)](#). Exoplanets within the Jupiter desert could provide key insights into these mechanisms. Luckily, they are easy to detect. Such objects would give of a massive astrometric/RV signal (depending on their orbital period).

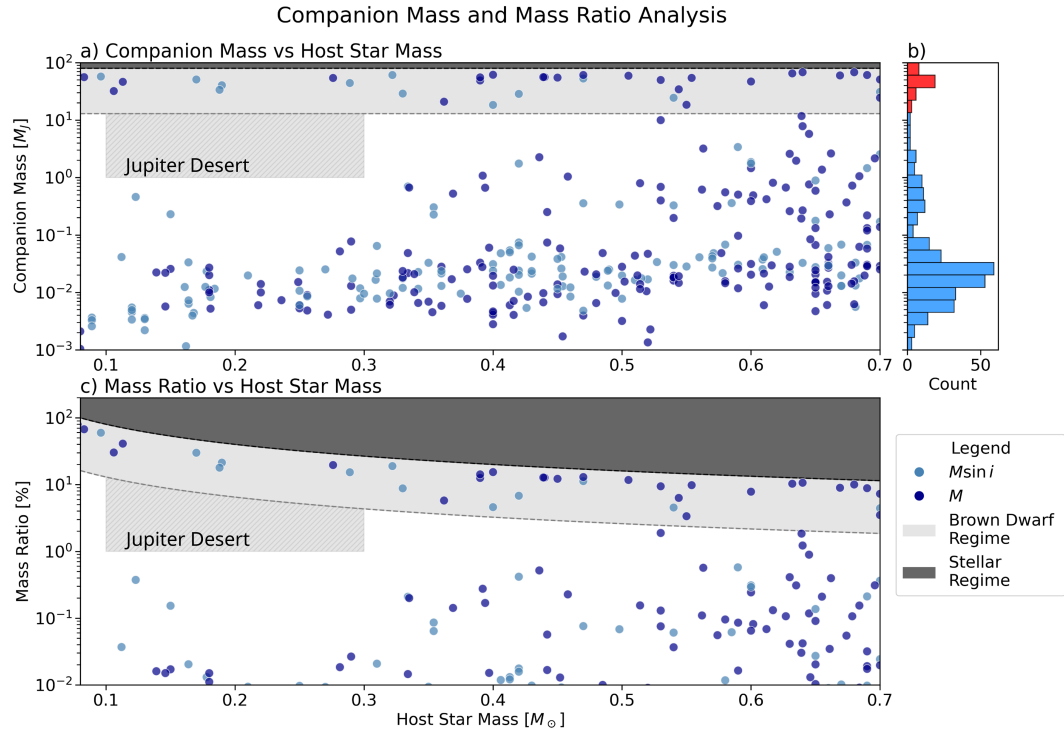


FIG. 1.7 – a) Scatter plot of confirmed exoplanets. On the x-axis the mass of the host star is shown in solar masses and on the y-axis the log-scaled mass of the companion is shown in Jupiter masses. The Triangles indicates the absolute mass and the dots indicates a lower-mass limit. The year of discovery is color-coded, with darker colors representing recent discoveries and lighter colors older ones. The light-gray shaded area represents the brown dwarf regime and the darker-gray shaded area the stellar regime. The striped gray area is the Jupiter desert. b) a histogram which represents the companion mass distribution of the plotted exoplanets. Red indicates brown dwarf companions and blue indicates planet companions. c) Scatter-plot with the same x-axis but now with the y-axis showing the mass ratio in log scale, the color scheme is the same as in the figure above.

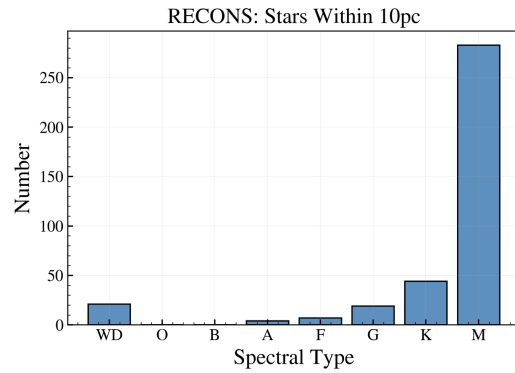


FIG. 1.8 – A bar-graph of the different spectral types of all the stars within 10 parsecs. M-dwarfs are significantly more represent in the solar neighborhood than the other spectral types. This trend continues outside the solar neighborhood. The figure is adapted from [Stefansson \(2025\)](#).

1.2 Gaia spacecraft

The Gaia spacecraft, launched in 2013, has taken high-accuracy astrometric data of 1.5 billion sources. This is an enormous improvement over its predecessor, Hipparcos. Another improvement on the Hipparcos mission: the data is freely accessible by anyone who wants to use it ([The Gaia Collaboration et al. 2016](#)). During the writing of this thesis, Gaia has finished taking measurements, spending its final years processing the data ([The European Space Agency \[ESA\] 2025](#)). Currently, we are waiting for the fourth data release (DR4), which will be made public around the summer of 2026. The final data release (DR5) will arrive before 2031. DR4 will improve upon the measurements released so far in third data release (DR3). It will contain 66 months' worth of data compared to the 34 months of DR3 [The European Space Agency \[ESA\] \(2023\)](#). The design of the Gaia mission has been mainly influenced by the primary scientific goal: Mapping the structure, dynamics and evolution of the milky way. However, the scope of Gaia far exceeded any one field within astronomy ([The Gaia Collaboration et al. 2016](#)). It has been described as "the discovery machine of the decade".

1.2.1 Instruments and Scanning Law

The Gaia spacecraft has been extensively documented ([Vallenari et al. 2023; Feng 2024; Perryman 2012](#)). It is equipped with two (mirror-based) telescopes, separated at an angle of 106.5 degrees. As the satellite rotates, with a rate of 60 arcseconds per second, light passes through the two telescopes and is gathered on the same focal plane. As the light moves across this plane, it passes through three different instruments: a spectrometer, a photometer and an astrometric instrument. This setup ensure every object gets measured twice, once when the object passes through the first telescope (the preceding field of view) and then, 106.5 minutes later, by the second telescope (the following field of view). If only a single telescope was used, Gaia would only be able to measure the shift in position relative to object within the field of view, which is extremely small. Using the second telescope, a comparison can be made with a object that is not within the current field of view. Over time, a true 3-dimensional map can be made.

The full movement of Gaia is described by the scanning law. Gaia maintains an angle of 45 degrees relative to the Sun and its instrumentation. In addition to the previously mentioned rotation speed, the spin axis slowly precesses, completing a full rotation every 63 days. As Gaia moves around the Sun (and around the second Lagrange point), it covers the entire sky in around 3-4 months. This intricate motion is necessary to optimize the sensitivity of the instruments onboard. Gaia is most sensitive in the along-scan (AL) direction, which is the same direction the telescopes are moving in. Perpendicular we have the across-scan (AC) direction, which is less

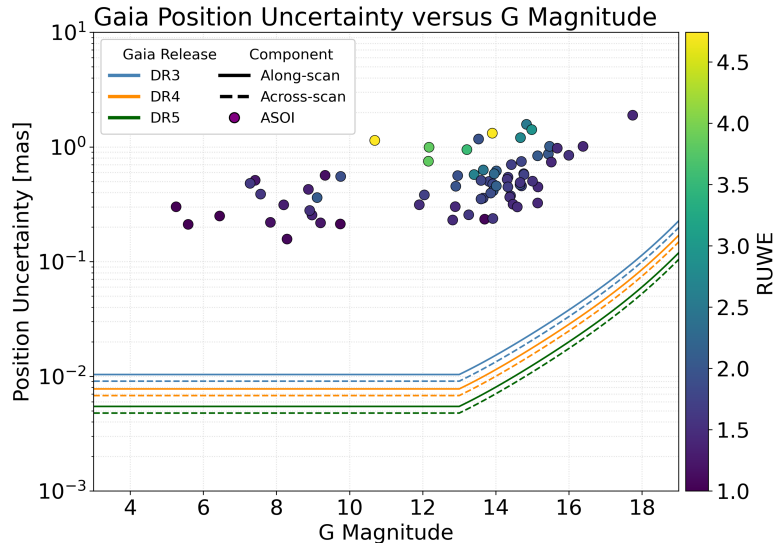


FIG. 1.9 – The astrometric precision of Gaia DR3, DR4, and DR5 (color-coded). The solid lines represent the uncertainty in the along-scan and the dashed lines in the across-scan. On the x-axis we see visual magnitude in the G-band and on the y-axis we see the uncertainty on the measurement in milliarcseconds (log-scale). The dots represent the ASOIs and are color coded based on their RUWE parameter. The uncertainties are generated by the PyGaia Python library ([Brown 2024](#))

sensitive. In practice, all objects are measured in a linear combination of the AL and AC direction. The precession ensures that these measurements are taken in multiple orientations.

The astrometric instrument utilizes photometric data in the G-band (ranging from 330-1050 nm) to determine the parallax and proper motion of all objects in the sky down to a magnitude of $M_G = 20$. The precision depends on the brightness of the object, with more luminous sources being measured more precisely than less luminous ones. Gaia measures the same object multiple times to determine the parallax and proper motion to milliarc precision. On average, each object passes through the instrument 12 times a year. This results in better-constrained values with each new data release. In Figure 1.9 we see the precision of the position uncertainty in both the along-scan and the across-scan for different data releases. In addition we see the ASOIs, well above the uncertainties.

Gaia has the capability of measuring photometric data in two bands. The blue photometer (BP) ranges from 330 to 680 nm and the red photometer (RP) from 640 to 1050 nm.

Lastly, the spectrometer onboard Gaia measures multiple Calcium-II lines between 845 and 872 nm and has a resolving power of $R \sim 11700 = \frac{\Delta\lambda}{\lambda}$. The data gathered are essential to the Gaia pipeline, specifically for the subclassification of the Non single-star (NSS) solutions ([The Gaia Collaboration et al. 2023](#)).

1.2.2 The Gaia Exoplanet Candidates

The Gaia exoplanet candidates are a selection of objects from DR3 that are consistent with a planetary companion and are published by [The European Space Agency \[ESA\] \(2022\)](#). The list contains close to 300 objects divided into three categories, TROI, ASOI, and RVOI. These abbreviations refer to the method of detection followed by '-OI', short for 'object of interest'. This work will focus only on the 72 ASOIs that were released as part of DR3. These objects are more consistent with the NSS solution than with the single-star solution, and they were not classified as a spectroscopic or eclipsing binary through other pipelines.

In equation 1.3, we see the astrometric mass function: \mathcal{M}_1 is the mass of the primary (host) star, \mathcal{M}_2 is the mass of the companion, $\frac{F_1}{F_2}$ is the flux ratio of the primary and companion star, respectively, a_0 is the observed semi-major axis of the objects orbit in mas, ϖ is the parallax of the object also in mas, and P is the orbital period of the system in days. Assuming $\frac{F_2}{F_1} = 0$ where appropriate and disregarding the objects where that assumption was not justified, the final ASOI list consists of all objects where $M_2 \leq 20M_j$.

$$f(\mathcal{M}) = (\mathcal{M}_1 + \mathcal{M}_2) \left(\frac{\mathcal{M}_2}{\mathcal{M}_1 + \mathcal{M}_2} - \frac{F_2/F_1}{1 + F_2/F_1} \right)^3 = \frac{(a_0/\varpi)^3}{(P/365.25)^2}, \quad (1.3)$$

To fully appreciate the selection mechanisms, we refer to the methods section, where we will dive into more detail, as well as to the work done by [The Gaia Collaboration et al. \(2023\)](#), from which the key points of the distillation process have been taken.

The current 72 ASOIs is significantly smaller than the predicted couple of thousand by [Casertano et al. \(2008\)](#). This discrepancy is partially caused by the underlying pipeline. One of the metrics used for classifying NSS-solutions is the Renormalized Unit Weight Error (RUWE). This parameter is given by

$$\text{RUWE} = \sqrt{\frac{\sum_i^N \left(\frac{x_{AL,i} - x_{0,i}}{\sigma^2(N-5)} \right)^2}{u(G, C)}}. \quad (1.4)$$

Here, $x_{AL,i}$ is the i -th position measurement in the Along-Scan direction, x_0, i the expected location given a single-star track, σ the error on the measurement, N the number of measurements taken, and $u(G, C)$ a reference value based on the brightness of the object and the color [European Space Agency \[ESA\] & The Gaia Collaboration \(2023\); Pearce \(2022\)](#). Objects for which $\text{RUWE} \simeq 1$ are well described by a single-star track, while object that significantly deviate from 1 are better described by a NSS track. The RUWE can intuitively be described as a measurement of how well the

single-star track deviations are explained by instrumental errors. One of the criteria for NSS solutions is a $\text{RUWE} \geq 1.4$. This however is not the only criteria that must be met. In addition, there are other NSS classification methods (based on the RV measurements for example). Most of the ASOIs do however satisfy this criteria, as seen by Figure 1.9

In Figure 1.10 the current candidate list is shown in a Hertzsprung-Russell diagram (HRD). A significant portion of these exoplanet candidates orbit a possible red dwarf. However, compared to the 2,600 massive exoplanets around M-dwarfs that Gaia was expected to find according to [Sozzetti et al. \(2014\)](#), this seems rather small. Gaia DR4 will certainly help with expanding the current ASOI-list. For some of the brightest targets, it might even negate the need for spectroscopic follow-up observations ([Sozzetti 2025](#)). For these objects the full radial velocity and astrometric time series will give a description of all orbital parameters. [The European Space Agency \[ESA\] \(2023\)](#). But for the fainter targets, this will not be the case and follow-up observations will play a crucial role in determining their nature. Exoplanets within the Jupiter desert will be a prime target for these follow-ups. Gaia DR4 is set to revolutionize the field of exoplanet research. This work is intended as a precursor to this release in the context of exoplanet detection. I will analyze the exoplanet candidates released with DR3 for RV follow-up observations and use the gathered data to determine the nature of these systems. In addition, I will analyze a framework that can be used for the prioritization of the follow-up observations. In Chapter 2 I will describe the methods used to analyze these targets and how the astrometric technique complements the RV technique. In Chapter 3, I will present the data gathered, which will be discussed in Chapter 4. Lastly, in Chapter 5 I will summarize the findings and provide an outlook on the future of the Gaia mission.

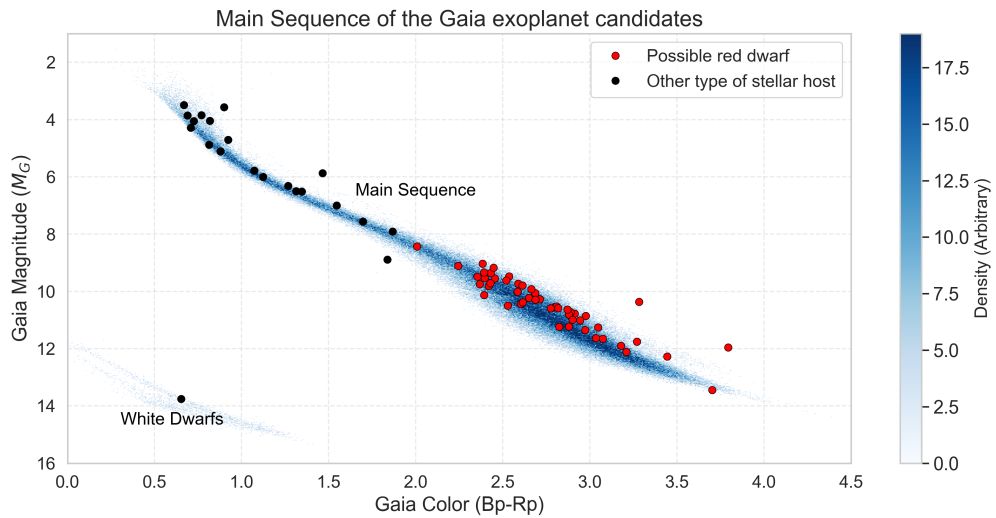


FIG. 1.10 – Hertzsprung-Russell diagram of the Gaia Catalog of Nearby Stars (GCNS), which contains all Gaia measured objects within 200 parsec (The Gaia Collaboration et al. 2021). The exoplanet candidate list is plotted on top of it. The x-axis represents the Gaia Bp-Rp color and y-axis represents the absolute magnitude in the G-band. The exoplanet candidates are split into two groups, 'Possible red dwarfs' and 'Other'. Stellar classification is done by analyzing the spectra of the star. Here it is done based on the Gaia color (Pecaut & Mamajek 2013). There are two clear clumps, the white dwarfs in the lower left corner and the main sequence. The color bar on the side represents the number of stars that can be found in a given area of the HRD. Note that, as expected from Figure 1.8, most stars in our neighborhood are red dwarfs.

Chapter 2

Methods

2.1 Color-Magnitude Diagrams as a Probe of Stellar Properties

Once stars arrive at the main-sequence (MS), they become hydrostatically stable. Over their lifetime, they move around very slowly on this diagram, but this movement is insignificant when compared to their pre- and post-MS evolution. Focusing on very young stellar objects (YSOs), they approach the MS from above, slowly settling in. YSOs are thus elevated from the main sequence. Because unresolved spectroscopic binaries are home to two stars with roughly the same color, we expect these objects to be over-luminous compared to single-star objects. This has been taken into account in the selection process of the ASOI list (for major deviations from the MS the assumption $\frac{F_2}{F_1} = 0$ does not hold), but an in-depth analysis of the objects' properties, including age estimates could give priority to certain targets.

2.1.1 SED fitting

Spectral energy distributions (SEDs) are plots in which we see the star's energy output plotted as a function of the wavelength (or frequency) of light. The main curve is dictated by the blackbody radiation of the star, but due to absorption/emission of light by the stellar atmosphere this curve is littered with features, which depend on the parameters of the star (such as, but not limited to, the mass, radius, and age). To obtain a detailed description of the physical parameters of the target stars, `astroARIADNE` ([Vines & Jenkins 2022](#)), a SED fitting software was used. This software uses Bayesian model averaging techniques to fit photometric data with six different atmospheric models to make a description of the star's SED and physical parameters.

`astroARIADNE` was chosen based on the ease of automatization, the sampling algorithm and because it uses Bayesian Model Averaging techniques (BMA).

Photometric Data

Photometry is a branch of physics that concerns itself with the energy output or measurement over a set wavelength range which is called the bandpass ([Bessell 1990](#)). Using photometry we can measure the brightness of a certain object, for example, the magnitude of a star. The bandpasses are determined by the filters used in the photometer. As light passes through the filters, wavelengths outside the bandpass are removed from the signal. However, the light within the filter range is also affected, a part is removed from the signal. This leads us to the response function of the filters, which describes how much light is let through as a function of wavelength ([Bessell 1990](#); [Kirkby et al. 2024](#)). In Figure 2.1 we see these response functions for the Gaia G , Bp , and Rp filters. When fitting photometric data to a SED, we need to take into account that certain wavelengths will contribute more (or less) to the measured energy than others. `astroARIADNE` uses a convolution of these response functions on the SED models to calculate the flux a given model will produce for a specific filter. These convolutions are described by

$$F_i = \frac{\int f(\lambda) T_i(\lambda) d\lambda}{\int T_i(\lambda) d\lambda}. \quad (2.1)$$

Here, F_b is the flux density (which we measure directly using photometry), $f(\lambda)$ is the SED model and $T_b(\lambda)$ is the response function of the filter used (i) [Alves \(2020\)](#); [Vines & Jenkins \(2022\)](#). The data is fitted using calculated synthetic fluxes, a nested sampling algorithm and an assumed Gaussian (the latter two we will discuss shortly after). The synthetic fluxes SF_i are calculated using the following equation:

$$SF = 10^{-0.4A_i} \cdot S(T_{\text{eff}}, \log g, [\text{Fe}/\text{H}]) \cdot \left(\frac{R}{D}\right)^2 + \epsilon_i. \quad (2.2)$$

It is composed of several terms.

- A_i : The extinction factor for the filter used. As light traverses the distance between the emitter and the instrument, it passes through the interstellar medium. This leads to extinction — and in some cases, emission — at specific wavelengths. Because the extinction is highly dependent on the wavelength, the selective absorption (R_v) is used to describe how the interstellar extinction

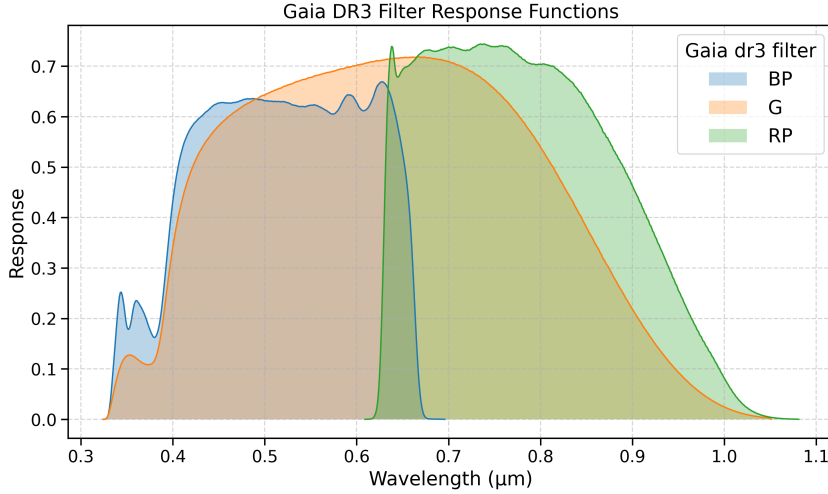


FIG. 2.1 – The response function of the Gaia DR3 filters (denoted by color). With on the x-axis, the wavelength in micron and on the y-axis the response of the filter. This can be viewed as a percentage of light that passes through the filter. Note that outside the filter ranges, the response is zero. Also, note how within the filter range, the response function is not uniform. Figure is generated using the `Speclite` (Kirkby et al. 2024) software

changes over the filter range. This value is fixed to 3.9. `astroARIADNE` has incorporated four different extinction laws and five different dust-maps. For further detail on the implementation of the dustmaps and extinction laws, we refer to the work done by Vines & Jenkins (2022). In this work, we solely incorporated the Fitzpatrick extinction law (Fitzpatrick 1999) and the SFD dustmap (Schlafly & Finkbeiner 2011).

- $S(T_{\text{eff}}, \log g, [\text{Fe}/\text{H}])$: The model grid interpolated in $T_{\text{eff}} - \log g - [\text{Fe}/\text{H}]$ space represents the convolution of the SED over the filter response function and is the stellar flux at its surface. It is a function of the effective temperature, stellar surface gravity, and metallicity (T_{eff} , $\log g$ and $[\text{Fe}/\text{H}]$ respectively).
- $(\frac{R}{D})^2$: A normalization factor to account for the dilution caused by the inverse-square law. R is the radius of the star and D the distance.
- ϵ_i : An additional noise term for each filter i . This term is used to mitigate any additional noise not described by the error on the measurement (such as stellar variability). It is comprised of the measurement error $\sigma_{i,m}$ and excess noise $\sigma_{e,i}$ and is given by $\epsilon_i^2 = \sigma_{m,i}^2 + \sigma_{e,i}^2$.

Bayesian Model Averaging

Bayesian model averaging is a technique that combines information gathered from multiple models (Fragoso et al. 2018). Normally, we would choose model based on the assumptions made within that model. However, we often do not know which model best describes the data and is physically the most accurate description of the star’s atmosphere. This uncertainty in our model choice can lead to a false sense of security. If we then choose a model that is not representative of the input data we can get great looking results but they are not physically accurate and do not describe our problem. Lastly, it can lead to riskier predictions, as phase transitions or random events can be overlooked or oversimplified by individual models. These problems can be partially negated if our statistical framework allows for the use of multiple models. Given the model assumptions are justifiable, the models should be relatively in agreement with each other. We would not expect two models with reasonable assumptions to give completely different results, and even if they did, it would be interesting to note. This combining procedure is done by simply taking model-weighted averages of the individually fitted parameters. In equation 2.3 we see Bayes’ theorem, the parameter $\hat{\theta}$ represents the set of stellar parameters we are interested in. X represents the data and M the model that is used.

$$P(\hat{\theta} | X, M) = \frac{P(X | \hat{\theta}, M) P(\hat{\theta} | M)}{P(X | M)}. \quad (2.3)$$

The weighted average is described by

$$P(\bar{\theta}) = \sum_{n=1}^N P(\hat{\theta}_n | X, M_n) P(M_n | X) \quad (2.4)$$

With the model likelihood being

$$P(M_j | X) = \frac{P(X | M_j) P(M_j)}{\sum_{n=1}^N P(X | M_n) P(M_n)} \quad (2.5)$$

Here `astroARIADNE` makes two assumptions (Vines & Jenkins 2022), firstly every model is a-priori equally viable. Secondly, the likelihood $P(X | M_j)$ is Gaussian:

$$\mathcal{L} = \prod_{i=1}^N \frac{1}{\sqrt{2\pi\epsilon_i^2}} \exp\left(-\frac{1}{2} \left(\frac{f_i - SF_{i,M}}{\epsilon_i}\right)^2\right) \quad (2.6)$$

With f_i , the i-th datapoint, $SF_{i,M}$ the interpolated model flux of the fitted star and ϵ_i the noise term.

The models that `astroARIADNE` uses are: Phoenix v2 (Husser et al. 2013), BT-Settl, BT-Cond, BT-NextGen (Allard et al. (2012)), Hauschildt et al. (1999) Kurucz

(Kurucz 1993), and Castelli & Kurucz (Castelli & Kurucz 2003). All of these models are built upon different assumptions of the microphysics of the star. Since the BT-models are identical for stars with an effective temperature greater than $4000K$, only the BT-Settl model is used if the prior temperature exceeds this, to avoid artificial double counting. On the other hand, the Kurucz and Castelli & Kurucz models are disabled for stars with an effective temperature lower than $4000K$ due to the known unreliability of those models for colder stars.

Nested Sampling

Nested Sampling is a Monte Carlo method used to describe both the marginal likelihood and the posterior of a given set of parameters (Buchner 2023; Kent 2020). Bayes' theorem can be rewritten as

$$P = \frac{\mathcal{L}\pi}{\mathcal{Z}}, \quad (2.7)$$

with the marginal likelihood:

$$\mathcal{Z} = \int P(D | \theta) \pi(\theta) d\theta. \quad (2.8)$$

This term can be ignored in single-model evaluations by using maximum likelihood methods, as this only acts as a normalizing term. However, if we want to compare different models to each other we need to normalize the posterior distributions, which becomes problematic when we increase the dimensionality of θ . Nested sampling solves this by transforming \mathcal{Z} into a one-dimensional integral. The prior mass X is divided into chunks $dX = \pi d\theta$, so we define:

$$X(\lambda) = \int_{L(\theta) > \lambda} \pi(\theta) d\theta. \quad (2.9)$$

Which is the total prior mass where the likelihood $L(\theta)$ is greater than a given probability λ . Since this function is monotonically increasing, we can write the inverse as

$$\lambda(X) = \mathcal{L}(X). \quad (2.10)$$

Which can be interpreted as the likelihood at which encloses a given prior mass X . At $\lambda = 0$, we integrate over the entire prior distribution, thus $X(\lambda = 0) = 1$. The opposite happens when $\lambda = 1$, there is no likelihood greater than 1 so $X(\lambda = 1) = 0$.

Now we can rewrite the marginal likelihood as a integral over the prior mass with $dX = \pi d\theta$:

$$\mathcal{Z} = \int_0^1 L_{min}(X) dX. \quad (2.11)$$

This integral is easier to compute numerically than the previous one. Because the shrinkage of X_i to X_{i+1} is statistically well characterized, as it behaves like a beta distribution. So instead of sampling from the prior directly we sample from the prior mass X . The algorithm works as follows:

1. Sample N live points directly from the priors given and calculate the likelihood for each point.
2. Save and remove the live points with the lowest likelihood, these correspond; to the worst fit and contribute $1/N$ of the total volume of $X(\lambda_i)$
3. Replace the removed point by a new live point with the restriction that the likelihood of the new point is greater than the removed one.
4. As we repeat step 2 and 3 the enclosed volume shrinks and the likelihood goes up, but every removed point removes less volume than the previous one. Once the volume removed subcedes some reference value, we stop this process.
5. The integral can now be approximated as $\Delta V_i * L_i$

There are some details that are not discussed in this work, for example: finding a new live point that has a higher likelihood than the previous dead point becomes increasingly problematic as λ increases. For a more in-depth explanation, we refer to [Buchner \(2023\)](#) and to [Speagle \(2020\)](#). Nested sampling, compared to other tools such as Markov Chain Monte Carlo (MCMC), naturally handles bimodal distributions as it does not restrict itself to a certain parameter space. Nested sampling also provides a clearly defined stopping criterion often called $d \log(\mathcal{Z})$. The lower this criterion, the longer and more precise our marginal likelihood gets defined. Lastly, nested sampling handles model comparison very well as it gives a direct way to calculate the marginal likelihood function ([Speagle 2020](#)).

Application

Using `astroARIADNE`, we define a `star` object with a given Right Ascension (RA), Declination (DEC), and Gaia ID. It then uses `ASTROQUERY` ([Ginsburg et al. 2019](#)) to query all available photometric and prior data of the target. In Table 2.1 we see the required prior data and their respective sources (the same table for the photometric data can be found in Table A.2 in the appendix). The priors can be overwritten if

we have a better estimate. Each model is then fitted independently, after which the model probabilities are calculated using Bayesian Model Averaging. These model probabilities can be used in two different ways, the *averaging* method and the *sampling* method. In the averaging method, the best-fitting parameters are directly calculated by averaging (weighted by the likelihood) over the posteriors. The sampling method first creates a master posterior from the model posteriors (weighted again by the likelihood) and resamples from this distribution to retrieve the best-fitting parameters. The averaging technique can generate very precise values, but if the models disagree, it can result in a best-fitting parameter that is not supported by any single model. The sampling method is better suited in those cases but in return is less precise.

In context of the ASOIs, SED fitting is a valuable tool because we lack key sources of data, such as spectroscopic measurements. They are however measured in all-sky photometric surveys. For single-star systems, the SED fitting constrains the stellar parameters, but for binary systems, the fitting will not represent the system in the slightest. The stellar parameters found in the literature is found under the assumption of singularity. Processing differences between SED fitting and these literature data could trickle down in the parameters. In addition, the noise terms — which are added to account for stellar variability — could be correlated with multiplicity. Lastly, there could be an excess in the redder filters.

TABLE 2.1 Overview of `astroARIADNE` input and output parameters. g_* and σ_{g_*} refer to the MIST estimate of the queried star; D_* and $D_{e,*}$ to the distance and uncertainty from [Bailer-Jones et al. \(2018\)](#); and av to the maximum optical extinction from the Schlegel, Finkbeiner & Davis (SFD) dust map ([Schlafly & Finkbeiner 2011](#)). RAVE refers to the fifth data release from the RAVE survey ([Kunder et al. 2017](#)). Isochrone interpolation uses the `ISOCHRONE` Python package and MIST tracks ([Morton 2015](#); [Dotter 2016](#)). Stellar mass is obtained both directly from $\log g_*$ and via isochrone interpolation. \mathcal{N} and \mathcal{U} represent a normal distribution and a uniform distribution respectively.

Parameter	Description	Prior	Fitted
T_{eff}	Effective temperature (K)	RAVE	Directly
$\log g$	Surface gravity (g_\odot)	$\mathcal{N}(g_*, \sigma_{g_*}^2)$	Directly
[Fe/H]	Metallicity (z_\odot)	$\mathcal{N}(-0.125, 0.234^2)$	Directly
D	Distance (pc)	$\mathcal{N}(D_*, (5D_{e,*})^2)$	Directly
R_*	Stellar radius (R_\odot)	$\mathcal{U}(0.05, 100)$	Directly
A_V	Interstellar optical extinction	$\mathcal{U}(0, av)$	Directly
Age	Age of the object	N/A	Isochrone interpolation
Mass	Stellar mass (M_\odot)	N/A	Isochrone interpolation and indirectly fitted

2.2 Observations of ASOIs

As of writing the thesis, the radial velocity follow-up observations are still ongoing. They are actively being observed by multiple high-resolution spectrographs, namely, the NEID ('NN-EXPLORE Exoplanet Investigations with Doppler Spectroscopy') spectrograph mounted on the WIYN 3.50-meter Telescope, the Habitable Zone Planet

Finder (HPF) spectrograph mounted on the Hobby-Eberly Telescope and both the HARPS (High Accuracy Radial velocity Planet Searcher) and the NIRPS (Near Infra Red Planet Searcher) spectrographs mounted on the ESO 3.6-meter telescope. In Table 2.2 we see a complete overview of the instruments.

TABLE 2.2 Overview of the instruments used for follow-up observations of the *Gaia* exoplanet candidates (Stefansson 2019; European Southern Observatory (ESO) 2022, 2002). Observatory names have been shortened: Kitt Peak¹, McDonald², and La Silla³ refer to Kitt Peak National Observatory (Arizona, U.S.), McDonald Observatory (Texas, U.S.), and La Silla Observatory (Chile), respectively.

Instrument	Telescope	Observatory	Resolution (R)	Wavelength Range (nm)
NEID	WIYN 3.5-meter	Kitt Peak ¹	$\sim 60,000$	380–930
HPF	Hobby-Eberly	McDonald ²	50,000	840–1300
NIRPS	ESO 3.6-meter	La Silla ³	$\sim 80,000$	950–1800
HARPS	ESO 3.6-meter	La Silla ³	120,000	378–691

2.2.1 RV Precision

At the foundation of the RV technique lies the Doppler shift of a photon due to the relative motion of the emitting object. The method is extensively used and well-studied (Trifonov 2024; Hara & Ford 2023; Stefansson 2019). The shift in wavelength is described by:

$$\lambda = \lambda_0 \left(1 + \frac{1}{c} \mathbf{k} \cdot \mathbf{v}_{obs}\right). \quad (2.12)$$

Here, λ is the wavelength of the measured photon, λ_0 the wavelength of the unshifted photon, \mathbf{k} the unit vector pointing from the observer to the source, and lastly, \mathbf{v}_{obs} the velocity of the source. Relativistic effects are ignored in this case. Ground-based observations are mostly done in optical and near infrared bands due to the effects of the atmosphere of the earth on ultraviolet and infrared light. The atmosphere of the earth absorbs and emits mostly in this part of the spectrum, which makes observations in these filters near impossible. Due to absorption in the atmosphere of the source, spectral lines are introduced. For hot star (with an effective temperature exceeding 10,000K), which typically have virtually no spectral lines in both the optical and near infrared, ground-based telescopes are unsuited for precise RV measurements. The signal-to-noise ratio (SNR) is also depended on the brightness of the object, the brighter the object the better the SNR. Cooler stars, even though they are less bright, usually contain a plethora of spectral lines which can be used to accurately determine the RV. Theoretically, the spectral lines occur at well-known rest-frame wavelengths. Due to natural effects, such as stellar rotation, winds, and the quantum uncertainty principle, these lines become broadened. The full width at

half maximum (FWHM) is used to describe how much a specific line is broadened, and as the name implies is the width of the line at half of the maximum depth. In the end, the precision of the measurement depends on the SNR (which is dependent on both the temperature and the brightness), the FWHM (broader lines making the measurement less precise) and the relative depth of the line (with deeper lines making the measurement more precise). In addition to the spectral information, the design of the instrument also affects the precision, the resolving power (R) is a measure of how detailed an instrument can measure a shift in wavelength $\Delta\lambda$ at wavelength λ and is easily described by $R = \frac{\lambda}{\Delta\lambda}$. The higher the resolving power, the more precisely an instrument can measure a change in wavelength. Other factors that can impact the precision of the instruments are thermal expansion and air pressure changes near the instrument among others. The specifics of each instrument are listed in Table 2.2. To calculate the expected instrument-specific precision, a publicly available code was used ([Stefansson 2018, 2024](#)).

2.2.2 Broadening Functions

A simplistic case of a spectrum would be one where its spectrum is disturbed only at precise frequencies. But as previously mentioned, once we take into account the star's rotation, turbulence in the atmosphere or instrumentation broadening, our perfect spectral feature will be broadened over a range of frequencies. Our perfect spectrum gets convolved by a 'broadening function'. Using this broadening function and a template spectrum, it is possible to gain information about the system based on how they are broadened (i.e. the shape of the spectral lines; [Yi \(2024\)](#)). In our case, we can see if an emission line is both blue- and red-shifted at the same time. In Figure 2.2 we see a binary broadening function over multiple phases. We can clearly see that the gray (measured) broadening function seems to split into two solutions as the orbit progresses. An important note is that these graphs cannot be interpreted as a probability density function (PDF), the height of the broadening function is mainly determined by the flux of the star, which can be ignored for our purposes. Once the spectra are measured, a binary broadening function is applied to them to recover the RV data of the individual components.

2.2.3 Astrometry and RV Interplay

Gaia astrometry measures the angular displacement of a star projected on the sky due to its motion around the barycenter of the system ([The Gaia Collaboration 2023](#)). The coordinates of the system are described by

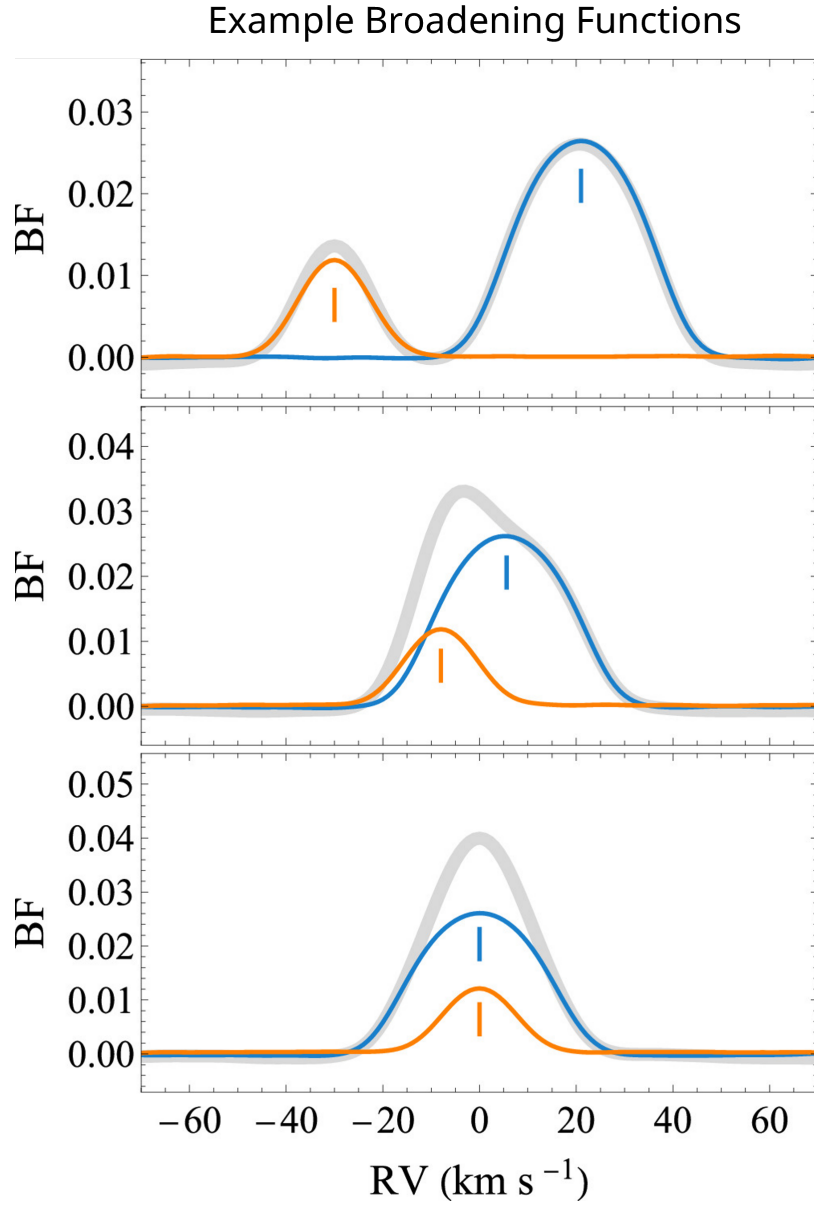


FIG. 2.2 – Figure adapted from [Yi \(2024\)](#). This figure shows the radial velocity (x-axis in km/s) plotted against mock broadening functions (y-axis) for a binary star system observed at three different orbital phases. The orange and blue curves represent the individual broadening functions of the two stellar components, while the gray curve represents the combined (measured) broadening function.

$$\Delta\alpha(t) = Bx(t) + Gy(t), \quad (2.13)$$

$$\Delta\delta(t) = Ax(t) + Fy(t), \quad (2.14)$$

$$x(t) = \cos[E(t)] - e, \quad (2.15)$$

$$y(t) = \sqrt{1 - e^2} \sin[E(t)], \quad (2.16)$$

Here, $\Delta\alpha$ and $\Delta\delta$ represent the displacement of the object (in the Right Ascension, and Declination respectively), x and y represent the Cartesian coordinates of a normalized top-down view of the system. $E(t)$ represents the eccentric anomaly and A, B, F and G are the Thiele-Innes coefficients. These are given by

$$A = a_0 (\cos \omega \cos \Omega - \sin \omega \sin \Omega \cos i) \quad (2.17)$$

$$B = a_0 (\cos \omega \sin \Omega + \sin \omega \cos \Omega \cos i) \quad (2.18)$$

$$F = -a_0 (\sin \omega \cos \Omega + \cos \omega \sin \Omega \cos i) \quad (2.19)$$

$$G = -a_0 (\sin \omega \sin \Omega - \cos \omega \cos \Omega \cos i) \quad (2.20)$$

Where ω is the argument of periastron, Ω is the longitude of ascending node, i the inclination and a_0 the semi-major axis as defined by Equation 1.1. In Figure 2.3 we see these parameters in a heliocentric perspective for an example system (with an arbitrary scaling) near the celestial north-pole. In Figure 2.4 a zoomed-in view is given of the system-specific parameters (of a different example system). Gaia derives orbital solutions by fitting for the Thiele-Innes constants A, B, F , and G as well as the eccentricity e , orbital period P , and time of periastron passage t_p . Using these Thiele Innes coefficients we can retrieve the semi-major axis and the inclination ([Emelyanov & Kondratyev 2022](#); [European Space Agency \[ESA\] & The Gaia Collaboration 2023](#)) using:

$$a_0 = \sqrt{u + \sqrt{u^2 - v^2}} \quad (2.21)$$

$$\cos i = \frac{v}{a_0^2} \quad (2.22)$$

$$(2.23)$$

with

$$u = \frac{1}{2} (A^2 + B^2 + F^2 + G^2) \quad (2.24)$$

$$v = AG - BF. \quad (2.25)$$

The motion in the radial direction is expressed as: ([European Space Agency \[ESA\] & The Gaia Collaboration 2023](#))

$$\text{RV}(t) = \gamma + K [\cos(\nu(t) + \omega) + e \cos(\omega)], \quad (2.26)$$

Orbital parameters from a heliocentric view

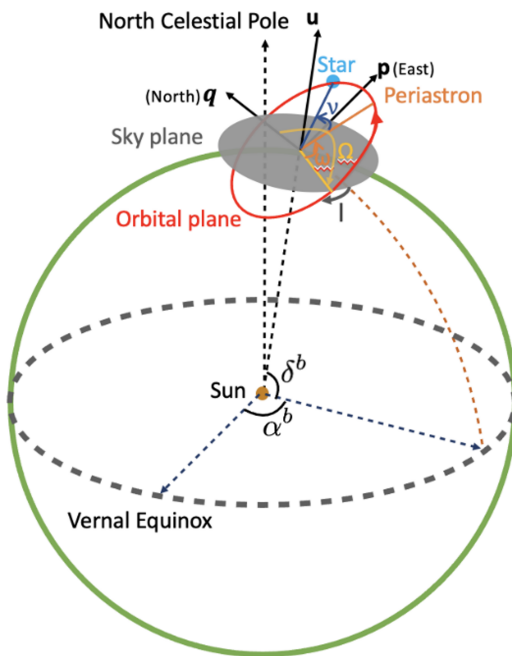


FIG. 2.3 – Figure adapted from Feng (2024). A representation of some of the parameters used in the astrometric technique from a heliocentric point-of-view. On top, an enhanced mock system is shown. A similar system is shown in Figure 2.4.

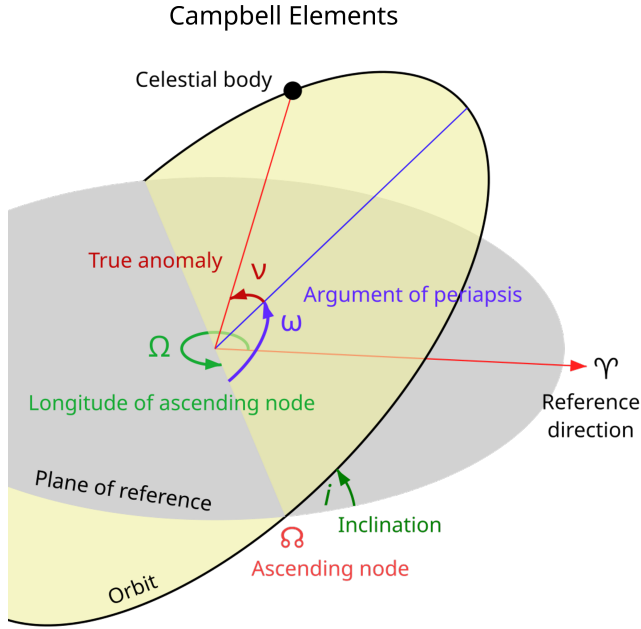


FIG. 2.4 – Figure adapted from [Lasunsky \(2007\)](#), showing multiple system-specific parameters used in the astrometric technique. The system represented is not the same as in Figure 2.3 but can be viewed as a zoomed in representation of the system parameters of that figure. Note that the Gaia solution are given using the Thiele-Ines framework, here we see the Campbell elements.

with γ , K and ν being the barycentric radial velocity, the RV amplitude and the true anomaly. The latter is given by $\nu(t) = \arccos\left(\frac{\cos(E(t))-e}{1-e\cos(E(t))}\right)$. The RV amplitude K_1 is given by:

$$K_{1,2} = \left(\frac{2\pi G}{P}\right)^{1/3} \cdot \frac{m_{2,1} \sin i}{(m_1 + m_2)^{2/3}} \cdot \frac{1}{\sqrt{1 - e^2}}. \quad (2.27)$$

Assuming the flux ratio is zero this can be rewritten in terms of the Gaia parameters:

$$K = \frac{2\pi}{P} \frac{(a_o/\varpi)\sqrt{1 - \cos^2 I}}{\sqrt{1 - e^2}}, \quad (2.28)$$

with ϖ , the parallax. As mentioned in the introduction, using RV, we can only find a minimum mass due to the $\sin i$ in this equation. Furthermore, the ratio of the amplitudes gives the mass ratio $\frac{K_1}{K_2} = \frac{m_2}{m_1} = q$. This allows us to find both masses, given we know the inclination, by substituting $m_2 = qm_1$. This results in the binary

mass function:

$$m_2 = \left[\frac{K_1(1+q)^{2/3}\sqrt{1-e^2}}{\left(\frac{2\pi G}{P}\right)^{1/3} \sin i} \right]^3 \quad (2.29)$$

Retrieving the Flux-ratio from RV

Given that the system is a spectroscopic binary, we can retrieve ϵ from the RV data, using Equation 1.2. We then consult a stellar type table to infer the expected fluxes of both stars. Finally, using Equation 1.2 we can calculate the expected flux-ratio ϵ . This approach serves as both a consistency check and a diagnostic tool. For sub-stellar companions, the flux-ratio should approach zero. Moreover, we are able to invert this method. Given a flux-ratio ϵ and masses m_1, m_2 , we can recover the semi-major axis and assess its consistency with the orbital parameters derived by Gaia. In this work, we adopted the Mamajek Table ([Pecaut & Mamajek 2013](#)), which is a table containing stellar parameters for objects ranging from massive O-type stars to sub-stellar Y4-type brown dwarfs and is well known in the field.

Chapter 3

Results

In this section, we present the results of our analysis based on the methods outlined in Section 2.

3.0.1 Observation Proposal

To prepare and contribute to the observational proposals for time on the telescopes mentioned in Table 2.2, I analyzed the ASOIs on their viability as potential targets and calculated the expected RV signal and the mass of the companion given that the assumption $F_2/F_1 = 0$ holds true. In addition, I made efforts to find targets beyond the current ASOI list.

Updating and Expanding the ASOI List

The ASOI list is generated using the NSS solution dataset with a restriction on the astrometric mass function ($f(\mathcal{M}) \leq 20M_j$ (The Gaia Collaboration et al. 2023)). We made efforts to expanding this list in two ways.

Firstly, Sahlmann & Gómez (2025), developed a machine-learning algorithm that uses literature data to classify the NSS solutions into two groups, stellar and sub-stellar companion hosting systems. The preliminary results of this study were considered in our target selection procedure. Although the paper, dataset, and algorithm were unpublished at the time, an early version was available on arXiv (Sahlmann & Gómez 2024). We specifically took note of Table 4, which lists the most promising sub-stellar companions. The early M-dwarf BD+75 510 stood out due to its strong classification score and a low companion mass estimate (below $13M_j$). HD 40503, a K2V star, also appeared notable for similar reasons. Although it is not an M-dwarf,

its relatively low stellar mass made it a compelling target for further consideration.

Secondly, because the ASOI list was created with the mass function restriction, other potentially interesting targets were not included. [The Gaia Collaboration et al. \(2023\)](#) notes that 1843 brown dwarf candidates were found. The binary mass function for these objects is restricted to $20M_j \leq f(\mathcal{M}) \leq 80M_j$. The study in question also describes the contents of the 'binary masses' table. It describes in detail how a Markov Chain Monte Carlo (MCMC) simulation was used to calculate an expected flux-ratio. We queried this table for targets with a lower bound flux-ratio of zero or lower. From this list we selected all targets with a host star mass lower than $0.7M_\odot$ and a companion mass lower than $80M_j$. The resulting objects underwent the selection procedure, which we will now describe.

Expected Signature

First, we retrieved the expected RV-curve. We used the `Gorp` python library to calculate the masses of host stars. This library uses a high-quality mass-luminosity scaling law to retrieve a stellar mass from a given luminosity. In our case, the absolute Gaia RP magnitude was chosen. Gaia, for some objects, also lists a mass. This pipeline is called FLAME ('Final Luminosity Age Mass Estimator'), but only a handful of targets in the ASOI list have such a mass. This is due to selection requirements set by this pipeline ([European Space Agency \[ESA\] & The Gaia Collaboration 2023](#)). A similar restriction was encountered using the `GORP` masses library, as some RP magnitudes were outside of the interpolation range. This led to an inability to calculate the stellar and companion mass for seven targets.

To see if our results aligned with expectations, a comparison was made with Gaia's FLAME masses. In Figure 3.1 we see this comparison and as expected, the masses agree, with the `Gorp`-masses being slightly more conservative. Note that this graph is based on a randomly selected subset of objects within 100 parsecs and does not represent the ASOI-list.

The RV amplitude was calculated using equation 2.28. Then, together with the `Gorp`-masses, the companion mass was calculated using the `radvel` library ([Fulton & Petigura 2017](#)). The resulting data were used to create an expected RV curve of the systems over the observing windows. The RV curves were used by the research team to determine the optimal timing for taking measurements for the given targets. The resulting RV curves can be found in the supplementary file. In Figure 3.2 we see the ASOI candidates represented in the Jupiter desert. The plot reveals several promising targets for follow-up observations that may help populate the Jupiter Desert.

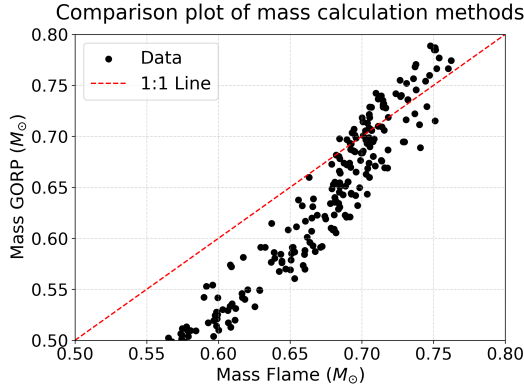


FIG. 3.1 – A comparison plot of the object masses calculated with Gaia’s internal pipeline (Flame) and the `GORP` library. With on the x-axis the FLAME mass and on the y-axis the `gorp` mass. The objects shown are a random subset of stars within 100 parsec. The red line shows the 1:1 equality.

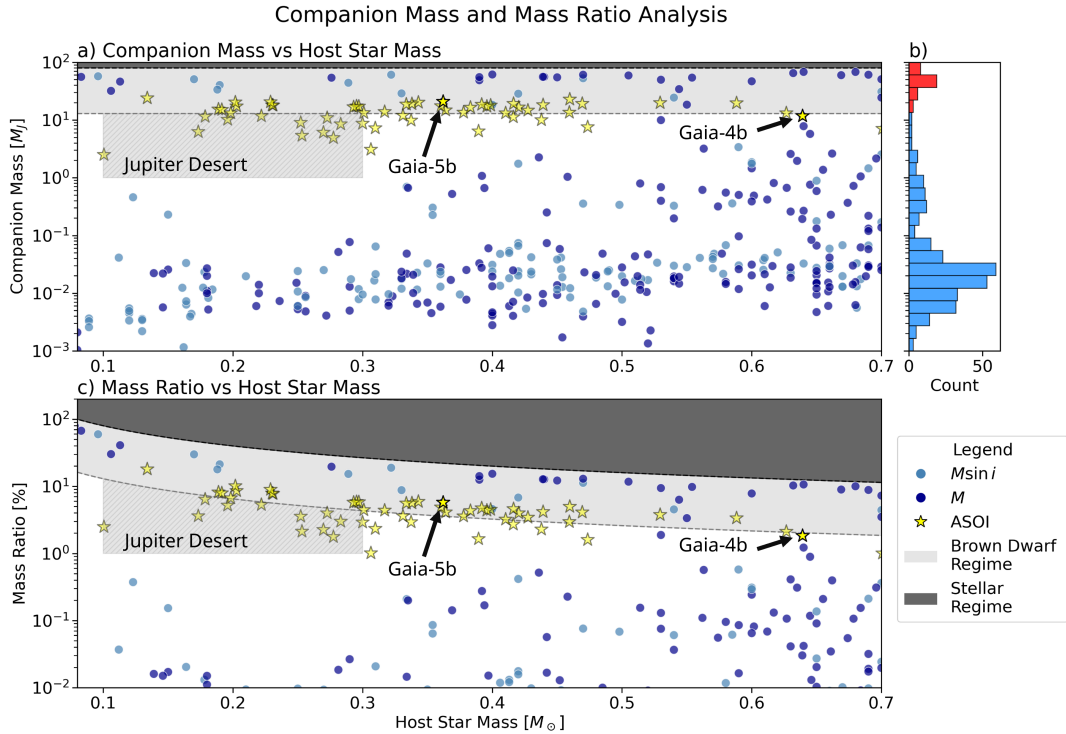


FIG. 3.2 – Same figure as Figure 1.7, now with the addition of the ASOI candidates represented with yellow stars. The histogram in panel b only shows the confirmed exoplanets. A) Scatter plot of confirmed exoplanets. On the x-axis the mass of the host star is shown in Solar masses and on the y-axis the log-scaled mass of the companion is shown in Jupiter masses. In panel b, on the side, a histogram is shown, which represents the companion mass distribution of the plotted exoplanets. C) Scatter-plot with the same x-axis as panel A, but now with the y-axis showing the mass ratio in log scale. The same coloring and marker-scheme is used as in Figure 1.7.

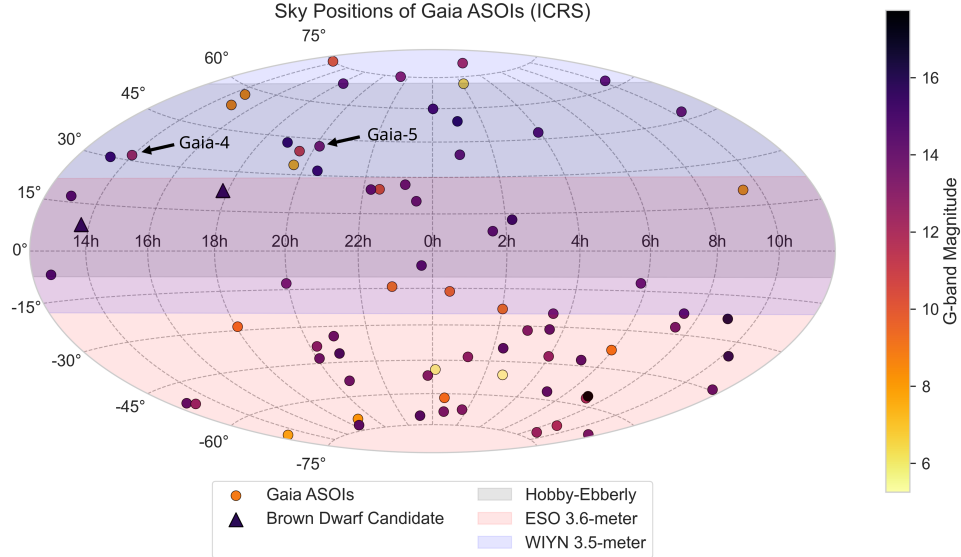


FIG. 3.3 – Sky position of all ASOIs using a Hammer-projection. On the horizontal axis the Right-Ascension, and the vertical axis the Declination. The circles indicate the ASOIs, note that not all ASOIs were selected for follow up. The triangles indicate ‘Brown Dwarf Candidates’ that were followed up and were part of the expanded ASOI list. In Section 4, we discuss these objects in further detail. The coloring-scheme of the objects is done based on the Gaia- G magnitude. In addition, the telescope ranges are highlighted using a underlying color-scheme, with gray indicating the Hobby-Eberly 10-meter telescope, red the ESO 3.6-meter telescope, and blue the WIYN 3.5-meter telescope [European Southern Observatory \(ESO\) \(2022, 2002\)](#); [Stefansson \(2019\)](#).

Observational Viability

All targets were assigned one or more telescopes from which they were measurable. This was largely done based on the declination of the targets. In Figure 3.3 we see an overview of the sky positions all ASOIs, together with an indication of the telescopes capable of observing them. For each telescope and each target, the precision was calculated using the expected RV amplitude, the H , V and J apparent magnitudes and the effective temperature. This was done under the assumption of a 15-minute observation window. If no temperature was available, a polynomial fitted temperature was used. The code for the fitting procedure was supplied by PhD student E. Koo, a member of the research team. The polynomial was based on the `gorp`-masses and the Gaia listed temperature of around 2000 sources within 100 parsec and was weighted according to the inverse square of the mass error. In Figure 3.4 we see the results of this interpolation outlined in the black dots. For targets that deviate from the interpolated red line, the effective temperature was already known from Gaia data. The H band visual magnitude was calculated using the $Rp - Bp$ color, the G band visual magnitude and known scaling laws documented by [European Space Agency \[ESA\] & The Gaia Collaboration \(2023\)](#), and the V and J band visual magnitudes were queried using Vizier ([Ochsenbein et al. 2000](#)). In total, 30 ASOI objects

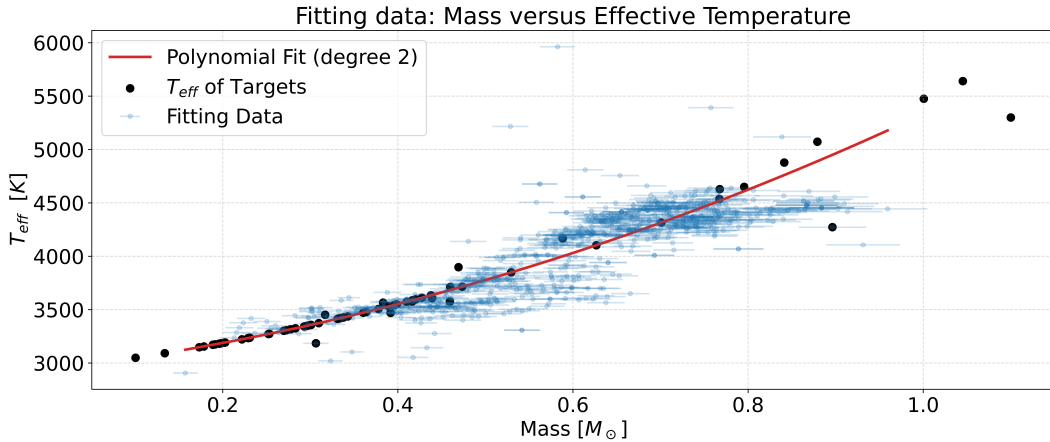


FIG. 3.4 – Scatterplot of the interpolated effective temperature of the ASOI-targets (shown in black). The red line represent the second degree polynomial used and the blue dotted background represents the data used for the fitting procedure. The code used for the fitting procedure was supplied by E. Koo, a member of the research team.

were chosen to be followed-up in this manner. Other candidates that were not chosen were either less luminous (resulting in a low SNR), were not observable during the observation window we applied for, or the companion was expected to be too massive. The observation proposal and the ongoing observations also included other objects, but I have chosen to omit those targets in further analysis since they are beyond the scope of the thesis. In the left panel (a) of Figure 3.5 we see the expected SNR for the ASOI objects chosen for follow-up observations, with markers indicating the different spectrographs used for the follow-ups. It is clearly visible that these targets have a sufficient signal-to-noise ratio to be considered for follow-up observations. The signal-to-noise ratio is typically in between one hundred and one thousand for the candidates. In the right panel (b) of Figure 3.5, we see a period-mass scatter plot for the selected targets. Most targets have an orbital period in the order of a few hundred days. Their masses are near the deuterium fusion limit ($13M_j$).

3.0.2 SED Fitting using astroARIADNE

For this work, we primarily adopted the default configuration provided in the `astroARIADNE` example script. In which the `dynesty` (Speagle 2020) nested sampling package is used with 500 live points and a stopping criterion of $dlog(\mathcal{Z}) = 0.5$. The multi-ellipsoid bounding method (`bound='multi'`) and the random walk sampling strategy (`sample='rwalk'`) were employed. Sampling was run in static mode (i.e., `dynamic=False`) using four parallel threads. We used a sample size of 100,000. As mentioned in Section 2.1.1, the Fitzpatrick extinction law and the SFD dustmap were used (Fitzpatrick 1999; Schlafly & Finkbeiner 2011). All results shown were generated using

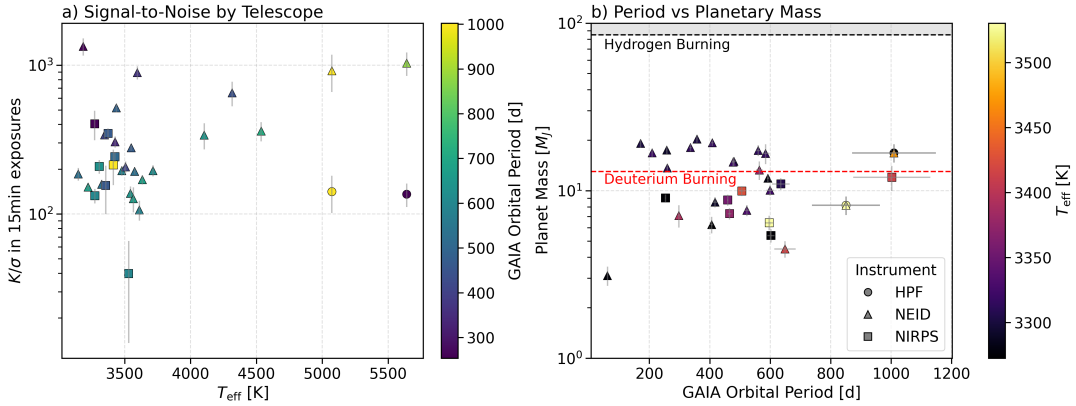


FIG. 3.5 – Two panel figure with on the left (panel a), the expected signal-to-noise ratio of the proposed targets as a function of the effective temperature, the color-bar indicates the orbital period of the companion as found by Gaia. The signal-to-noise ratio is represented in log-scale. In the right plot (panel b) we see a period-mass diagram of the proposed objects, with the color coding indicating the effective temperature. Two lines are annotated within this plot, which are the deuterium burning limit at 13 Jupiter masses and the hydrogen burning limit (sub-stellar/stellar boundary) at around 85 Jupiter masses. On both plots, the errors are shown in gray and the instruments are shown using the marker-scheme found in the legend. It is important to note that objects that are followed up with multiple instruments are shown twice in the plots.

the averaging method, unless stated otherwise.

In total, four runs on the original ASOI list have been performed, differing slightly in methodology. After every run, we reviewed the results and changed settings according to noteworthy behavior. Following the initial run, it became apparent that the fitting procedure sometimes favored solutions for which the interstellar extinction deviated significantly from zero, which we can see in Figure 3.6. Some solutions also show significant uncertainties in their proposed best-fitting parameters. Given that the majority of the targets are nearby, we expected these values to be close to zero. As a result, for all future runs, it was decided that this parameter would be permanently fixed to zero. During the analysis of the second run, an issue with the photometric data retrieval was identified. The `astroARIADNE` library queries the photometric catalogs for a given target using successively smaller radii, storing and using the smallest non-empty query. For stars that are, for example, part of dense clusters, this method introduced contamination from nearby stars (see the bottom-left panel of Figure 3.9 for an example). We performed a third run using the same method but with additional smaller radii. Even though this decontaminated the data, it decreased the data quality for uncontaminated targets, as this sometimes led to the unnecessary exclusion of data. Lastly, since most of these targets are M-dwarfs (single stars, or spectroscopic binaries), and thus are bright in the infrared, we opted to fit the targets using infrared data only. In Table A.2 the filters considered for this final run can be found together with the other filters `astroARIADNE` uses.

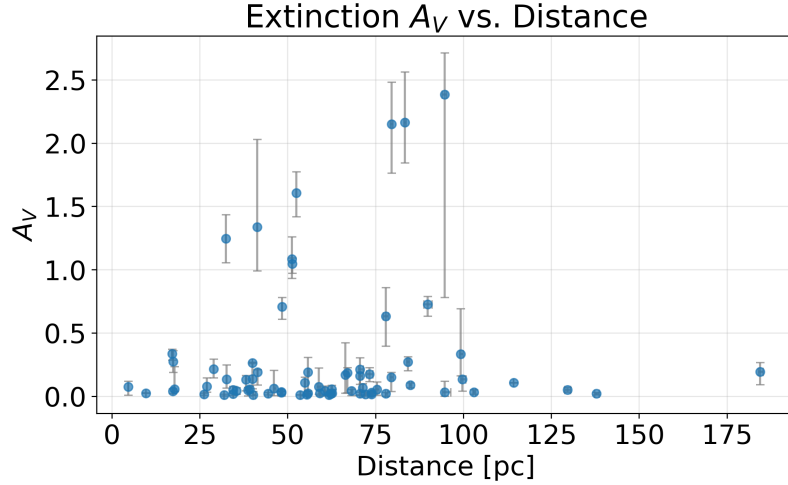


FIG. 3.6 – Scatterplot of the fitted distance (Parsec) against the interstellar optical extinction. The data shown are gathered from the test run (the first run), with in gray, the error on the fitted optical extinction.

The results presented in this work are mainly based on the second run, because it provided the best overall data quality. We manually verified all targets using SIMBAD to identify any unseen contamination from nearby sources, and for these targets the results from the third run replaced those from the second run. We compared the second run with the final IR-only run and with literature data for these stars, if available. The literature data used was extracted from ExoFOP ([NASA Exoplanet Science Institute \(NExSci\) 2022](#)). The results will be accompanied with an indication, to clarify from which run the data originates ('Run 1', 'Run 2', 'Run 3', 'IR-data only' and 'Literature'), if omitted, the second run was used (note that we replaced the contaminated targets).

Fitted parameters

In Figure 3.7, we see the literature parameter values plotted against the fitted parameter values we obtained using `astroARIADNE`. Orange representing confirmed binary systems, blue representing confirmed exoplanets and gray representing systems of an unknown nature. As expected, `astroARIADNE` performs very well in determining the distance of the system (lower left). It uses a very high-precision prior and the SED is minimally affected by the distance. If we did not assume an interstellar optical extinction of zero, these effects would be negligible due to the expected deviation in fitted distance. In the upper right plot, we see the stellar effective temperature comparison, and again it neatly follows the line, with some exceptions at lower effective temperatures. The same holds true for the radius plot (upper middle). In the lower middle plot we see the metallicity. Due to the limited amount of data

available, there are not a lot of objects shown, and in combination with the large errors on the fitted parameters a statistical significant conclusion cannot be made. In the lower right panel we see the Isochrone interpolated-mass, which closely follows the 1:1 line, with some outliers near the bottom and the top. We chose to show this version of the calculated mass, instead of the ‘gravitational mass’ `astroARIADNE` also provides, as the latter is directly calculated from the surface gravity, which is shown right above. The literature and the fitted parameter values do not align at all, with significant error-bars, which sometimes exceed a order of magnitude. A keen eye may have spotted a trend within the coloring, for example in the lower right mass plot. In this plot, most orange objects (confirmed binaries) are found at lower masses, which is explained by both a tendency towards multiplicity for low-mass stars (instead of the alternative — a high mass exoplanet) and our tendency to prioritize these targets in follow-up surveys. Another important note is that the literature values also assume a single object. It is therefore interesting to see that for most parameters `astroARIADNE` performs reasonably well, with an exception for the stellar surface gravity and possibly for the metallicity.

To highlight the precision `astroARIADNE` usually performs at, given standard single targets we refer to Figures 6-10 from [Vines & Jenkins \(2022\)](#) and to Figure 3.8, where we take a closer look at the posterior distributions compared to the work done by [Stefánsson et al. \(2025\)](#). As shown in Figure 3.8, the fitted parameters are in agreement with earlier work. It is important to note that [Stefánsson et al. \(2025\)](#) found an interstellar optical extinction of $A_v = 0.019_{-0.013}^{+0.016}$ and $A_v = 0.150_{-0.097}^{+0.15}$ for Gaia-4 and 5 respectively while we manually set this parameter to zero.

In Figure 3.9 we see a collection of four SEDs. The top two are the SEDs of Gaia-4 and 5. At first glance, the residuals seem to indicate the model does not fit the data well. The difference between the model and the data points are a handful of times in the order of several standard deviations. But on closer inspection, we see that this is to be expected in these cases. The residuals represent the distance (expressed in standard deviations) from the measured fluxes to the synthetic fluxes of the used model. Discrepancies between models can cause a trickle down effect to the residual plots and can be mitigated by using the ‘sampling method’. In this case, the noise terms are likely to be in disagreement across the different models. The SED should thus be interpreted with this context in mind. The bottom-right panel (Gaia ID 5085864568417061120) is confirmed to be a spectroscopic binary. There seems to be excess flux at longer (infrared) wavelengths. Which could be explained by the secondary star. It could imply that this excess (infra)red light is due to an unseen companion that is bright in the infrared. But when taking into account other confirmed binary systems, that do not show the same behavior, this reasoning becomes questionable. In addition, when taking into account the context within the residuals are calculated this statement cannot be supported and is most likely due to model disagreements. In Figure 3.10 a similar four panel plot is shown, with Gaia-4 and Gaia-5 again on top but with other noteworthy targets on the

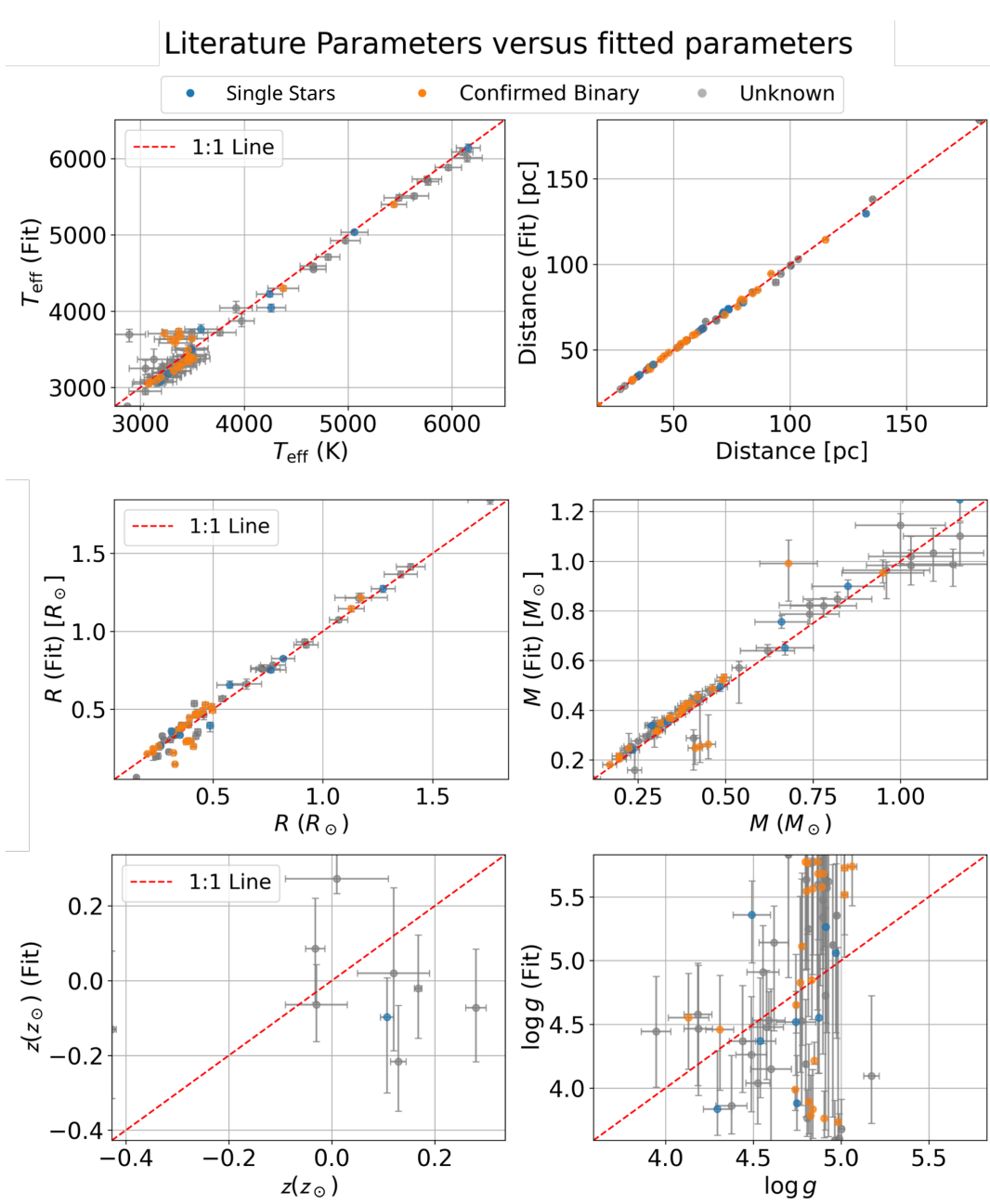


FIG. 3.7 – A six-panel Figure comprising of scatter plots, in which literature values queried from ExoFOP ([NASA Exoplanet Science Institute \(NExScI\) 2022](#)) are plotted against fitted values from the second run. In these six plots, the effective temperature (top-left), the distance (top-right), the radius (middle-left), the Isochrone interpolated stellar mass (middle-right), the metallicity (lower left) and stellar surface gravity (lower-right) are shown in their standard units ($K, \text{Parsec}, R_{\odot}, M_{\odot}, z_{\odot}, \text{cgs}$) and with both their literature error and fitted error (indicated by the gray horizontal and vertical bars). With blue indicating unknown systems and orange systems with confirmed multiplicity. The dotted red lines indicates the 1:1 line. The amount of data points shown is solely depended on if the data was available.

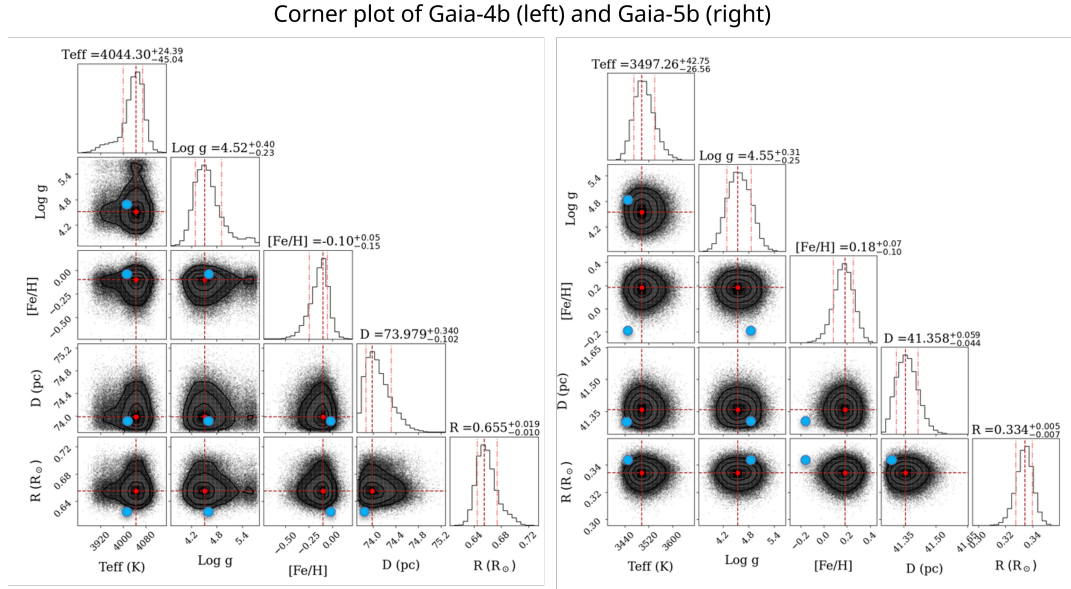


FIG. 3.8 – Corner plot of posterior parameter distributions (Second run) of Gaia-4b (left) and Gaia-5b (right) with the blue dots representing the literature values found by [Stefánsson et al. \(2025\)](#).

bottom. The plots show the posterior distributions of the stellar radius. In the case of Gaia-5, the different models agree and converge close to the literature value. The BT-family of models are favored over the phoenix model. In the case of Gaia-4, there seems to be a small divide, with the Kurucz model favoring a slightly larger radius compared to the BT-settl and CK04. The phoenix model bridges in between. The BT-SETTL model however, is heavily favored. The Kurucz model is around 4 times less likely than the BT-SETTL model. This is a perfect example of a situation where the assumed microphysics are impacting the results in a significant way, BMA eases this discrepancy by averaging these results based on the model likelihoods in a weighted manner. In the bottom two figures, we again see two confirmed spectroscopic binaries. Similar to Gaia-4 and 5, the models in the left fit do not agree while the models on the right side do. It is immediately noticeable that the models themselves do not converge on a single solution. The PDF’s are intricate and extremely multi-modal. Nested sampling, as mentioned by Section 2, is particularly good at finding these multi-modal posterior distributions. An argument for multiplicity can be made based on these extreme types of distributions. The confirmed planets do not show this behavior and we would expect a spectroscopic binary, with a given mass and flux-ratios to produce different SEDs that sum to the measured SED. The secondary (the less massive star) will be relatively brighter as we shift our focus at longer wavelengths. This would cause excess reddening, impacting the fitting procedure. But this behavior is more easily explained by looking at the model probabilities and the context of the fitting algorithm.

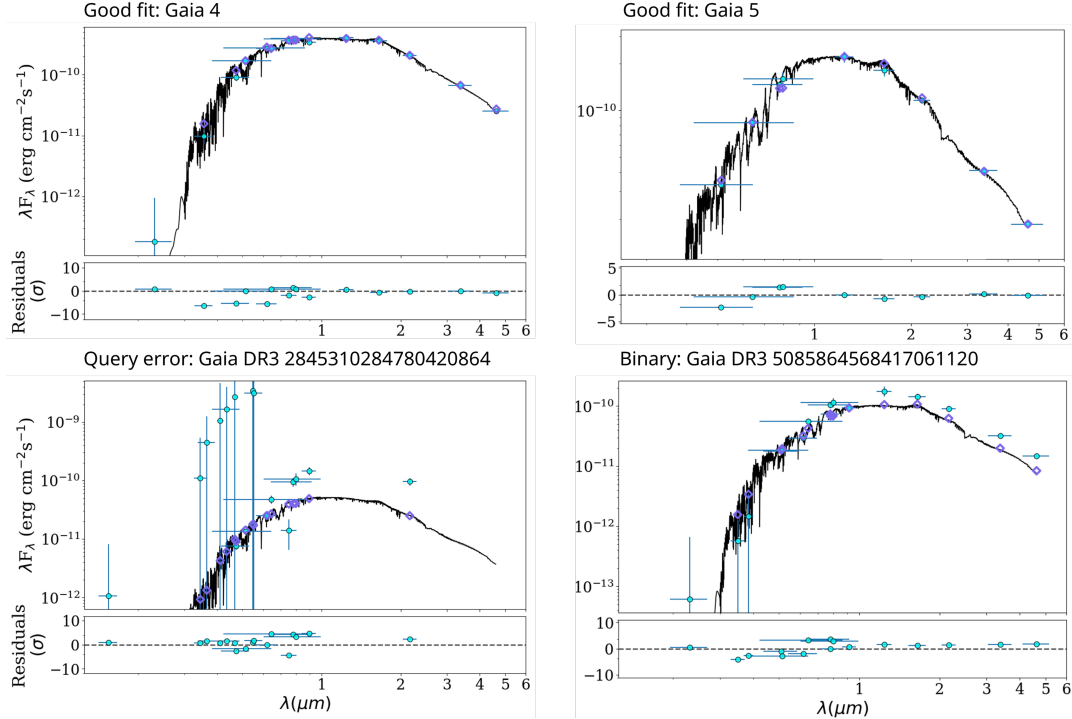


FIG. 3.9 – Four panel figure representing the best-fitting SED models for Gaia-4 (left-top), Gaia-5 (right-top). Gaia DR3 2845310284780420864 (bottom-left) and Gaia DR3 5085864568417061120 (bottom-right). Every SED is accompanied with a residual plot. The x-axis represents the wavelength (in micron) and is plotted against the energy flux density (in $\text{erg} \cdot \text{cm}^{-2} \cdot \text{s}^{-1}$) in log-scale. The SED model shown (black lines) are the most likely model found. The best-fitting parameters used as input for the models were the parameters found using BMA, not the best-fitting parameters for the model shown. The blue dots represent the fluxes used for the fitting procedure, the error-bars on the x-axis show the width of the filter. The error-bars on the y-axis show the error on the measurement. The purple triangles show the synthetic fluxes. The residual plot underneath each model is calculated using the distance between the blue data points and the purple triangles expressed in standard deviations (using the error on the flux measurement). Gaia-4 and Gaia-5 are prime examples of the usage of the `astroARIADNE` software. Gaia DR3 2845310284780420864 (bottom left) is an example of a query within a densely populated field and where the photometric retrieval was ineffective. Lastly, Gaia DR3 5085864568417061120 is an example of a confirmed spectroscopic binary.

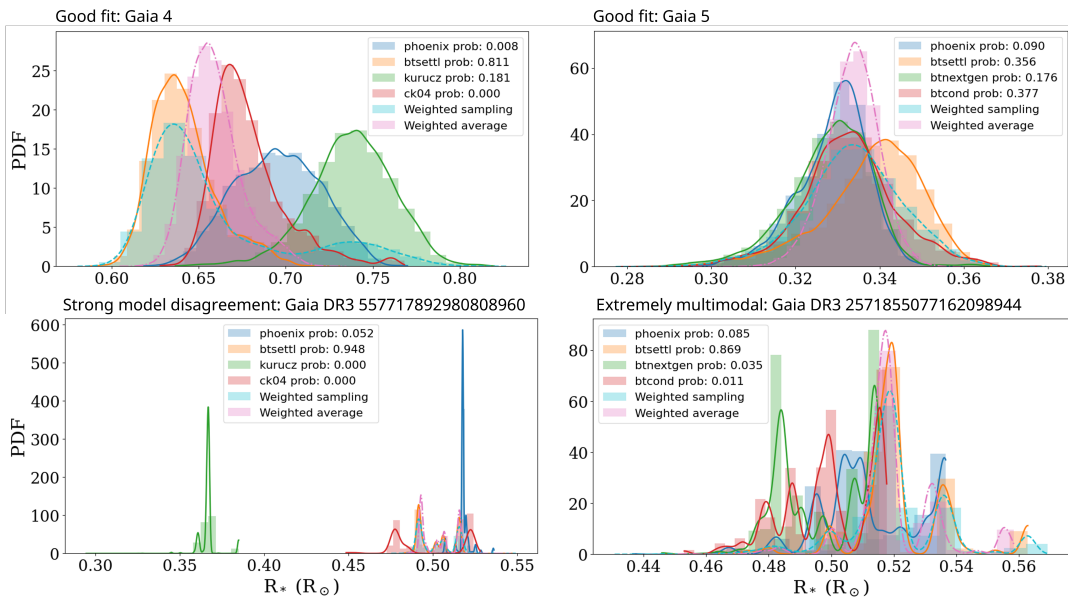


FIG. 3.10 – Four panel figure with PDF’s of the stellar radius (in R_\odot). The objects shown are Gaia-4 (top-left), Gaia (top-right), Gaia DR3 557717892980808960 (bottom-left) and Gaia DR3 2571855077162098944 (bottom-right). The color differentiates the PDF’s per model (or mix of models). The PDF’s are calculated with a kernel density estimation performed on the histograms that are plotted underneath the PDF’s. The histograms each have ten bins. The legends for each PDF also contains the model likelihood, which is shortened to ’model prob:’.

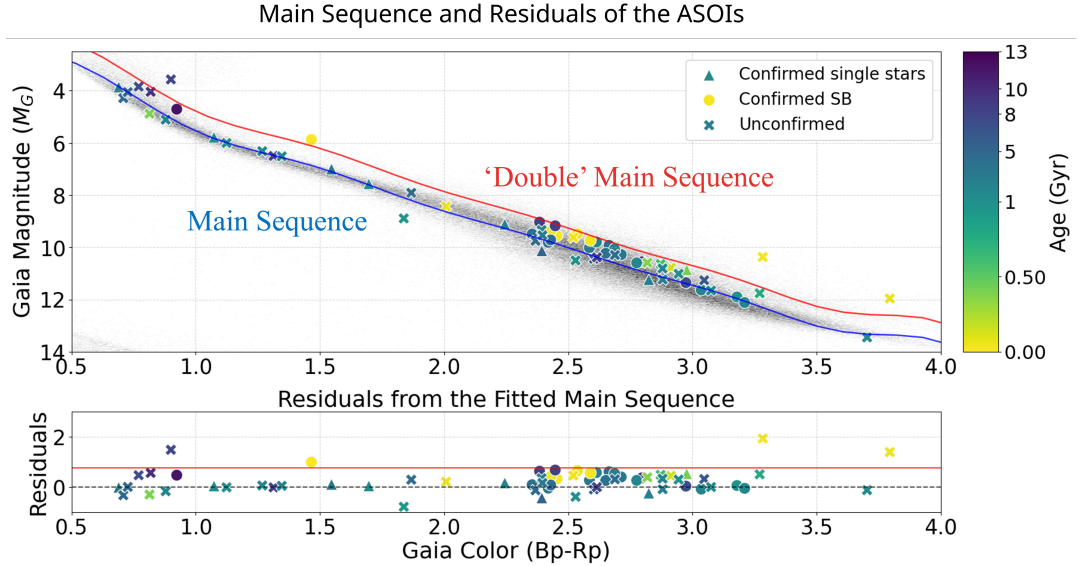


FIG. 3.11 – CMD with the Gaia $Bp - Rp$ color on the x-axis and the Gaia absolute magnitude (M_G) on the y-axis. The blue line is generated by interpolating the stellar parameters Table (Pecaut & Mamajek 2013). The red line is calculated by subtracting $2.5 \log_{10}(2)$ from the blue line, effectively doubling the luminosity of the star. It outlines a rough estimate of the CMD position of two MS stars with equal luminosities ($\epsilon = 1$). The age of the system, as fitted by `astroARIADNE` is shown (in giga-years) by the coloring. Underneath the CMD, the residuals are shown (in absolute magnitude) and follows the same coloring scheme as the CMD. The markers indicate the current status of the object.

When solely looking at infrared data, the fits become significantly less precise (see Table 3.1), this is to be expected since there is less data available to make the fit. Besides that, some fitted targets show significant deviations between fits. This is most prominently seen in the surface gravity and the effective temperature (Gaia DR3 4188996885011268608 and Gaia DR3 2104920835634141696). We manually compared the IR-only parameters and the parameters from the first run to the literature values and we found that besides being more precise, they also tended to align better with the literature values.

TABLE 3.1 A comparison of IR-derived and regular fitted stellar parameters. They tend to agree, with an exception for the surface gravity and the temperature. The IR-derived values also tend to have larger uncertainties.

Gaia DR3 Source ID	IR Fit				Original Fit			
	$M (M_{\odot})$	$R (R_{\odot})$	$T_{\text{eff}} (\text{K})$	$\log g (\text{cgs})$	$M (M_{\odot})$	$R (R_{\odot})$	$T_{\text{eff}} (\text{K})$	$\log g (\text{cgs})$
4062446910648807168	$0.79^{+0.04}_{-0.06}$	$0.75^{+0.03}_{-0.03}$	4766^{+319}_{-215}	$4.49^{+0.49}_{-0.46}$	$0.82^{+0.03}_{-0.05}$	$0.75^{+0.02}_{-0.01}$	4820^{+109}_{-69}	$4.92^{+0.36}_{-0.74}$
4188996885011268608	$0.18^{+0.01}_{-0.01}$	$0.15^{+0.01}_{-0.01}$	3869^{+181}_{-132}	$4.47^{+0.57}_{-0.49}$	$0.19^{+0.00}_{-0.00}$	$0.23^{+0.01}_{-0.01}$	2933^{+55}_{-48}	$5.31^{+0.52}_{-0.47}$
373892712892466048	$0.47^{+0.02}_{-0.02}$	$0.40^{+0.02}_{-0.02}$	3860^{+145}_{-105}	$4.33^{+0.44}_{-0.44}$	$0.49^{+0.01}_{-0.01}$	$0.53^{+0.03}_{-0.03}$	3336^{+56}_{-52}	$4.67^{+0.78}_{-0.52}$
834357565445682944	$0.39^{+0.02}_{-0.02}$	$0.33^{+0.02}_{-0.02}$	3859^{+105}_{-109}	$4.65^{+0.39}_{-0.45}$	$0.38^{+0.00}_{-0.01}$	$0.26^{+0.00}_{-0.00}$	3651^{+11}_{-11}	$4.61^{+0.39}_{-0.04}$
2104920835634141696	$0.17^{+0.01}_{-0.01}$	$0.14^{+0.01}_{-0.01}$	3856^{+140}_{-111}	$4.06^{+0.41}_{-0.28}$	$0.18^{+0.00}_{-0.01}$	$0.22^{+0.01}_{-0.01}$	3042^{+40}_{-35}	$5.56^{+0.39}_{-0.45}$
2824801747222539648	$0.39^{+0.03}_{-0.02}$	$0.33^{+0.02}_{-0.03}$	3972^{+206}_{-119}	$5.16^{+0.42}_{-0.57}$	$0.42^{+0.02}_{-0.02}$	$0.42^{+0.01}_{-0.01}$	3476^{+53}_{-32}	$5.34^{+0.58}_{-0.61}$

Correlation Tests

To find a correlation between possible bad fits and multiplicity we performed a Pearson-r correlation test using the most recent object status as a binary value (which means we performed a Point-Biserial test). With 0 representing objects with a single line profile and 1 representing objects with a double lined profile. This test was performed on the literature parameters, the `astroARIADNE` derived parameters, their differences expressed in standard deviations (using the literature error) and lastly the deviation from the Main-Sequence (in magnitudes) For a full overview of the tested parameters, we refer to Table A.3, found in the Appendix. We acknowledge that this method is prone to error, since the single lined profiles are technically not confirmed to be exoplanets yet (for which we need measurements near or at the maximum/minimum amplitude of the RV-curve). Therefore, our dataset representing single lined objects is possibly contaminated with some binary systems. We preferred this over the alternative, which would be removing all but three systems (Gaia-3A, Gaia-4 and Gaia-5). This would severely impact the significance of any correlation found. Ambiguous broadening functions (e.g., the gray broadening function in the middle panel of Figure 2.2)) were assigned fractional numbers. Even though they are not confirmed to be binary systems nor fully ruled out (as wider BF can be the result of uncertainties in the deconvolution process), we omitted these systems in the analysis. Targets that are yet to be followed up are also not considered for this analysis. In Table A.1, found in the Appendix, we can see how each target was labeled. In Figure 3.12 we see the correlation coefficient (r) scattered against the p-value (in log-scale)

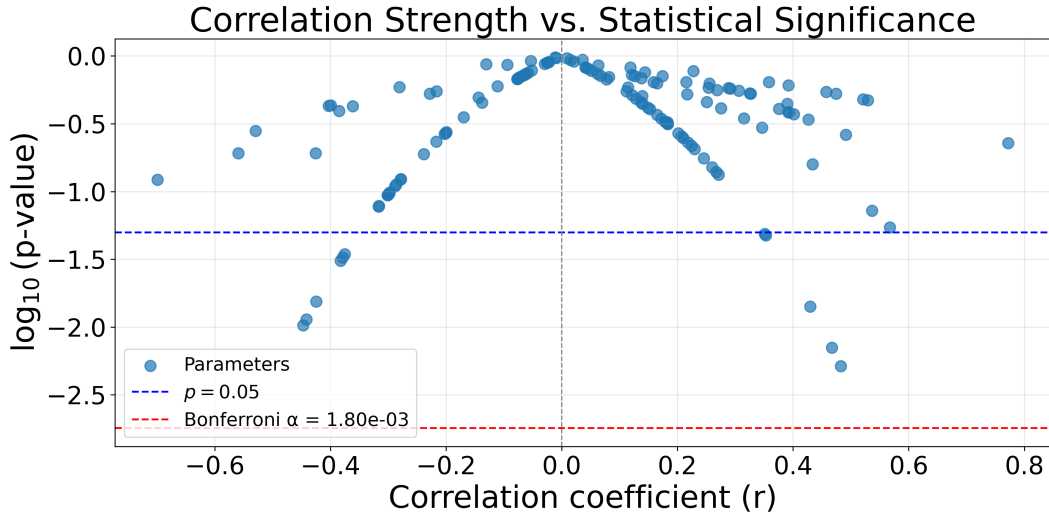


FIG. 3.12 – Scatterplot of each tested metric, with on the x-axis the Correlation coefficient (r) and on the y-scale the p-value in log-scale. The blue line represents a p value of 0.05 and the red line the Bonferroni correction performed. As we can see, no metric exceeds the Bonferroni correction but multiple metrics exceed the standard significance level of $p = 0.05$. A full description of the metrics tested and their corresponding p- and r- value can be found in Table A.3.

for each tested column. Since multiple null-hypotheses were tested, we performed a Bonferroni correction. This correction will be discussed further in the Section 4.1.

Chapter 4

Discussion

Throughout the course of this thesis, the research team was granted the requested telescope time to observe the selected targets. The final observation proposals included similar images to those shown in Figure 3.5. The key differences were the inclusion and removal of some objects and instrument specific plots for their respective proposals instead on one singular figure using a marker-scheme. The supplementary targets are not discussed in this work as they are outside its scope. The observations will continue after the submission of this thesis.

4.1 SED Fitting

The stellar parameters retrieved through the fitting procedure — for the candidates that are confirmed to be exoplanet hosting systems, and not spectroscopic binaries — can be considered to be reliable. As briefly discussed in Section 3, the fitted parameters for Gaia-4 and 5 are in agreement with [Stefánsson et al. \(2025\)](#). [Sozzetti, A. et al. \(2023\)](#) found the stellar parameters of Gaia-3 Ab. A part of the astrometric solution has been withdrawn [\[ESA\] \(2024\)](#), but most of the stellar parameters were found using SED fitting using a different software, namely EXOFASTv2 ([Eastman et al. 2019](#)). These parameters can be viewed in Table 4.1 together with the parameters retrieved in this work. The surface gravity immediately stands out, as the values differ by a order of magnitude. The EXOFASTv2 software uses a different method than the software we adopted. It has the ability to fit the parameters using the BT-NextGen model or using a 'MIST bolometric correction grid' ([Dotter 2016](#)). It is unclear which method [Sozzetti, A. et al. \(2023\)](#) adopted. In case the BT-NextGen method was adopted, we can compare this to our own fit which can be seen in Figure 4.1. The BT-NextGen model is not shown, because this model is identical to the BT-Settl model as previously mentioned in Section 2.1.1. We see that `astroARIADNE` prefers the Phoenix atmospheric model over the BT-settl model, which do not agree

TABLE 4.1 Table containing the literature values for Gaia-3A ([Sozzetti, A. et al. 2023](#)) and our fitted stellar parameters. They seem to be in agreement, with an exception for the stellar surface gravity.

Parameter	Literature	SED fitting (This work)
Identifiers		
Gaia DR3 Source ID	1712614124767394816	–
HIP ID	66074	–
Stellar Parameters		
T_{eff} (K)	4300 ± 60	4224 ± 38
$\log g$ (cgs)	4.58 ± 0.05	$5.36^{+0.27}_{-0.38}$
[Fe/H]	0.12 ± 0.05	$-0.14^{+0.22}_{-0.21}$
$R_{\star} (R_{\odot})$	$0.69^{+0.013}_{-0.012}$	0.75 ± 0.01
$M_{\star} (M_{\odot})$	$0.705^{+0.025}_{-0.023}$	0.76 ± 0.03
Distance (pc)	$35.37^{+0.03}_{-0.02}$	$35.41^{+0.04}_{-0.03}$

with each other. This could partially explain the difference between derived values. But upon closer inspection, we see that the BT-Settl model on its own also does not agree with the value derived by [Sozzetti, A. et al. \(2023\)](#). Which could be due to differences in sampling methods used (MCMC and nested sampling) or due to the usage of the MIST grid. The performance of the MIST grid, as noted by [Eastman et al. \(2019\)](#), has not been well studied. Other stellar parameters also do not agree well, which could be due to the adaptation of the YY isochrones ([Yi et al. 2001](#)) by [Sozzetti, A. et al. \(2023\)](#), besides the aforementioned reasons.

Currently, there are eight other candidates for which we have obtained partial follow-up data and do not show signs of multiplicity. These can be found in Table [A.1](#) in the appendix.

`astroARIADNE` cannot be used as a diagnostic tool to aid the search for multiplicity, the correlations found, between multiplicity and the SEDs are not statistically significant or show correlations that are most likely features of our target parameter space. In Figure [3.12](#), multiple metrics are shown lower than the $p = 0.05$ threshold but these results need to be critically evaluated. We are currently testing a set of hypotheses (139 to be exact.) When performing on a set of hypothesis, the chance to get a significant p value while no underlying correlation is found needs to be taken into account. The Bonferroni correction (seen in red) rescales the boundary at which we call a result significant and is defined as $\alpha = p/N$ where p is significance threshold for a single hypothesis and N the number of hypothesis. However, the usage of this method is not mathematically justified, as numerous metrics are directly correlated to other tested metrics. This explicitly breaks the assumption of independence needed to use this correction, otherwise, it would be overly conservative. To counteract this effect, we approximate the number of independent tests to be one-fifth of the total, and apply the Bonferroni correction accordingly. No metric was found to be statistically relevant using this correction. However, we performed this test only as

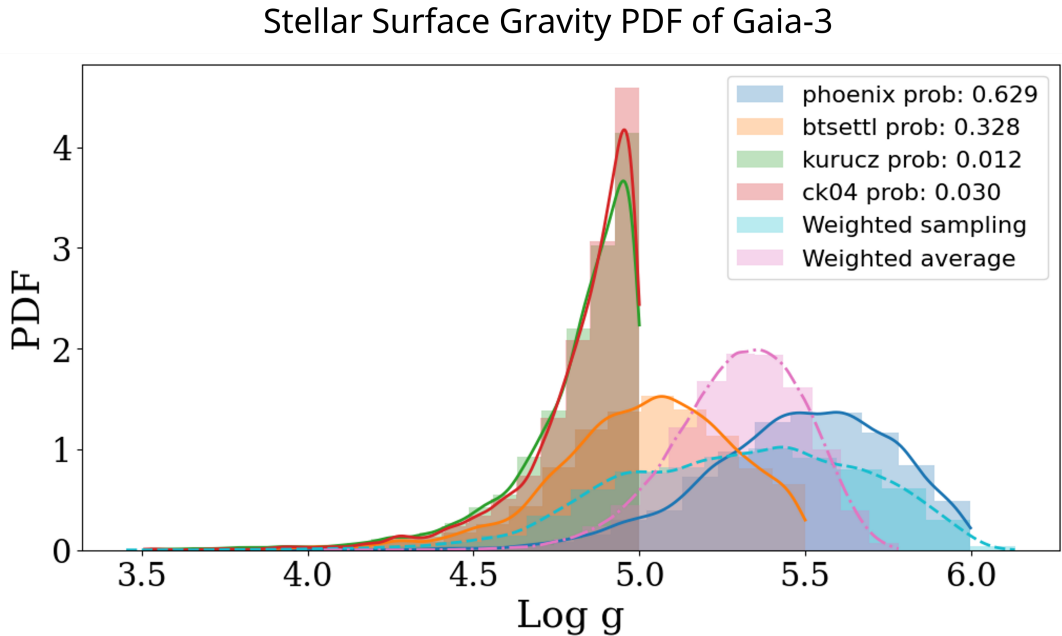


FIG. 4.1 – PDF of the surface gravity (cgs) as found by `astroARIADNE` for Gaia-3A. The models do not seem to agree on a solution.

a control measure and not as a strict statistical requirement. We did analyze every single metric that had a p value lower than 0.05 and most of these are directly related to the stellar mass (M_{star} , T_{eff} , $\log g$, M_G) and the error on these measurements. In Figure 4.2, we see two histograms of example metrics — the effective temperature and the stellar mass (in Kelvin and Solar mass respectively). Note that the distributions are qualitatively similar, as they are inherently correlated. It is also evident that the confirmed binaries (shown in blue) tend to occupy lower values compared to the single-star systems (shown in orange). This can directly be explained by the parameter space we are probing with these targets. Theoretically, we do not expect there to be high mass exoplanet companions to low mass stars, so signal posing as these objects are more likely to be false positives. This obvious statement however does not give us any insightful diagnostic tool for the detection of false positives — we are after all most interested in this parameter space.

There are two other terms that are of interest: The TESS noise ϵ_{TESS} and the distance from the main sequence.

In the upper panel of Figure 4.3, we see a histogram of the TESS noise metric. Higher terms seem to be exclusive to binary systems (in blue). As described in Section 2, the noise errors are introduced to account for non-instrumental additional noise, such as stellar variability. Multiplicity could induce an excess in these noise terms, which is what we partially expected. However, TESS does not measure absolute magnitudes,

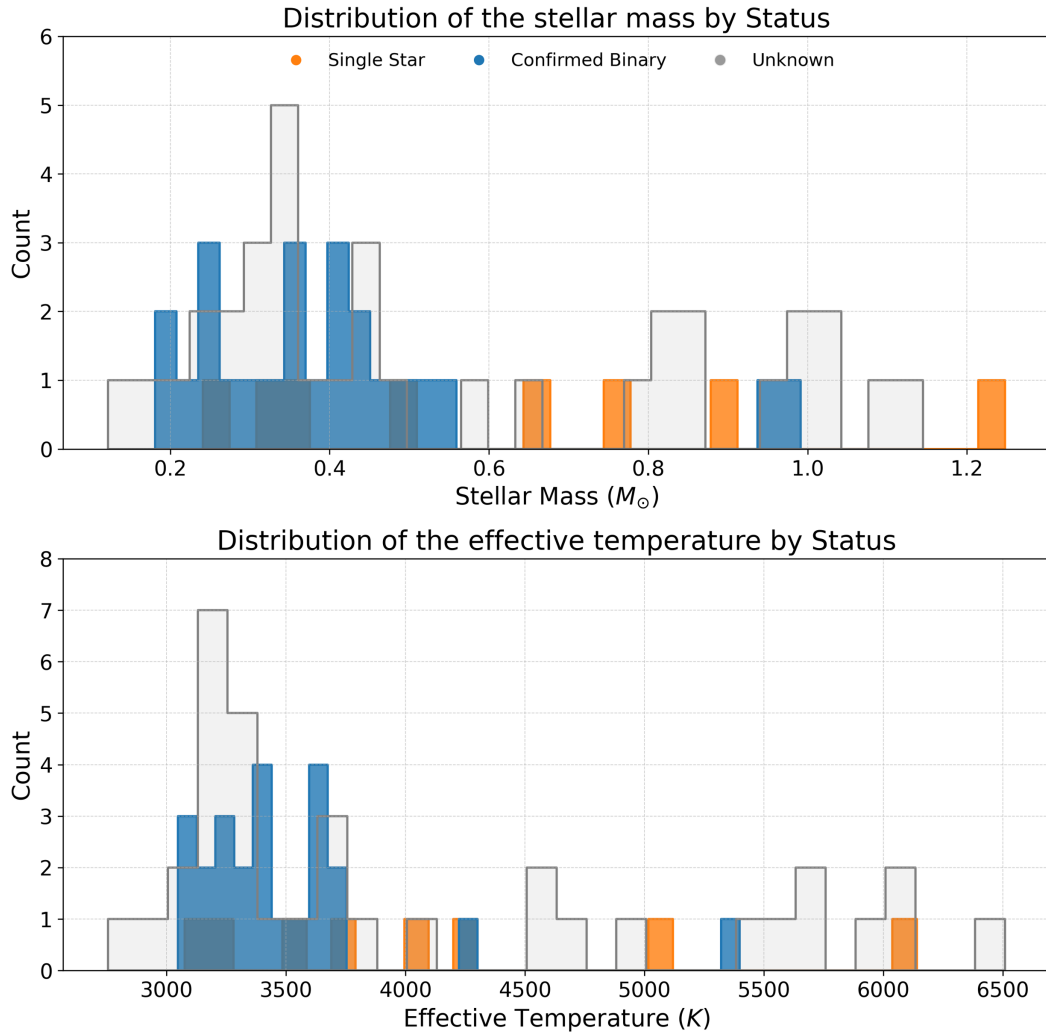


FIG. 4.2 – Histograms of both the effective temperature (upper histogram in Kelvin) and the stellar mass (lower histogram in M_{\odot}). Both values are derived using `astroARIADNE`. Multiplicity is highlighted by the color-scheme, with Orange indicating single stars and blue confirmed binary systems. Gray highlights the ASOIs that are yet to be determined. The y-axis of both plots indicate the counts.

only relative ones. TESS infers the magnitude using other databases. This correlation could also be explained by some unforeseen consequence of the TESS data pipeline, and thus should be considered with caution ([Ricker et al. 2014](#)).

Lastly, the deviation from the main sequence does seem to be an indicator of multiplicity. In the aforementioned figure (4.3), we see the histogram plot of the MS residuals in the lower panel and as expected, over-luminosity seems to be an indicator for multiplicity. It is important to note that the sole white dwarf (seen in the lower left corner of Figure 1.10) has yet to be followed up. Thus, it was omitted from the correlation test. It was also removed from the histogram since it was clearly not a MS star. We reinstate that the sample size is extremely small, and that the resulting correlations need to be interpreted as such.

We found no significant correlation between the remaining metrics. One possible explanation could be the addition of the noise term in the SED fitting process, which may partially mask the variability multiplicity introduces. One would then expect these noise terms to be correlated with multiplicity, but this is not necessarily true. Correlations across filters could still underlie the dataset, and would not be found using the statistical analysis performed. In addition, the flux ratio of binary systems is inherently wavelength-dependent. This means that any correlation between metrics could be diluted by our sample size of false positives. The inability to determine the stellar parameters for these systems with photometry alone (such as mass), further limits our sensitivity to such correlations. The sample size greatly impacts the statistical relevance of this study, making it unlikely that any but the strongest of trends are detected. A future study could address this by inserting mock data or using the fourth Gaia data release (DR4) to improve upon this issue.

The parameters listed in ExoFOP are also derived under the assumption of no multiplicity, and thus are untrustworthy in most cases. There seems to be no disagreement between these parameters and the ones we retrieved through SED fitting, with an exception to the stellar surface gravity, throughout both single and double stars. The discrepancy in the surface gravity, trickles down to the masses of the objects. The masses that are derived through the surface gravity are often not in agreement with the literature data. The isochrone-interpolated masses often give a more accurate description of the masses as seen in Figure 3.7. $\log g$ is also systematically more constrained in the literature compared to the values derived by `astroARIADNE`. This is likely due to the nature of the effects of the surface gravity on the SED. The surface gravity affects the features in the SED, causing deeper spectral lines. It also has an effect on the overall shape of the SED but only indirectly through the mass, which affects the temperature. It is however important to note that [Vines & Jenkins \(2022\)](#) did not find the same discrepancy. A comparison between literature data and fitted values for the metallicity z cannot be performed due to the scarce literary data. The data does suggest a similar discrepancy similar to the stellar gravity, and could be explained by similar reasoning. Again, [Vines & Jenkins \(2022\)](#) did not find a similar

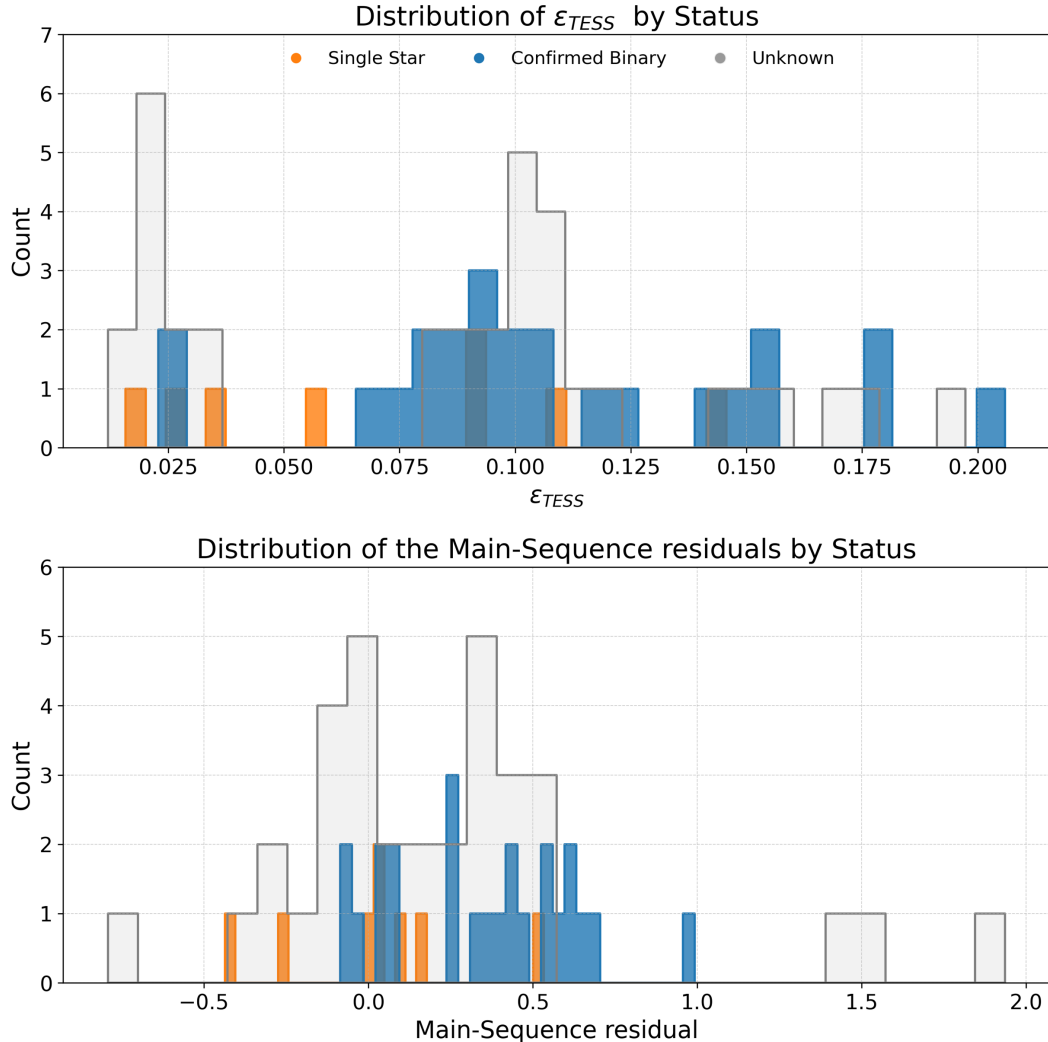


FIG. 4.3 – Two histograms of both the TESS noise metric (upper histogram) and the residual terms of the fitted MS (lower histogram in M_G). The y-axis of both plots indicate the counts. The same color-scheme is used as in Figure 4.2. The white dwarf target was removed in the analysis for the Main-Sequence residuals.

discrepancy. [Vines & Jenkins \(2022\)](#) do note that, for low-mass stars, the model differences become particularly notable. They claim this explains the disagreement between the fitted and the literature values. The internal structures of these stars, are expected to be wildly different than the structure of our own sun. Most of our knowledge on stellar structure is based on theoretical models and data gathered from our own star. Our dataset is comprised mostly of these stars.

The IR-only run was successful for five targets, four of whom are confirmed to be binary systems. As mentioned in the results, the companion is most likely to be relatively bright in the infrared. Even though a true statistical analysis cannot be performed, as we have no control group (the fifth is yet to be followed up). The fits agree well with the main run. This also holds true for parameters not shown (such as the noise parameters), with the only difference being the size of the error bars.

The fourth data Gaia data release will describe these type of systems in more detail using spectroscopic data gathered over time. Classifying exoplanets and ruling out false positive binary systems. It will also reclassify single-star solutions as exoplanets or binary systems. Currently, there is a clear lack of non single-star solutions with orbital periods of around one year ([Stevenson et al. 2023](#)). This is caused by the fitting procedure, the parallax movement masks the reflex motion as they are both on a 1-year cycle. Using these new data, it would be interesting to re-perform this analysis, as it could give insight in the behavior of spectroscopic binaries in SED fitting software that use single-star models. Specifically in terms of mass ratio and its relationship with the flux ratio as a function of the filter used and the noise term associated with the filter. More importantly, it would be very interesting to perform population studies on these spectroscopic binaries and the sub-stellar systems they are mimicking. The differences in formation methods could trickle down into the orbital parameters, such as the eccentricity and obliquity. This could be combined with population studies on the brown dwarf desert. This parameter space has not been discussed in this work, but is related to the Jupiter Desert. It describes the lack of intermediate-mass brown dwarf companions to A-, F-, and K-Stars, and is theorized to be boundary between exoplanet gravitational instability and binary star formation processes ([Kouwenhoven et al. 2007](#); [Duchêne et al. 2022](#); [Stevenson et al. 2023](#)). Describing objects within and around these transition areas plays a key role in understanding the formation theories and their dependencies.

Even though `astroARIADNE` was used, there are other software available. Most noteworthy is VOSA ([Bayo et al. 2008](#)) which has the ability to fit binary stars. The spectroscopic binaries are explicitly mentioned by them, in the context that they are extremely difficult to fit for, as they tend to have similar SEDs. A new analysis could be performed with VOSA, but `astroARIADNE` is more advanced. The tradeoff between describing the single-star systems and finding a correlation between multiplicity and stellar parameters found through SED fitting needs to be evaluated in those cases.

4.1.1 Ongoing Observations

Most ASOIs have been identified as binary systems, with currently only two (three if you include Gaia 3-b or eight if you include all clearly single-lined spectra) exoplanet systems.

After obtaining RV measurements for Gaia DR3 3937630969071148032, the data was analyzed and a double lined spectrum was found. Using the RV data of both objects and code provided by the research team the orbital parameters were found and can be seen in Figure 4.6. The code uses a MCMC algorithm to fit for these parameters. We used these parameters to estimate the mass of the primary and secondary and they were found to be $M_1 \simeq 0.101M_{\odot}$ and $M_2 \simeq 0.087M_{\odot}$ respectively, which would make the very late M-dwarfs. This estimation was done by using the binary mass function, as described by Section 2. On the contrary, our single-star SED fit derived a mass of $0.40^{+0.02}_{-0.01}M_{\odot}$. We used the RV-derived masses to retrieved the luminosities of the primary and secondary. This was done using a polynomial interpolation of the Mamajek Table [Pecaut & Mamajek \(2013\)](#). These luminosities were then used to estimate the semi-major axis of the system. In Figure 4.5 we see the semi-major axis a_0 color-coded as a function of both the primary mass M_1 and the flux-ratio ϵ . The Blue line represents the semi major axis as derived using the aforementioned approximation. The red line indicates the Gaia DR3 value. The Black line, denoted with the label 'Theory' shows the flux-ratio as a function of the primary mass (using mass ratio $q = 0.86$). The discrepancy between the RV approximated values and the Gaia values is still an open question. In addition, when comparing the combined fluxes of the primary and secondary to the flux expected from a $0.40M_{\odot}$ star, a significant discrepancy is found. Comparing spectroscopic binaries to their single-star SED fit was unfortunately, due to time constraints, not performed in a more thorough manner.

Regarding the objects found by expanding the ASOI list, as described in Section 3, we have identified two brown dwarf candidates. In Figures 4.7 and 4.8 we see the expected RV curve and the broadening functions of Gaia DR3 3724701024704375424 and Gaia DR3 4580216762992082048, which are from now on referred to as Object 1 and Object 2 respectively.

The broadening functions clearly show a single-lined profile in both cases. Additional follow-up observations are still necessary to completely rule out multiplicity. The observations were not taken at the maximum RV amplitude, which is preferable in ruling out false-positives. The double-lined spectrum will be easiest to detect at such phases. Taken at face-value, however, it is a promising sign. Assuming a single-star system, we retrieve the stellar parameters by SED fitting and the orbital parameters using the Gaia astrometric solutions (as described by Section 3). The latter is done using a privatized code package developed by Dr. G.K. Stefansson, which is based on a Markov Chain Monte Carlo (MCMC) algorithm. The parameters of these systems

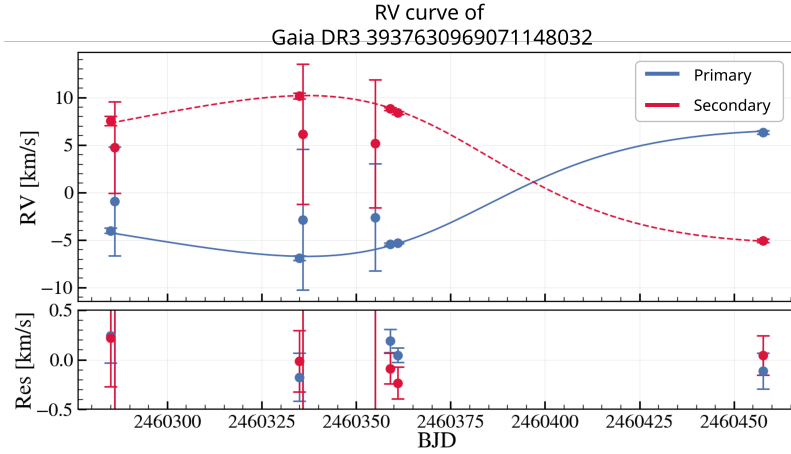


FIG. 4.4 – Two panel figure, with on top the RV measurements with a fitted curve of Gaia DR3 3937630969071148032. On the x-axis, we see the Barycentric Julian Date, and on the y-axis the RV in km/s . In the lower figure we see the residual terms. The Color-coding indicates the object, with blue representing the primary and red the secondary.

can be viewed in Table 4.2. Both objects are very late M-dwarfs with high-mass brown dwarf companions.

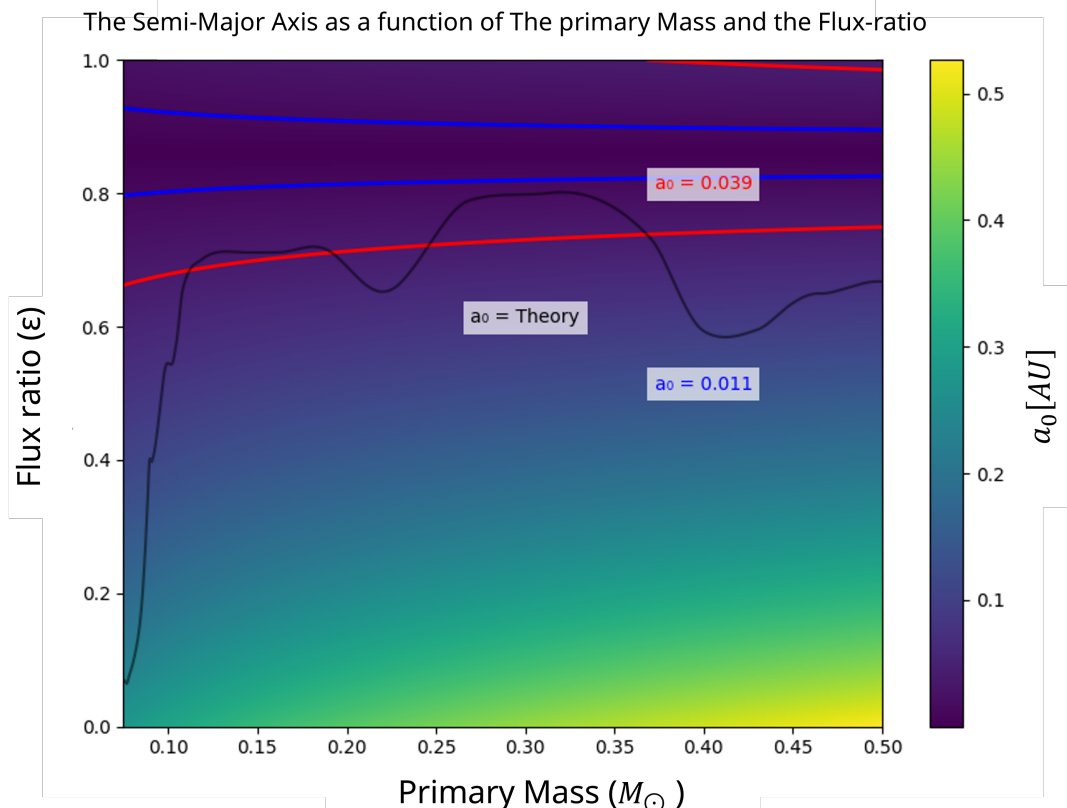


FIG. 4.5 – A plot of the semi-major axis a_0 color-coded as a function of both the primary mass M_1 and the flux-ratio ϵ using a period of 460 days and a mass ratio $q = 0.86$. The Blue line represents the semi major axis found by interpolating the Mamajek Table for the estimated masses to retrieve the flux-ratio. Then, using Equation 1.1 the semi-major axis is found . The red line indicates the Gaia DR3 value. The Black line, denoted with the label 'Theory' shows the flux-ratio as a function of the primary mass (using mass ratio $q = 0.86$).

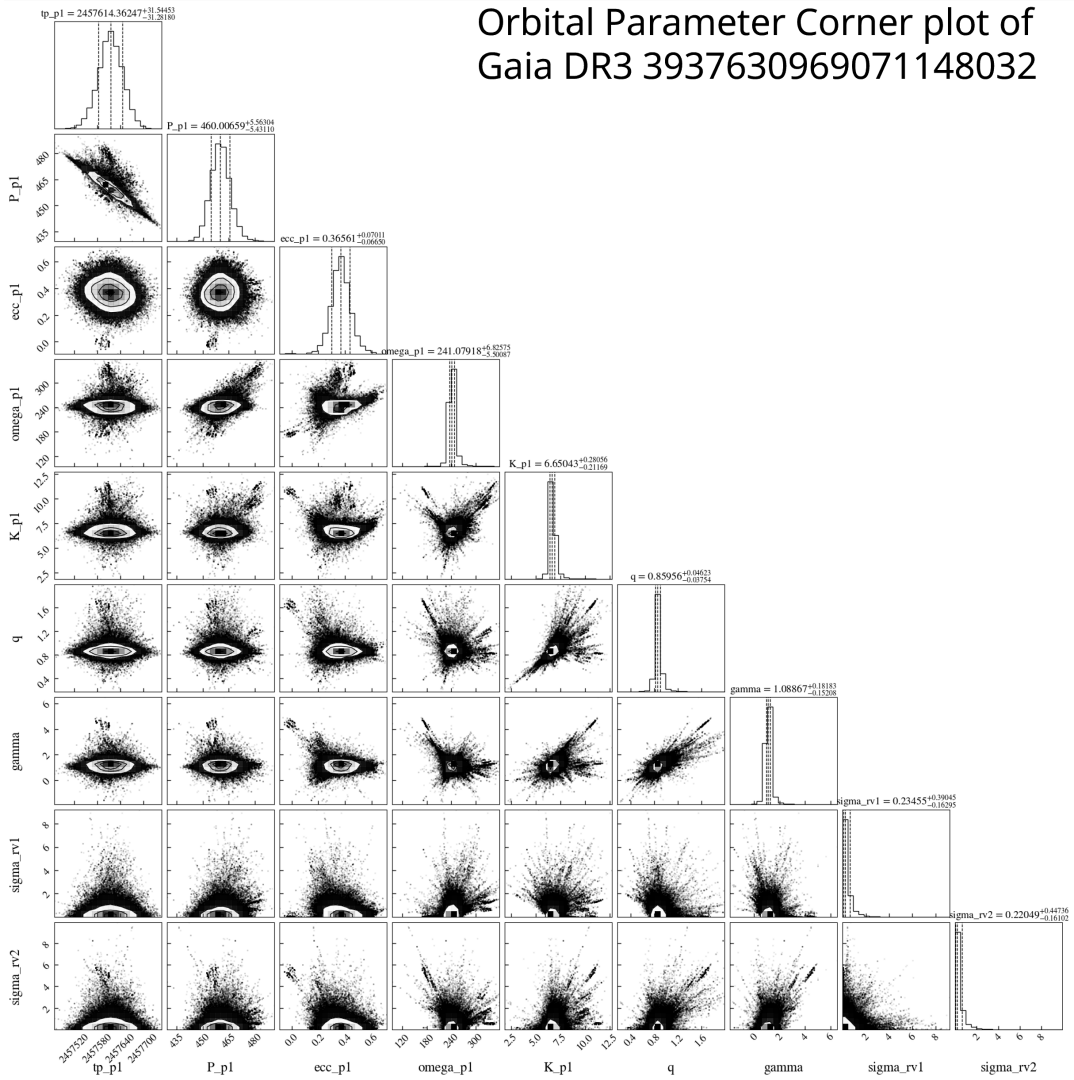


FIG. 4.6 – Corner plot of the derived orbital parameters of Gaia DR3 3937630969071148032, which is a spectroscopic binary. The system has mass ratio $q = 0.86^{+0.046}_{-0.038}$, eccentricity $e = 0.366^{+0.070}_{-0.066}$, period $P = 460.0^{+5.6}_{-5.4}$ and the primary has a RV amplitude of $K = 6.65^{+0.28}_{-0.21} \text{ km s}^{-1}$.

Gaia DR3 3724701024704375424

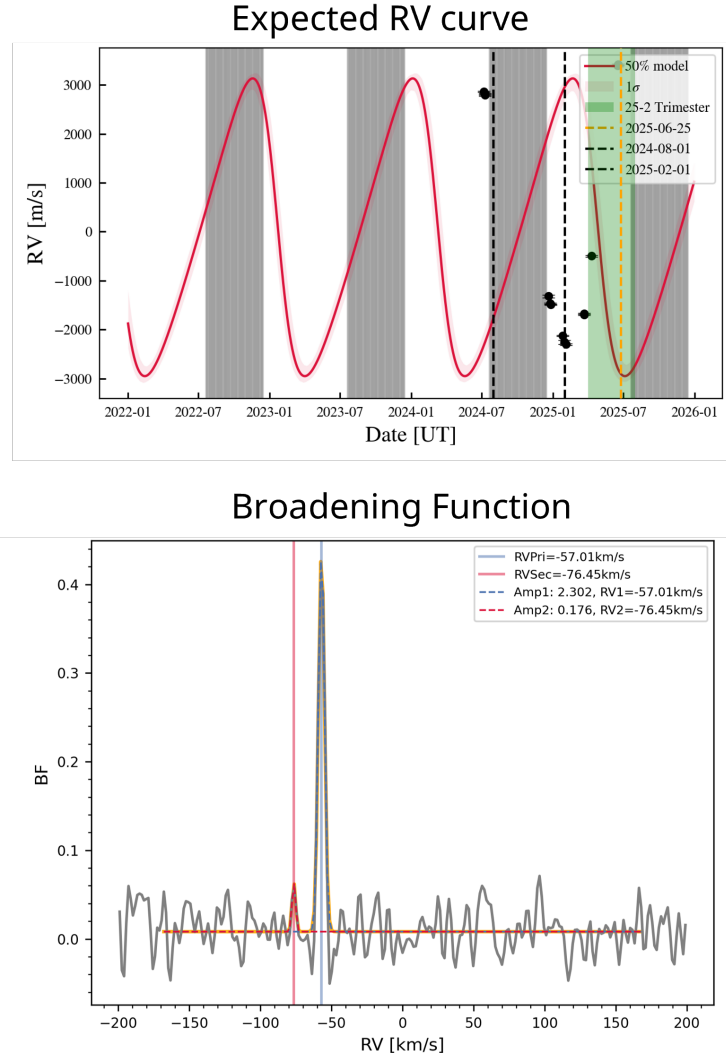


FIG. 4.7 – The expected RV curve (upper figure) and broadening function (lower figure) for Gaia DR3 3724701024704375424. The expected RV curve is calculated using the Gaia astrometric solution under the assumption of a single star, a full description is given in Section 2 and Section 3. For this figure the x-axis represents the date of measurement and on the y-axis the expected RV measurement in m/s . The red line indicates the expected RV and the thin pink area surrounding it a $1-\sigma$ deviation from this model. The shaded areas indicate the observing windows in which the target can be viewed with the Hobby-Eberly telescope. The Broadening function corresponds to a unspecified measurement, on the x-axis we see RV in km/s and on the y-axis the broadening function. The blue corresponds to the peak of the broadening function, which is taken as the measured RV. Note that the measured RV does not align with the expected RV. We ignored the movement of the system while calculating the expected RV curve (γ in Equation 2.26), which is unknowable before taking such measurements. Lastly, these figures were generated for internal use only, stylistic and scientific artifacts (such as shifted and flipped data) are still visible and should be ignored.

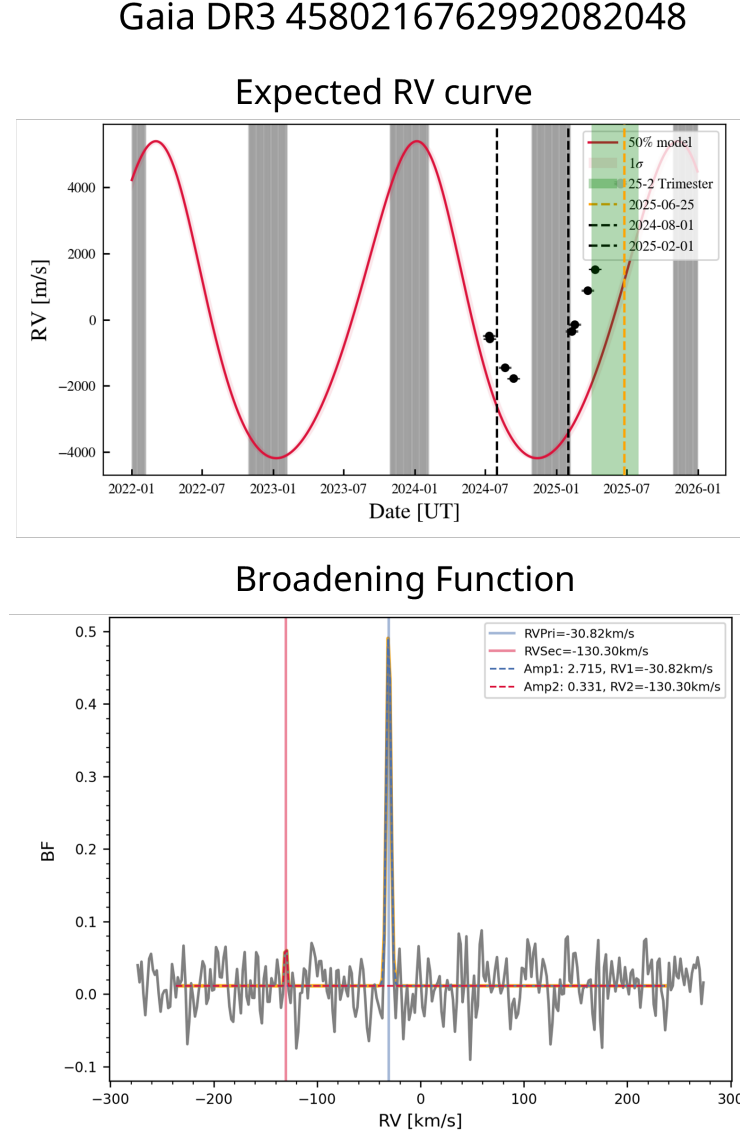


FIG. 4.8 – The expected RV curve (upper figure) and broadening function (lower figure) for Gaia DR3 4580216762992082048. This figure follows the same scheme as Figure 4.7. For reference I repeat these notes: The expected RV curve is calculated using the Gaia astrometric solution under the assumption of a single star, a full description is given in Section 2 and Section 3. For this figure the x-axis represents the date of measurement and on the y-axis the expected RV measurement in m/s . The red line indicates the expected RV and the thin pink area surrounding it a $1-\sigma$ deviation from this model. The shaded areas indicate the observing windows in which the target can be viewed with the Hobby-Eberly telescope. The Broadening function corresponds to a unspecified measurement, on the x-axis we see RV in km/s and on the y-axis the broadening function. The blue corresponds to the peak of the broadening function, which is taken as the measured RV. Note that the measured RV does not align with the expected RV. We ignored the movement of the system while calculating the expected RV curve (γ in Equation 2.26), which is unknowable before taking such measurements. Lastly, these figures were generated for internal use only, stylistic and scientific artifacts (such as shifted and flipped data) are still visible and should be ignored

TABLE 4.2 Preliminary stellar and orbital parameters for Object 1 and Object 2 and their companions. The parameters are either adopted from Gaia, calculated using SED fitting or calculated using the Gaia astrometric solutions . The latter is done using a private software package. ¹ : See Table A.2 for a full description of the filters.

Parameter	Description	Object 1	Object 2
Identifiers			
Gaia DR3 Source ID	-	3724701024704375424	4580216762992082048
TIC ID	-	379115695	298545715
Equatorial Coordinates			
α_{J2016}	Right Ascension (RA), epoch J2016	13:43:38.54	17:49:58.60
δ_{J2016}	Declination (Dec), epoch J2016	+08:25:44.97	+22:41:04.99
μ_α	Proper motion (RA, mas yr ⁻¹)	-245.03 ± 0.50	-773.12 ± 0.04
μ_δ	Proper motion (Dec, mas yr ⁻¹)	91.08 ± 0.45	-127.65 ± 0.07
Magnitudes and Spectral Type¹			
2MASS <i>H</i>	-	11.53 ± 0.02	11.53 ± 0.02
2MASS <i>J</i>	-	12.19 ± 0.02	12.19 ± 0.02
2MASS <i>K_s</i>	-	11.22 ± 0.02	11.22 ± 0.02
GALEX NUV	-	21.63 ± 0.41	21.63 ± 0.41
Gaia BP	-	18.50 ± 0.02	18.50 ± 0.02
Gaia G	-	15.888 ± 0.003	15.888 ± 0.003
Gaia RP	-	14.468 ± 0.004	14.468 ± 0.004
PS1 <i>g</i>	-	18.83 ± 0.01	18.83 ± 0.01
PS1 <i>i</i>	-	15.20 ± 0.01	15.20 ± 0.01
PS1 <i>r</i>	-	17.48 ± 0.01	17.48 ± 0.01
PS1 <i>y</i>	-	13.65 ± 0.01	13.65 ± 0.01
PS1 <i>z</i>	-	14.18 ± 0.01	14.18 ± 0.01
TESS	-	14.30 ± 0.01	14.30 ± 0.01
WISE W1	-	11.04 ± 0.02	11.04 ± 0.02
WISE W2	-	10.82 ± 0.02	10.82 ± 0.02
Spectral Type	-	M6.5V	M7.5V
Stellar Parameters (SED Fitting)			
M_* (M_\odot)	Mass (Isochrone)	0.12 ± 0.01	0.11 ± 0.01
R_* (R_\odot)	Radius	0.16 ± 0.01	0.16 ± 0.01
$T_{\text{eff}}(K)$	Effective temperature	2770 ⁺²⁴ ₋₅₂	2609 ⁺⁴⁷ ₋₄₆
$\log g$ (cgs)	Surface gravity	5.38 ^{+0.06} _{-0.12}	5.63 ^{+0.17} _{-0.35}
[Fe/H]	Metallicity	-0.09 ^{+0.22} _{-0.12}	-0.17 ^{+0.15} _{-0.18}
Distance (Pc)	Distance from Sun	26.66 ^{+0.83} _{-0.40}	25.87 ^{+0.44} _{-0.30}
Stellar Parameters (Gaia NSS)			
M_* (M_\odot)	Mass	0.12 ± 0.01	0.12 ± 0.01
RUWE	Gaia RUWE	8.30	9.85
Companion and Orbital Parameters			
m	Companion mass (M_J)	42.5 ± 2.4	66.8 ± 3.3
P	Orbital period (days)	412.7 ± 1.2	673.6 ± 1.5
e	Eccentricity	0.28 ± 0.03	0.14 ± 0.01
i	Inclination (degrees)	133.8 ± 2.3	79.8 ± 0.2
A	Thiele-Innes Coefficient (mas)	1.99 ± 0.40	-11.64 ± 0.27
B	Thiele-Innes Coefficient (mas)	-3.53 ± 0.24	2.54 ± 0.21
F	Thiele-Innes Coefficient (mas)	-5.25 ± 0.21	4.79 ± 0.63
G	Thiele-Innes Coefficient (mas)	-2.43 ± 0.39	-3.68 ± 0.15

Chapter 5

Conclusion

In this Thesis, I have analyzed the reliability and diagnostic potential of spectral energy distribution (SED) fitting for characterizing stellar hosts of the Gaia Astrometric Objects of Interests (ASOIs), using the `astroARIADNE` software. I retrieved multiple stellar parameters of single-star systems and found they were in agreement with the literature. A key aim of this work was to explore any signs of multiplicity within the SED fits and color-magnitude diagrams (CMDs). This was done by comparing the retrieved parameters to literature data and performing regression tests on a total of 139 metrics. Most of the significant metrics were artifacts of the Jupiter Desert, a region within the host mass-planet mass parameter space with a scarcity of exoplanets. The exceptions were the TESS noise term, which `astroARIADNE` introduces to account for stellar variability and the residuals from a fitted Main-Sequence. The correlation of these metrics needs to be viewed in a critical context. In both cases, we are severely limited by our available sample size. In case of the TESS noise metric, other liabilities were also noted. Our hypothesized correlation between other noise terms were not found to be correlated with multiplicity. In addition, I examined systems with severe disagreements between models that are used in `astroARIADNE`'s Bayesian Model Averaging (BMA) framework. Some of these systems are confirmed to be binary systems, while others are yet to be followed up with observations. While such discrepancies may seem diagnostically useful, they are difficult to quantify and, in the used mathematical framework, problematic as a formal metric. Assuming that upcoming spectroscopic observations will continue to yield single-lined spectra, I derived stellar parameters for 8 systems using photometric data. Among these, three systems — Gaia-3, Gaia-4, and Gaia-5 — have already been confirmed as single-stars.

5.1 Acknowledgments

This thesis would not have been possible without the astronomical infrastructure that facilitated the data. I especially thank the European Space Agency and the research team behind the *Gaia* mission. The very fact these targets were highlighted is not only a feat of extraordinary astrometric precision but also a testament to ESA's dedication for open and transparent science. The observation teams behind the WIYN 3.5-meter, Hobby-Eberly and the ESO 3.6-meter telescopes, played an essential part in this work. Without their aid, the crucial follow-up observations would not be possible. I am also grateful to J. Vines, the developer behind the `astroARIADNE` software, which is extensively used in this work.

I would also like to thank the astronomy faculty at the University of Amsterdam (the Anton Pannekoek Institute – API), and specifically the participants of the Exoplanet and discs meetings, their pursuit of excellent education/science was of upmost importance to this work. The welcoming atmosphere at the institute facilitated an amazing learning environment and a great way to be introduced to academic astronomy.

On a personal note, I would like to thank my supervisor at the UvA, Dr. Gudmundur ('Gummi') K. Stefánsson for his guidance. The time, energy, and trust he placed in me — and in his other Master's students, Hugo and Kaya — are a testament to his passion for astronomy and exemplifies the supportive atmosphere at the API. A good learning environment is recognized by the freedom to make mistakes in a safe environment, which he consistently provided. I also thank the research team members — Elise Koo, Hugo Veldhuis, Juan Ignacio Espinoza Retamal, Kaya Han Taş and Rowen Glusman. Without their technical and moral support this work would not have been finished. Especially Elise, as her unspoken open-door policy was greatly appreciated. Without the moral support of my friends, Elise van Os, Max Smedes and Shannon Veldink this work nor the Master's program leading up to it would have been possible. In addition, I thank my friends at the UvA, 'the master room', for their continued moral and technical support. Specifically, Ziggy Weesing, Cristobal Zilleruelo, Aleksandra Bołbot and Jonas Pronk. Lastly, I would like to thank my sister, Sabine Bruijne, her fiancé Jari Koen and my parents, Saskia and Rene Bruijne for their never-ending support of my academic efforts and interests. There are many more that have played an important part in this work, both mentally and technically, Thank you!

Bibliography

- Alam, S. e. a. 2015, ApJS, 219, 12
- Allard, F., Homeier, D., & Freytag, B. 2012, Philosophical Transactions of the Royal Society A: Mathematical, Physical and Engineering Sciences, 370, 2765
- Alves. 2020, Convolve a SED with a filter
- Bailer-Jones, C. A. L., Rybizki, J., Fouesneau, M., Mantelet, G., & Andrae, R. 2018, The Astronomical Journal, 156, 58
- Bayo, A., Rodrigo, C., Barrado Y Navascués, D., et al. 2008, , 492, 277
- Benjamin, R. A. e. a. 2003, PASP, 115, 953
- Bessell, M. S. 1990, Publications of the Astronomical Society of the Pacific, 102, 1181
- Bianchi, L. e. a. 2011, MNRAS, 411, 2770
- Brown, A. 2024, PyGaia: Gaia science performance simulation toolkit
- Bryant, E. M., Bayliss, D., & Van Eylen, V. 2023, Monthly Notices of the Royal Astronomical Society, 521, 3663
- Buchner, J. 2023, Statistics Surveys, 17, arXiv:2101.09675 [stat]
- Buchner, J., Georgakakis, A., Nandra, K., et al. 2014, , 564, A125
- Casertano, S., Lattanzi, M. G., Sozzetti, A., et al. 2008, Astronomy Astrophysics, 482, 699–729
- Castelli, F. & Kurucz, R. L. 2003, in Modelling of Stellar Atmospheres, ed. N. Piskunov, W. W. Weiss, & D. F. Gray, Vol. 210, A20
- Chambers, K. C. e. a. 2016, arXiv e-prints [1612.05560]
- Cutri, R. M., Wright, E. L., Conrow, T., et al. 2021, VizieR Online Data Catalog: AllWISE Data Release (Cutri+ 2013), VizieR On-line Data Catalog: II/328. Originally published in: IPAC/Caltech (2013)

Bibliography

- Dotter, A. 2016, , 222, 8
- Duchêne, G., Oon, J. T., De Rosa, R. J., et al. 2022, Monthly Notices of the Royal Astronomical Society, 519, 778–798
- Eastman, J. D., Rodriguez, J. E., Agol, E., et al. 2019, EXOFASTv2: A public, generalized, publication-quality exoplanet modeling code
- Emelyanov, N. V. & Kondratyev, B. P. 2022, Icarus, 383, 115060
- Endl, M., Robertson, P., Cochran, W. D., et al. 2022, The Astronomical Journal, 164, 238
- [ESA], T. E. S. A. 2024, Gaia DR3 known issues - Gaia - Cosmos
- European Southern Observatory (ESO). 2002, HARPS, <https://www.eso.org/public/teles-instr/lasilla/36/harps/>, accessed via ESO public archive
- European Southern Observatory (ESO). 2022, NIRPS, <https://www.eso.org/public/teles-instr/lasilla/36/nirps/>, accessed via ESO public archive
- European Space Agency [ESA] & The Gaia Collaboration. 2023, Gaia Data Release 3: Documentation Release 1.3 (The Gaia Collaboration)
- Feng, F. 2024, arXiv, arXiv:2403.08226 [astro-ph]
- Feroz, F., Hobson, M. P., & Bridges, M. 2009, , 398, 1601
- Fitzpatrick, E. L. 1999, Publications of the Astronomical Society of the Pacific, 111, 63
- Fragoso, T. M., Bertoli, W., & Louzada, F. 2018, International Statistical Review, 86, 1–28
- Fulton, B. & Petigura, E. 2017, RadVel: Radial Velocity Fitting Toolkit
- Gaia Collaboration. 2016, A&A, 595, A1
- Gaia Collaboration. 2018, A&A, 616, A1
- Ginsburg, A., Sipócz, B. M., Brasseur, C. E., et al. 2019, , 157, 98
- Hara, N. C. & Ford, E. B. 2023, Annual Review of Statistics and Its Application, 10, 623–649
- Hauschildt, P. H., Allard, F., & Baron, E. 1999, The Astrophysical Journal, 629, 865
- Henden, A. A., Levine, S., Terrell, D., & Welch, D. L. 2015, in American Astronomical Society Meeting Abstracts, Vol. 225, American Astronomical Society Meeting Abstracts #225, 336.16

- Henden, A. A. & Munari, U. 2014, Contrib. Astron. Obs. Skalnaté Pleso, 43, 518
- Henry, T. J., Jao, W.-C., Subasavage, J. P., et al. 2006, , 132, 2360
- Høg, E., Fabricius, C., Makarov, V. V., et al. 2000, , 355, L27
- Husser, T.-O., von Berg, S. W., Dreizler, S., et al. 2013, Astronomy & Astrophysics, 553, A6
- Høg, E. e. a. 2000, A&A, 355, L27
- Kent, J. 2020, A Practical Introduction to Nested Sampling – Part 1, <https://jamesckent.com/2020/01/a-practical-introduction-to-nested-sampling-part-1/>, accessed 30 June 2025
- Kharchenko, N. V. 2001, KFNT, 17, 409
- Kirkby, D., Robitaille, T., Weaver, B. A., et al. 2024, desihub/speclite: Bug fix release: General clean-up prior to refactoring package infrastructure
- Kouwenhoven, M. B. N., Brown, A. G. A., & Kaper, L. 2007, Astronomy Astrophysics, 464, 581–599, arXiv:astro-ph/0611903
- Kunder, A., Kordopatis, G., Steinmetz, M., et al. 2017, The Astronomical Journal, 153, 75, arXiv:1609.03210 [astro-ph]
- Kurucz, R. 1993, ATLAS9 Stellar Atmosphere Programs and 2 km/s grid. Kurucz CD-ROM No. 13. Cambridge, 13
- Lasunnty. 2007, File:Orbit1.svg - Wikimedia Commons (Wikipedia)
- Marcussen, M. L. & Albrecht, S. H. 2023, , 165, 266
- Martin, P.-Y. 2019, Catalogue of Exoplanets
- Mollière, P. & Mordasini, C. 2012, Astronomy Astrophysics, 547, A105
- Morton, T. D. 2015, isochrones: Stellar model grid package
- NASA. 2025, NASA Exoplanet Archive
- NASA Exoplanet Science Institute (NExScI). 2022, Exoplanet Follow-up Observing Program Web Service, <https://catcopy.ipac.caltech.edu/dois/doi.php?id=10.26134/EXOFOP5>, DOI: 10.26134/EXOFOP5, IPAC, Caltech/NASA
- Ochsenbein, F., Bauer, P., & Marcout, J. 2000, Astronomy and Astrophysics Supplement Series, 143, 23–32
- Paunzen, E. 2015, A&A, 580, A23

Bibliography

- Pearce, L. 2022, RUWE as an Indicator of Multiplicity, accessed 30 June 2025
- Pecaut, M. J. & Mamajek, E. E. 2013, The Astrophysical Journal Supplement Series, 208, 9
- Pecaut, M. J. & Mamajek, E. E. 2013, , 208, 9
- Perryman, M. 2012, The European Physical Journal H, 37, 745–792
- Ricker, G. R., Winn, J. N., Vanderspek, R., et al. 2014, Journal of Astronomical Telescopes, Instruments, and Systems, 1, 014003
- Sahlmann, J. & Gómez, P. 2025, , 537, 1130
- Sahlmann, J. & Gómez, P. 2024, arXiv:2404.09350 [astro-ph]
- Schlafly, E. F. & Finkbeiner, D. P. 2011, The Astrophysical Journal, 737, 103
- Skilling, J. 2004, in American Institute of Physics Conference Series, Vol. 735, American Institute of Physics Conference Series, ed. R. Fischer, R. Preuss, & U. V. Toussaint, 395–405
- Skilling, J. 2006, Bayesian Anal., 1, 833
- Skrutskie, M. F. e. a. 2006, AJ, 131, 1163
- Sozzetti. 2025, The Gaia Mission: Toward DR4: Know Thy Planet 2
- Sozzetti, A., Giacobbe, P., Lattanzi, M. G., et al. 2014, Monthly Notices of the Royal Astronomical Society, 437, 497–509, arXiv:1310.1405 [astro-ph]
- Sozzetti, A., Pinamonti, M., Damasso, M., et al. 2023, AA, 677, L15
- Speagle, J. I. f. P. . A. M. I. 2021, Joshua Speagle - A Brief Introduction to Nested Sampling - IPAM at UCLA
- Speagle, J. S. 2020, , 493, 3132
- Stassun, K. G., Oelkers, R. J., Pepper, J., et al. 2018, , 156, 102
- Stefansson, G. 2024, GitHub - gummiks/rvprec
- Stefansson, G. 2025, Histogram of the nearest stars (within 10 parsec)
- Stefansson, G., Mahadevan, S., Winn, J., et al. 2024, Gaia-4b and 5b: Radial Velocity Confirmation of Gaia Astrometric Orbital Solutions Reveal a Massive Planet and a Brown Dwarf Orbiting Low-mass Stars
- Stefansson, G. g. 2018, GitHub - HPF-SNR-plots: HPF Signal to noise plots
- Stefansson, G. K. 2019, PhD thesis, Pennsylvania State University, Pennsylvania, US

- Stefánsson, G., Mahadevan, S., Winn, J. N., et al. 2025, The Astronomical Journal, 169, 107
- Stevenson, A. T., Haswell, C. A., Barnes, J. R., & Barstow, J. K. 2023, arXiv:2310.02695 [astro-ph]
- The European Space Agency [ESA]. 2022, Gaia exoplanets - Gaia - Cosmos
- The European Space Agency [ESA]. 2023, GAIA Data Release Scenario - GAIA - Cosmos
- The European Space Agency [ESA]. 2025, Last starlight for ground-breaking Gaia
- The Gaia Collaboration. 2023
- The Gaia Collaboration, Arenou, F., Babusiaux, C., et al. 2023, Astronomy Astrophysics, 674, A34
- The Gaia Collaboration, Prusti, T., De Bruijne, J. H. J., et al. 2016, Astronomy Astrophysics, 595, A1
- The Gaia Collaboration, Smart, R. L., Sarro, L. M., et al. 2021, Astronomy Astrophysics, 649, A6
- Trifonov, T. 2024
- Vallenari, A., Brown, A. G. A., Prusti, T., et al. 2023, Astronomy amp; Astrophysics, 674, A1
- Vines, J. I. & Jenkins, J. S. 2022, [[arXiv]2204.03769]
- Wallace, A. L., Casey, A. R., Brown, A. G. A., & Castro-Ginard, A. 2024, arXiv:2411.06705 [astro-ph]
- Wright, E. L. e. a. 2010, AJ, 140, 1868
- Yi, S., Demarque, P., Kim, Y.-C., et al. 2001, The Astrophysical Journal Supplement Series, 136, 417
- Yi, T. 2024, The Astrophysical Journal, 965, 92

Appendix A

Ariadne

TABLE A.1 Stellar parameters derived from SED fitting. The values shown are from the second run, with exception to the Objects notated with a ¹. These indicate the results from the third run.

Gaia DR3 Source ID	$M (M_{\odot})$	$R (R_{\odot})$	$T_{\text{eff}} (\text{K})$	$\log g (\text{cgs})$	Distance (pc)	[Fe/H] (dex)	Age (Gyr)	Status
6685861691447769088	0.48 ^{+0.02} _{-0.02}	0.46 ^{+0.02} _{-0.03}	3514 ⁺¹⁵¹ ₋₆₅	4.53 ^{+1.11} _{-0.66}	99.64 ^{+1.08} _{-0.40}	0.24 ^{+0.17} _{-0.41}	2.59 ^{+9.81} _{-1.98}	Unknown
6471102606408910848	0.85 ^{+0.20} _{-0.18}	0.05 ^{+0.00} _{-0.00}	6509 ⁺¹³⁴ ₋₂₆₅	3.95 ^{+0.48} _{-0.33}	62.70 ^{+0.60} _{-0.49}	-0.36 ^{+0.22} _{-0.19}	1.05 ^{+6.97} _{-0.03}	Unknown
1052042828882790016	0.25 ^{+0.07} _{-0.07}	0.47 ^{+0.02} _{-0.02}	3369 ⁺¹²⁰ ₋₄₂	5.77 ^{+0.85} _{-0.85}	78.36 ^{+0.45} _{-0.45}	-0.14 ^{+0.15} _{-0.30}	0.03 ^{+0.01} _{-0.01}	Binary
522135261462534528	0.99 ^{+0.06} _{-0.09}	1.07 ^{+0.02} _{-0.02}	6084 ⁺⁴⁰ ₋₄₀	4.37 ^{+0.44} _{-0.40}	27.03 ^{+0.02} _{-0.02}	-0.20 ^{+0.12} _{-0.12}	5.06 ^{+3.74} _{-1.74}	Unknown
3676303512147120640	0.20 ^{+0.01} _{-0.01}	0.22 ^{+0.01} _{-0.05}	3073 ⁺¹⁰⁴ ₋₃₅	5.52 ^{+0.33} _{-0.49}	38.76 ^{+0.42} _{-0.14}	0.16 ^{+0.21} _{-0.33}	0.98 ^{+4.38} _{-0.89}	Binary
637329067477530368	1.02 ^{+0.03} _{-0.02}	0.93 ^{+0.02} _{-0.01}	5697 ⁺⁴⁷ ₋₅₀	4.04 ^{+0.47} _{-0.42}	34.48 ^{+0.09} _{-0.07}	0.09 ^{+0.13} _{-0.14}	0.39 ^{+2.54} _{-0.86}	Unknown
5375875638010549248	0.36 ^{+0.02} _{-0.01}	0.40 ^{+0.02} _{-0.02}	3212 ⁺⁴⁶ ₋₅₃	5.60 ^{+0.31} _{-0.24}	67.00 ^{+0.12} _{-0.24}	-0.04 ^{+0.22} _{-0.22}	4.61 ^{+3.74} _{-1.80}	Unknown
1878822452815621120	0.90 ^{+0.03} _{-0.04}	0.82 ^{+0.01} _{-0.01}	5034 ⁺²⁷ ₋₂₄	4.37 ^{+0.50} _{-0.44}	62.52 ^{+0.24} _{-0.17}	-0.02 ^{+0.13} _{-0.14}	1.39 ^{+4.74} _{-1.26}	Single
6381440834777420800	0.25 ^{+0.01} _{-0.01}	0.27 ^{+0.01} _{-0.01}	3150 ⁺⁵⁷ ₋₃₆	5.35 ^{+0.51} _{-0.97}	60.56 ^{+0.69} _{-0.83}	-0.08 ^{+0.29} _{-0.35}	2.70 ^{+8.45} _{-2.13}	Unknown
1862136504889464320	0.35 ^{+0.02} _{-0.02}	0.36 ^{+0.01} _{-0.01}	3198 ⁺⁵² ₋₅₀	5.58 ^{+0.50} _{-0.53}	83.08 ^{+0.32} _{-0.30}	-0.16 ^{+0.35} _{-0.30}	10.70 ^{+1.03} _{-9.81}	Binary
6421118739093252096	1.14 ^{+0.05} _{-0.15}	1.84 ^{+0.03} _{-0.03}	5510 ⁺³³ ₋₃₃	4.44 ^{+0.43} _{-0.44}	71.35 ^{+0.18} _{-0.12}	-0.07 ^{+0.16} _{-0.14}	7.96 ^{+1.38} _{-1.21}	Unknown
5220375041387611136	0.79 ^{+0.04} _{-0.04}	0.76 ^{+0.01} _{-0.01}	4591 ⁺²⁹ ₋₂₉	4.91 ^{+0.36} _{-0.56}	184.52 ^{+0.80} _{-0.57}	-0.10 ^{+0.19} _{-0.18}	8.48 ^{+3.49} _{-7.61}	Unknown
2845310284780421120	0.32 ^{+0.03} _{-0.03}	0.15 ^{+0.01} _{-0.01}	3707 ⁺⁴⁹ ₋₃₅	5.68 ^{+0.22} _{-0.40}	41.40 ^{+0.63} _{-0.40}	-0.09 ^{+0.13} _{-0.20}	2.09 ^{+9.78} _{-3.08}	Binary
5122670101678217216	1.03 ^{+0.10} _{-0.11}	1.41 ^{+0.02} _{-0.02}	5884 ⁺³⁷ ₋₃₇	4.58 ^{+0.40} _{-0.56}	103.07 ^{+0.40} _{-0.31}	-0.18 ^{+0.15} _{-0.29}	7.29 ^{+1.71} _{-3.08}	Unknown
1879554280883275520	0.40 ^{+0.01} _{-0.01}	0.40 ^{+0.01} _{-0.01}	3410 ⁺⁴⁷ ₋₄₂	5.56 ^{+0.29} _{-0.52}	79.43 ^{+0.40} _{-0.23}	-0.04 ^{+0.22} _{-0.24}	3.68 ^{+8.17} _{-3.23}	Binary
2998643469106143232	0.32 ^{+0.02} _{-0.02}	0.22 ^{+0.01} _{-0.01}	3632 ⁺³⁴ ₋₃₉	3.76 ^{+0.21} _{-0.15}	48.35 ^{+0.01} _{-0.08}	0.26 ^{+0.09} _{-0.09}	1.92 ^{+8.97} _{-8.84}	Binary
2052469973468984320	0.46 ^{+0.02} _{-0.03}	0.47 ^{+0.03} _{-0.03}	3377 ⁺⁴⁴ ₋₃₉	5.54 ^{+0.43} _{-0.61}	17.39 ^{+0.09} _{-0.03}	-0.01 ^{+0.18} _{-0.08}	3.98 ^{+8.92} _{-8.48}	Binary
1610837178107032064	1.25 ^{+0.01} _{-0.01}	1.27 ^{+0.02} _{-0.02}	6140 ⁺⁵⁰ ₋₄₄	3.83 ^{+0.46} _{-0.21}	73.89 ^{+0.22} _{-0.17}	0.21 ^{+0.08} _{-0.08}	3.08 ^{+0.48} _{-1.72}	Single
4062446910648807936	0.82 ^{+0.03} _{-0.03}	0.76 ^{+0.02} _{-0.02}	4711 ⁺³⁵ ₋₄₂	5.14 ^{+0.29} _{-0.69}	40.04 ^{+0.12} _{-0.05}	0.02 ^{+0.23} _{-0.21}	1.95 ^{+7.09} _{-1.66}	Unknown
4812716639938468864	0.28 ^{+0.01} _{-0.01}	0.30 ^{+0.01} _{-0.01}	3065 ⁺⁴⁵ ₋₆₃	5.12 ^{+0.68} _{-0.38}	48.25 ^{+0.08} _{-0.19}	-0.04 ^{+0.29} _{-0.35}	6.53 ^{+3.96} _{-3.35}	Unknown
5085864568417060864	0.43 ^{+0.01} _{-0.02}	0.29 ^{+0.01} _{-0.01}	3636 ⁺²³ ₋₃₃	3.78 ^{+0.39} _{-0.20}	55.74 ^{+0.12} _{-0.08}	0.15 ^{+0.15} _{-0.11}	4.35 ^{+7.74} _{-3.76}	Binary
5654515588409755648	0.22 ^{+0.01} _{-0.01}	0.20 ^{+0.02} _{-0.02}	3369 ⁺¹³⁵ ₋₁₂₆	3.68 ^{+0.23} _{-0.12}	89.57 ^{+1.34} _{-1.02}	0.30 ^{+0.09} _{-0.09}	1.51 ^{+6.16} _{-1.38}	Unknown
6694115931396058112 ¹	0.30 ^{+0.02} _{-0.02}	0.31 ^{+0.01} _{-0.01}	3364 ⁺⁴⁹ ₋₃₂	5.57 ^{+0.28} _{-0.34}	38.22 ^{+0.09} _{-0.31}	0.12 ^{+0.22} _{-0.25}	1.08 ^{+10.38} _{-9.92}	Unknown
6521749994635476992	0.45 ^{+0.02} _{-0.02}	0.46 ^{+0.01} _{-0.01}	3352 ⁺⁴¹ ₋₄₁	5.64 ^{+0.63} _{-0.63}	62.27 ^{+0.07} _{-0.07}	-0.19 ^{+0.35} _{-0.24}	0.05 ^{+9.92} _{-0.05}	Unknown
1462767459023424512	0.34 ^{+0.01} _{-0.01}	0.36 ^{+0.02} _{-0.02}	3076 ⁺⁵⁹ ₋₅₂	5.26 ^{+0.69} _{-0.75}	72.05 ^{+0.26} _{-0.26}	-0.29 ^{+0.37} _{-0.30}	0.42 ^{+0.00} _{-0.04}	Single
4745373133284418560	1.10 ^{+0.05} _{-0.12}	1.21 ^{+0.03} _{-0.03}	6009 ⁺⁶⁴ ₋₅₂	3.86 ^{+0.39} _{-0.22}	17.38 ^{+0.07} _{-0.07}	-0.02 ^{+0.14} _{-0.13}	4.85 ^{+3.25} _{-7.00}	Unknown
373892712892466048	0.49 ^{+0.02} _{-0.02}	0.53 ^{+0.01} _{-0.03}	3327 ⁺⁵² ₋₇₄	4.83 ^{+0.68} _{-0.70}	75.28 ^{+0.44} _{-0.30}	0.18 ^{+0.65} _{-0.65}	0.05 ^{+0.54} _{-0.54}	Binary
2277249663873880832	0.26 ^{+0.12} _{-0.06}	0.49 ^{+0.02} _{-0.01}	3404 ⁺³² ₋₃₂	5.11 ^{+0.57} _{-0.78}	51.16 ^{+0.24} _{-0.05}	0.07 ^{+0.26} _{-0.16}	0.03 ^{+0.00} _{-0.00}	Binary
405316961377489792	0.24 ^{+0.02} _{-0.01}	0.27 ^{+0.01} _{-0.01}	3184 ⁺⁵⁵ ₋₄₅	5.06 ^{+0.70} _{-0.63}	77.62 ^{+0.56} _{-0.38}	-0.09 ^{+0.24} _{-0.20}	2.63 ^{+9.72} _{-2.07}	Single
8343575654456829441 ¹	0.38 ^{+0.01} _{-0.01}	0.29 ^{+0.00} _{-0.01}	3669 ⁺¹¹ ₋₁₁	4.21 ^{+0.15} _{-0.03}	53.59 ^{+0.02} _{-0.01}	0.21 ^{+0.05} _{-0.00}	3.50 ^{+8.27} _{-2.65}	Binary
246890014559489792	0.34 ^{+0.03} _{-0.09}	0.35 ^{+0.01} _{-0.01}	3141 ⁺³³ ₋₃₆	5.64 ^{+0.25} _{-0.53}	52.50 ^{+0.20} _{-0.09}	-0.14 ^{+0.25} _{-0.24}	0.15 ^{+1.63} _{-0.14}	Unknown
5055723587443421184	0.44 ^{+0.02} _{-0.02}	0.36 ^{+0.02} _{-0.03}	4041 ⁺⁸⁶ ₋₆₃	4.19 ^{+0.51} _{-0.41}	138.04 ^{+0.72} _{-0.54}	-0.15 ^{+0.15} _{-0.15}	0.94 ^{+9.26} _{-9.90}	Unknown
1457486023639239168	0.65 ^{+0.02} _{-0.02}	0.66 ^{+0.03} _{-0.02}	4044 ⁺⁴⁹ ₋₅₆	4.52 ^{+0.53} _{-0.42}	73.98 ^{+0.45} _{-0.22}	-0.10 ^{+0.10} _{-0.20}	1.20 ^{+9.54} _{-6.92}	Single
2367734656180390808	0.82 ^{+0.04} _{-0.04}	0.76 ^{+0.01} _{-0.02}	4549 ⁺¹⁷ ₋₂₂	4.53 ^{+0.22} _{-0.08}	34.50 ^{+0.01} _{-0.01}	0.27 ^{+0.04} _{-0.04}	1.98 ^{+6.92} _{-1.80}	Unknown
6677563745912844288	0.36 ^{+0.01} _{-0.02}	0.37 ^{+0.02} _{-0.02}	3149 ⁺⁴³ ₋₄₃	5.77 ^{+0.23} _{-0.97}	94.45 ^{+1.77} _{-0.31}	-0.11 ^{+0.33} _{-0.30}	0.62 ^{+11.78} _{-0.58}	Unknown
5446516751833167872	0.24 ^{+0.01} _{-0.01}	0.20 ^{+0.02} _{-0.02}	3250 ⁺¹⁰⁶ ₋₈₃	3.60 ^{+0.20} _{-0.08}	70.86 ^{+0.81} _{-0.54}	0.28 ^{+0.18} _{-0.14}	0.78 ^{+4.34} _{-7.02}	Unknown
4901802507993393152	0.99 ^{+0.15} _{-0.15}	1.22 ^{+0.03} _{-0.03}	4299 ⁺³² ₋₃₂	4.55 ^{+0.35} _{-0.40}	44.48 ^{+0.07} _{-0.07}	-0.11 ^{+0.17} _{-0.17}	0.01 ^{+0.00} _{-0.00}	Binary
1712614124767394816	0.70 ^{+0.03} _{-0.03}	0.75 ^{+0.02} _{-0.02}	4224 ⁺³⁸ ₋₃₈	5.36 ^{+0.27} _{-0.38}	35.41 ^{+0.04} _{-0.03}	-0.14 ^{+0.22} _{-0.21}	3.46 ^{+8.22} _{-2.52}	Single
5486916932205092864 ¹	0.30 ^{+0.01} _{-0.01}	0.23 ^{+0.01} _{-0.01}	3254 ⁺⁵² ₋₆₀	5.62 ^{+0.38} _{-0.20}	17.10 ^{+0.03} _{-0.16}	-0.18 ^{+0.25} _{-0.20}	1.14 ^{+8.70} _{-1.08}	Unknown
5618776310850226176	0.43 ^{+0.03} _{-0.03}	0.26 ^{+0.01} _{-0.01}	3735 ⁺³⁷ ₋₃₉	3.89 ^{+0.45} _{-0.36}	94.48 ^{+0.57} _{-0.74}	0.01 ^{+0.16} _{-0.16}	2.35 ^{+9.26} _{-2.07}	Binary
2047188847334279680	0.95 ^{+0.04} _{-0.04}	1.14 ^{+0.02} _{-0.02}	5398 ⁺³³ ₋₃₃	4.46 ^{+0.48} _{-0.48}	32.65 ^{+0.03} _{-0.03}	-0.11 ^{+0.15} _{-0.15}	11.87 ^{+2.84} _{-2.84}	Binary
55771789280890860	0.53 ^{+0.01} _{-0.01}	0.49 ^{+0.02} _{-0.00}	3640 ⁺¹ ₋₂₄	3.99 ^{+0.01} _{-0.16}	40.00 ^{+0.00} _{-0.00}	0.34 ^{+0.05} _{-0.00}	8.36 ^{+4.86} _{-6.38}	Binary
7364811062251600	0.22 ^{+0.01} _{-0.01}	0.25 ^{+0.01} _{-0.01}	3098 ⁺³¹ ₋₅₂	5.73 ^{+0.26} _{-0.53}	58.52 ^{+1.12} _{-0.21}	-0.39 ^{+0.31} _{-0.24}	2.30 ^{+5.43} _{-2.20}	Binary
2104920835634141696	0.18 ^{+0.00} _{-0.00}	0.21 ^{+0.01} _{-0.01}	3048 ⁺¹⁹ ₋₂₀	5.74 ^{+0.40} _{-0.31}	46.27 ^{+0.00} _{-0.16}	-0.13 ^{+0.14} _{-0.21}	2.01 ^{+2.52} _{-2.52}	Binary
5052449001298518016 ¹	0.28 ^{+0.07} _{-0.07}	0.46 ^{+0.02} _{-0.01}	3268 ⁺⁴⁹ ₋₄₉	5.77 ^{+0.23} _{-0.56}	59.09 ^{+0.31} _{-0.06}	-0.03 ^{+0.19} _{-0.27}	0.03 ^{+0.00} _{-0.01}	Binary
4842246017566494720	0.32 ^{+0.02} _{-0.01}	0.33 ^{+0.01} _{-0.01}	3294 ⁺⁴⁶ ₋₃₈	5.34 ^{+0.51} _{-0.25}	31.93 ^{+0.10} _{-0.32}	-0.14 ^{+0.32} _{-0.25}	6.60 ^{+5.66} _{-6.29}	Unknown
2074815898041643520	0.35 ^{+0.01} _{-0.01}	0.33 ^{+0.01} _{-0.01}	3497 ⁺⁶³ ₋₅₀	4.55 ^{+0.50} _{-0.43}	41.36 ^{+0.07} _{-0.08}	0.18 ^{+0.13} _{-0.13}	5.35 ^{+6.97} _{-5.95}	Single
4764340705296116736	0.34 ^{+0.02} _{-0.02}	0.34 ^{+0.01} _{-0.01}	3130 ⁺⁴⁵ ₋₄₅	4.73 ^{+0.69} _{-1.06}	61.82 ^{+0.15} _{-0.15}	0.08 ^{+0.21} _{-0.41}	2.04 ^{+5.83} _{-1.48}	Unknown
4232972766697088	0.37 ^{+0.02} _{-0.01}	0.39 ^{+0.02}						

Appendix A. Ariadne

TABLE A.2 Photometric Filters, Labels, and Wavelength Ranges with Catalogue References. ¹: Note that these filters are not used for the fitting procedure. these are only available for visualization (IR-excess). ²: These filters were included for the IR-only run.

Catalogue	Filter Label	Filter Name	Wavelength Range (nm)	Description
APASS DR9	B	Johnson B	390–490	Henden & Munari (2014)
	V	Johnson V	500–600	
ASCC	B	Johnson B	390–490	Kharchenko (2001)
	V	Johnson V	500–600	
ALL-WISE	W1 ²	WISE 3.4 μm	3300–3900	Wright (2010)
	W2 ²	WISE 4.6 μm	4600–5300	
	W3 ¹	WISE 12 μm	7800–9000	
	W4 ¹	WISE 22 μm	20000–25000	
2MASS	J ²	2MASS J	1100–1400	Skrutskie (2006)
	H ²	2MASS H	1500–1800	
	Ks ²	2MASS Ks	2000–2400	
SDSS DR12	u	SDSS u	300–400	Alam (2015)
	g	SDSS g	400–550	
	r	SDSS r	550–700	
	i	SDSS i	700–850	
	z	SDSS z	850–1000	
	g _{P1}	Pan-STARRS g	400–550	
Pan-STARRS1	r _{P1}	Pan-STARRS r	550–700	Chambers (2016)
	i _{P1}	Pan-STARRS i	700–820	
	z _{P1}	Pan-STARRS z	820–920	
	y _{P1} ²	Pan-STARRS y	920–1050	
	FUV	GALEX FUV	135–175	Bianchi (2011)
GALEX	NUV	GALEX NUV	175–280	
Strömgren	u	Strömgren u	350–370	Paunzen (2015)
	v	Strömgren v	400–420	
	b	Strömgren b	470–490	
	y	Strömgren y	550–570	
GLIMPSE	IRAC1 ²	IRAC 3.6 μm	3000–3900	Benjamin (2003)
	IRAC2 ²	IRAC 4.5 μm	4000–5000	
	IRAC3 ²	IRAC 5.8 μm	5200–6300	
	IRAC4 ²	IRAC 8.0 μm	7000–9000	
Tycho-2	B _T	Tycho B _T	390–490	Høg (2000)
	V _T	Tycho V _T	500–600	
Gaia DR2	G	Gaia G	330–1050	Gaia Collaboration (2016, 2018)
	BP	Gaia BP	330–680	
	RP	Gaia RP	630–1050	

TABLE A.3 Pearson correlation coefficient (r) and p -values for all tested metrics. Fitted values contain the prefix 'fit', the 1σ confidence interval is indicated with the suffixes 'upper' and 'lower'. Lastly, the literature values are found at the bottom, without special indication.

Parameter	r	p -value
fit_teff	-0.382342	0.030803
fit_teff_upper	-0.077101	0.674907
fit_teff_lower	-0.137724	0.452243
fit_logg	0.183657	0.314330
fit_logg_upper	-0.216919	0.233057
fit_logg_lower	0.041142	0.823094
fit_[Fe/H]	0.137188	0.454020
fit_[Fe/H].upper	0.077757	0.672295
fit_[Fe/H].lower	0.152563	0.404514
fit_dist	-0.199375	0.273959
fit_dist_upper	-0.058438	0.750716
fit_dist_lower	-0.288584	0.109196
fit_rad	-0.278417	0.122832
fit_rad_upper	-0.202420	0.266544
fit_rad_lower	-0.169856	0.352682
fit_grav_mass	-0.025015	0.891901
fit_grav_mass_upper	0.128503	0.483356
fit_grav_mass_lower	0.045330	0.805411
fit_lum	-0.297589	0.098095
fit_lum_upper	-0.315996	0.078089
fit_lum_lower	-0.316803	0.077290
fit_AD	-0.063926	0.728150
fit_AD_upper	0.040952	0.823898
fit_AD_lower	0.067209	0.714755
fit_age	0.178789	0.327548
fit_age_upper	-0.076228	0.678390
fit_age_lower	0.180196	0.323692
fit_iso_mas	-0.374952	0.034473
fit_iso_mas_upper	0.201629	0.268459
fit_iso_mas_lower	-0.024663	0.893415
fit_eep	-0.238696	0.188289
fit_eep_upper	0.224369	0.217001
fit_eep_lower	0.015240	0.934022
fit_NUV_noise	0.536398	0.072193
fit_NUV_noise_upper	0.567233	0.054424
fit_NUV_noise_lower	0.433911	0.158737
fit_BP_noise	-0.075530	0.681182
fit_BP_noise_upper	0.021080	0.908828

Continued on next page

Table A.3 – continued from previous page

Parameter	<i>r</i>	<i>p</i> -value
fit_BP_noise_lower	-0.065813	0.720438
fit_G_noise	0.140005	0.444715
fit_G_noise_upper	0.148971	0.415797
fit_G_noise_lower	-0.021716	0.906093
fit_RP_noise	0.267186	0.139320
fit_RP_noise_upper	0.061467	0.738233
fit_RP_noise_lower	0.210076	0.248492
fit_TESS_noise	0.351260	0.048690
fit_TESS_noise_upper	0.172424	0.345342
fit_TESS_noise_lower	0.245450	0.175720
fit_J_noise	0.111931	0.548850
fit_J_noise_upper	-0.074068	0.692111
fit_J_noise_lower	-0.029326	0.875556
fit_H_noise	0.182954	0.324560
fit_H_noise_upper	-0.051988	0.781205
fit_H_noise_lower	0.121663	0.514414
fit_Ks_noise	0.164736	0.367594
fit_Ks_noise_upper	0.051477	0.779631
fit_Ks_noise_lower	-0.061972	0.736160
fit_W1_noise	0.114829	0.584676
fit_W1_noise_upper	-0.143721	0.493099
fit_W1_noise_lower	-0.009214	0.965133
fit_W2_noise	0.081572	0.698291
fit_W2_noise_upper	0.139396	0.506335
fit_W2_noise_lower	-0.110931	0.597574
fit_u_noise	-0.698783	0.122432
fit_u_noise_upper	-0.402862	0.428398
fit_u_noise_lower	-0.529196	0.280307
fit_U_noise	0.771928	0.228072
fit_U_noise_upper	-0.130749	0.869251
fit_U_noise_lower	0.227929	0.772071
fit_v_noise	0.118902	0.822488
fit_v_noise_upper	-0.399432	0.432715
fit_v_noise_lower	-0.094033	0.859367
fit_B_noise	0.426733	0.339674
fit_B_noise_upper	0.393147	0.382934
fit_B_noise_lower	0.491558	0.262557
fit_g_noise	0.174051	0.708977
fit_g_noise_upper	0.268678	0.560162
fit_g_noise_lower	0.253719	0.583003
fit_V_noise	0.375507	0.406497

Continued on next page

Table A.3 – continued from previous page

Parameter	<i>r</i>	<i>p</i> -value
fit_V_noise_upper	0.401321	0.372209
fit_V_noise_lower	0.391501	0.385109
fit_r_noise	-0.559194	0.191859
fit_r_noise_upper	-0.385198	0.393482
fit_r_noise_lower	-0.361479	0.425629
fit_i_noise	-0.053476	0.919862
fit_i_noise_upper	0.255571	0.624990
fit_i_noise_lower	-0.280609	0.590134
fit_z_noise	0.143775	0.758435
fit_z_noise_upper	0.215435	0.642693
fit_z_noise_lower	0.036171	0.938635
fit_BT_noise	0.291554	0.575061
fit_BT_noise_upper	0.389984	0.444679
fit_BT_noise_lower	0.326637	0.527469
fit_b_noise	0.529136	0.470864
fit_b_noise_upper	0.358000	0.642000
fit_b_noise_lower	0.474410	0.525590
fit_VT_noise	0.288287	0.579549
fit_VT_noise_upper	0.325226	0.529361
fit_VT_noise_lower	0.306369	0.554825
fit_y_noise	0.521091	0.478909
fit_y_noise_upper	0.457304	0.542696
fit_y_noise_lower	0.392309	0.607691
fit_SDSS_u_noise	-0.228441	0.525557
fit_SDSS_u_noise_upper	-0.011263	0.975365
fit_SDSS_u_noise_lower	-0.216595	0.547808
fit_SDSS_g_noise	0.137552	0.686719
fit_SDSS_g_noise_upper	0.126540	0.710826
fit_SDSS_g_noise_lower	-0.425762	0.191686
fit_SDSS_r_noise	0.216723	0.522115
fit_SDSS_r_noise_upper	0.158731	0.641102
fit_SDSS_r_noise_lower	0.121054	0.722927
fit_SDSS_i_noise	0.314838	0.345679
fit_SDSS_i_noise_upper	0.165007	0.627786
fit_SDSS_i_noise_lower	0.346543	0.296468
fit_SDSS_z_noise	0.250619	0.457294
fit_SDSS_z_noise_upper	0.063424	0.853027
fit_SDSS_z_noise_lower	0.275527	0.412182
Teff (K)	-0.424558	0.015438
Teff (K) Error	0.482587	0.005152
log(g)	0.229719	0.205950

Continued on next page

Table A.3 – continued from previous page

Parameter	<i>r</i>	<i>p</i> -value
log(g) Error	-0.441691	0.011379
Radius (R_Sun)	-0.278100	0.123278
Radius (R_Sun) Error	-0.300624	0.094553
Mass (M_Sun)	-0.378558	0.032640
Mass (M_Sun) Error	-0.447190	0.010284
Density (g/cm ³)	0.218446	0.229703
Density (g/cm ³) <i>Error</i>	-0.301266	0.093817
Luminosity	-0.299370	0.096005
Luminosity Error	-0.286118	0.112394
Distance (pc)	-0.200652	0.270833
Distance (pc) Error	-0.069684	0.704712
Bp-Rp	0.429486	0.014163
Gmag_abs	0.353086	0.047451
MSresidual	0.467014	0.007045
Teff_diff	0.207212	0.255146
logg_diff	0.182802	0.316627
radius_diff	0.271350	0.133029
mass_diff	0.259955	0.150757
lum_diff	0.009194	0.960169